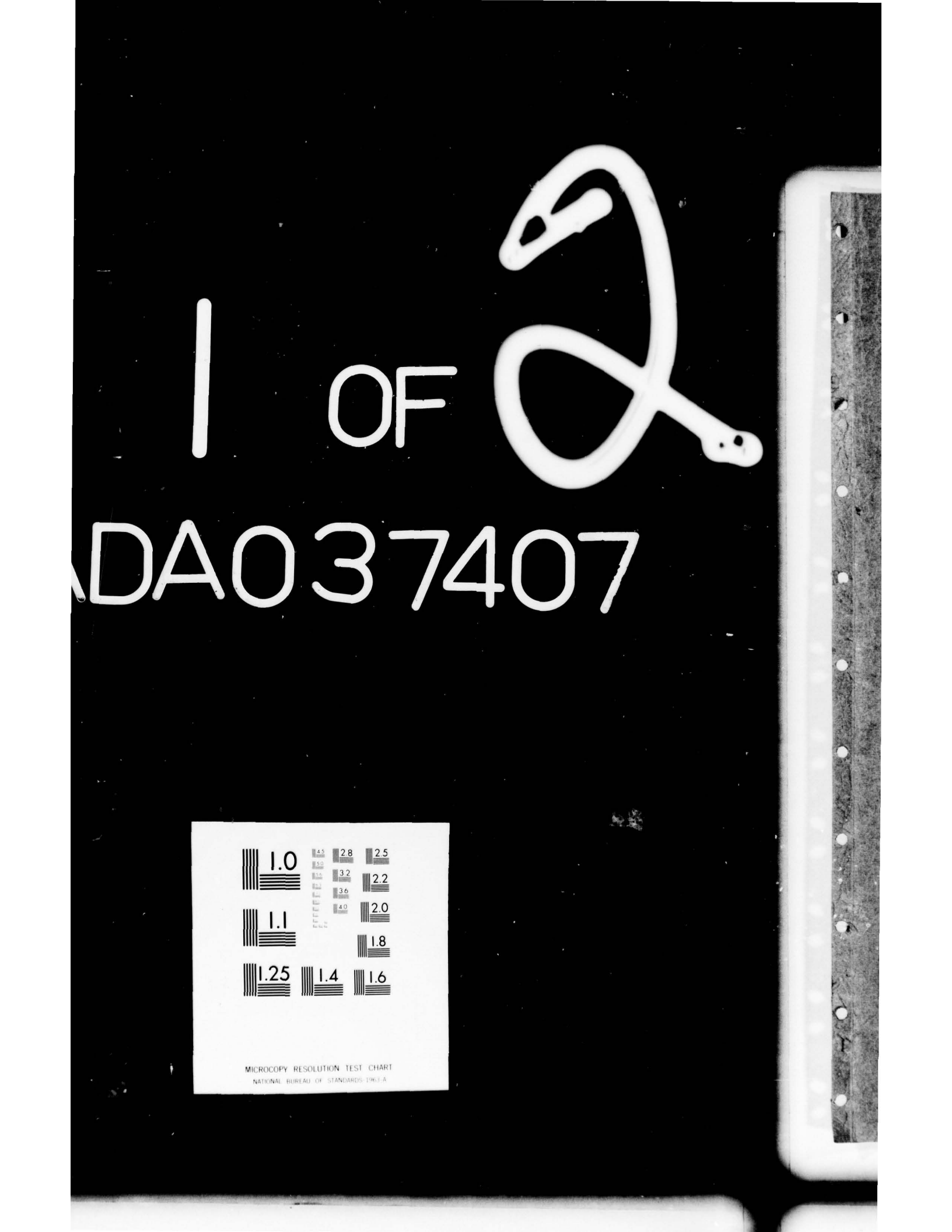
AD-A037 407 YALE UNIV NEW HAVEN CONN DEPT OF ENGINEERING AND AP--ETC F/G 7/4
THE DEVELOPMENT OF A PARALLEL-CHANNEL SPECTROGRAPHIC DETECTOR: --ETC(U)
MAR 77 P C BLACK
UNCLASSIFIED TR-1 N00014-76-C-0643
NL

1 OF 2
AD A037407




1 OF 2
AD A037407
1.0
1.1
1.25
1.4
1.6
2.8
3.2
3.6
4.0
2.5
2.2
2.0
1.8
MICROCOPY RESOLUTION TEST CHART
NATIONAL BUREAU OF STANDARDS 1963-A

ADA037407

COPY AVAILABLE TO DDC DOES NOT PERMIT FULLY LEGIBLE REPRODUCTION

THE DEVELOPMENT OF A PARALLEL CHANNEL SPECTROGRAPHIC DETECTOR

Philip G. Black
Department of Engineering and Applied Science
Yale University

Technical Report No. 1
to the
OFFICE OF NAVAL RESEARCH
Contract No. N00014-75-C-0643

AD No.
DDC FILE COPY

DISTRIBUTION STATEMENT A
Approved for public release;
Distribution Unlimited

DDC
NOV 13

(12)



THE DEVELOPMENT OF A PARALLEL-CHANNEL SPECTROGRAPHIC DETECTOR: APPLICATIONS TO RAMAN SCATTERING

by

Philip C. Black

Technical Report No. 1

to the

OFFICE OF NAVAL RESEARCH

Contract No. N00014-76-C-0643



March 1977

Distribution of this document is unlimited.

DEPARTMENT OF ENGINEERING
AND APPLIED SCIENCE

YALE UNIVERSITY

THE DEVELOPMENT OF A PARALLEL-CHANNEL SPECTROGRAPHIC DETECTOR: APPLICATIONS TO RAMAN SCATTERING

A Dissertation

Presented to the Faculty of the Graduate School

of

Yale University

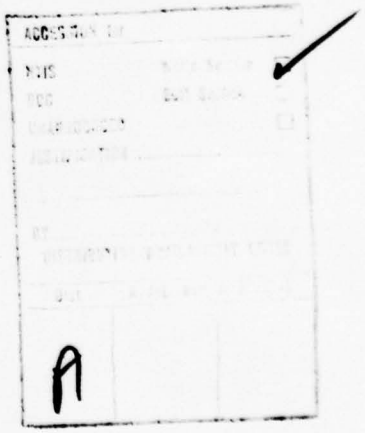
in Candidacy for the Degree of

Doctor of Philosophy

by

Philip Charles Black

1977



ABSTRACT

A parallel-channel detector was developed for use in visible and near-infrared light scattering experiments. The design goal of obtaining quantum-limited response simultaneously over 100 resolvable spectral elements has been achieved. This level of performance allows a significant (100:1) decrease in the time required to obtain a low-light level spectrum, when compared to the acquisition times of conventional detectors, such as the photomultiplier tube or photographic emulsion. Details of the design, construction, and operating characteristics of the parallel-channel detector are given, along with the results of Raman scattering measurements to determine: 1) the vibrational-rotational temperature of a flame; 2) the gas concentration profile of a gas-dynamic system. Implications of these measurement techniques are discussed.

ACKNOWLEDGMENTS

The research program described in this manuscript was carried out over a period of five years, during which time I have received encouragement, consultation, consolation, and countless hours of volunteer labor from many friends and acquaintances whose assistance has been invaluable both professionally and personally. It is with sincere gratitude that I acknowledge these contributions plus those by members of the industrial community and the various agencies supporting this work.

In particular, I thank the members of my thesis committee: Dr. Richard K. Chang (Advisor) for his faith and perseverance in pursuing the development of the parallel-channel detector and for the strength of character he has shown in fulfilling his commitments to the members of this laboratory, even under the most difficult of circumstances. Dr. Robert G. Wheeler and Dr. Arvid Herzenberg for their continuing interest in my professional development. Dr. John G. Zornig for help in dealing with the intricacies of the META-4 computer, as well as for his constant encouragement and sensible advice in matters both technical and personal. Dr. Boa-Teh Chu for many hours of excellent tutoring in the physics of fluids.

In addition, I would like to thank:

Dr. Peter J. Kindlmann for instruction in the art of electronic design and for his valuable assistance during the critical phases of constructing and testing the early detector implementations.

The late Dr. George J. Schulz for providing, by his personal example, an excellent model of laboratory management and scientific technique.

Dr. Paul B. Klein for his friendship, encouragement, and unselfish labor during the period of our co-residency in the laboratory.

Armand R. Tanguay, Jr. for countless valuable discussions of scientific techniques and for his strong personal interest in my progress and well being.

My coworkers in the laboratory: Walter Nagorski for technical assistance in the design and construction of the parallel-channel detector. Roger Farrow and Daniel Murphy for their good-natured help and cooperation.

The members of the Machine Shop and the Electronics Design Laboratory for skilled technical support.

Dr. Marshall Lapp and Dr. C. M. Penney of the General Electric Company Corporate Research and Development Center for the gracious loan of their flame apparatus and for their consultations regarding the flame experiment.

Westinghouse Electric Corporation and RCA for advice concerning the use of television camera tubes.

Varo, Inc. and Westinghouse Electric Corporation for their gifts of imaging devices.

The agencies providing financial support for this project: The Office of Naval Research, the National Science Foundation, and the Petroleum Research Fund.

Susie Engelman for typing the manuscript.

I would like to express my special appreciation to my wife and children for enduring the long hours and inconveniences of the past five years, as well as to our parents for their support, both spiritual and financial, without which I could not have completed my graduate studies.

TABLE OF CONTENTS

		Page
Chapter 1	THE CONCEPT OF A PARALLEL-CHANNEL DETECTOR	
1.1	Introduction	1
1.2	Early Low-Light Level Image Recording Systems	7
1.3	Early Parallel-Channel Detector Systems	14
1.4	Choice of Components	17
Chapter 2	INITIAL PARALLEL-CHANNEL DETECTOR CONFIGURATION	
2.1	The Isocon Camera	24
2.2	Initial Design Parameters	27
2.3	Device Testing	31
Chapter 3	FULL PARALLEL-CHANNEL DETECTOR IMPLEMENTATION	
3.1	Performance Problems	41
3.2	Digital Electronics	43
3.3	Analog Electronics	47
3.4	Mechanical/Optical Considerations	53
3.5	Computer Software	60
3.6	Results	63
Chapter 4	FINAL CONFIGURATION AND PERFORMANCE CHARACTERISTICS	
4.1	Introduction	68
4.2	Implementation	69
4.3	Noise Reduction	74
4.4	Resolution Enhancement	76
4.5	Final Parallel-Channel Detector Characteristics	77
4.6	Other Modern Parallel-Channel Detector Systems	84

		Page
4.6.1	Intensifier/Photographic Plate Method	86
4.6.2	Low-Sensitivity TV Camera Systems	86
4.6.3	High-Sensitivity TV Camera Systems	87
4.6.4	Discussion	88
Chapter 5	FLAME TEMPERATURE MEASUREMENTS	
5.1	Introduction	89
5.2	The Scattering Process	91
5.3	Experimental Results	112
Chapter 6	GAS CONCENTRATION MEASUREMENTS IN A DYNAMIC SYSTEM	
6.1	Experimental Configuration	116
6.2	Measurement Characteristics	123
6.3	Experimental Parameters	125
6.4	Experimental Results	129
6.5	Conclusions	139
Chapter 7	CONCLUDING REMARKS	
7.1	Current Capabilities	140
7.2	Future Improvements	142
7.3	Alternative Approaches to Parallel-Channel Detector Design	146
Appendix A	POLLUTANT DETECTION	148
Appendix B	CALCULATION OF COLLECTION EFFICIENCY	152
Appendix C	THE SELECTIVE-SCAN TECHNIQUE	156
Appendix D	DIGITAL I/O INTERFACE	160
Appendix E	SUPPLEMENTARY INFORMATION	164
	REFERENCES	173

LIST OF FIGURES

		Page
1.	Typical Raman scattering experiment	5
2.	Single-stage magnetically focused image intensifier	8
3.	Phosphor-photocathode interstage section	8
4.	Vidicon camera tube	12
5a.	Pulse-height distribution of single electron pulses from four-stage EMI image intensifier	15
5b.	Pulse-height distribution from single electron pulses with image intensifier and plumbicon camera	15
6.	Faceplate illumination vs. signal current	18
7.	Resolution vs. faceplate illumination	20
8.	Image Isocon television camera	25
9.	Computer-controlled low-light level TV camera system	30
10.	Apparatus and experimental result for a pulse-height analysis of single-photon events in a 40 mm three-stage intensifier	32
11a.	Video preamplifier	35
11b.	Analog video processing	36
12.	Schematic diagram of the parallel-channel Raman apparatus used in the reflection geometry	39
13.	Raman scattering from silicon	40
14.	Digital communication system	44
15.	Geometry and intensity correction of video signals	48
16.	Pincushion distortion test patterns	49

		Page
17a.	Video amplifier and DC restoring	51
17b.	Gain normalization	52
18a.	Enclosure with cover removed, showing details of the yoke clamps and intensifier supports	54
18b.	Closeup of the front inside surface of the enclosure, viewed from above	55
18c.	Enclosure with the cover in place	56
19.	Raman scattering from silicon, λ_o = 4880 Å	67
20a.	Video amplifiers with gain selection, DC restoring circuit	70
20b.	Integrator with gain selection	71
21.	Oscilloscope Z-axis driver circuit	73
22.	Photon-event detector, dual discriminator, and threshold modulation	79
23.	Photon-event detector, digital filtering, and Z-axis modulator	80
24.	Silicon in reflection geometry, 4880 Å probe	82
25.	Vibrational temperature measurements for various burner conditions	92
26.	Flame measurements	93
27.	Rigid and nonrigid rotator models	101
28.	Line positions for simple harmonic oscillator, nonrigid rotator	105
29.	Line positions for anharmonic oscillator with no rotational-vibrational coupling	105

Page

30. Line positions within a single band. Effects of vibrational-rotational coupling in anharmonic oscillator 107

31. Comparison of J-dependent terms in I(J) 109

32. Fully resolved Q-branch as a function of J 109

33. Fully resolved Q-branch as a function of $\Delta\nu$ 109

34. Unresolved Q-branch band shape 111

35. Convolution with a Gaussian slit function 111

36. Full set of vibrational-rotational bands at elevated temperature 111

37. Experimental apparatus for flame temperature measurement 113

38a. Experimental apparatus for gas concentration measurements 117

38b. Closeup of jet, focusing and collection lenses 118

38c. Complete optical arrangement 119

39. Preservation of spatial resolution along laser track 121

40-45. Gas jet data 132

B1. Spherical coordinates 153

B2. Geometric relationships 153

B3. Collection efficiency vs. f/number 155

C1. Intensity vs. wavelength, with equivalent frame rates 158

C2. Intensity vs. wavelength 159

D1. Digital I/O interface 162

Chapter 1

THE CONCEPT OF A PARALLEL-CHANNEL DETECTOR

1.1 Introduction

Until recently the principal detectors in the visible and near-visible regions of the spectrum have been photographic emulsions and photomultiplier tubes (PMTs). Photographic emulsion has the advantage of being simultaneously exposed to all wavelengths in the spectrum, thereby wasting no data. Unfortunately, its detector quantum efficiency (DQE) is low (less than 1%) and its dynamic range is poor. We define (linear) dynamic range as the ratio of the largest and smallest signals for which detector response is linearly proportional to the input signal intensity. High-speed photographic emulsion has a dynamic range of 100 or less, whereas a good PMT can have a dynamic range of 5 or 6 orders of magnitude, if one count per second is a reasonable lower limit for linear detection. Further advantages of the PMT are its high DQE, up to 30% in the 0.2 to 1.0 μm range, and direct electronic readout. However, a PMT does not preserve the geometry of its source image and therefore must be used with a narrow bandpass scanning spectrometer. For instance, if a 100 Å region were to be scanned with 1 Å resolution, 100 separate measurements would have to be made with the PMT. During each "channel" of such a scan, the other 99 channels are disregarded--i.e., only 1% of the available data is acquired at any instant.

An ideal detector would have the simultaneous full-spectrum signal acquisition of photographic emulsion, as well as the high quantum efficiency, dynamic range, and direct electronic readout of the

PMT. The resulting "parallel-channel detector" (PCD) would offer a considerable speed advantage (at least 100:1) over either previous system. If one presumes the existence of a spectrographic detector which provides simultaneous data acquisition over 100 resolvable "channels," each channel providing single-photon (quantum-limited) sensitivity, then a broad range of new applications becomes available to researchers in the fields of visible and near-infrared spectroscopy. For Raman spectroscopy, where the signals of interest are typically very weak, speed alone is of considerable importance: a spectrum which would ordinarily require 24 hours of continuous data acquisition could be completed in approximately 15 minutes. This is not merely a convenience, since it is often impossible to maintain a stable experimental configuration over such a long period of time. The impact of a PCD is even more dramatic in studies of time-dependent or transient spectra. For example:

1. The detection of automotive pollutants. It is desirable to obtain a time-history of the evolution of many possible pollutants while an automobile is undergoing the Federal Drive Cycle test. Previous researchers (Fouche et al., 1971, 1972) have established that nearly all atmospheric pollutants of current interest can be uniquely identified by their Raman spectra. Thus, a PCD-based Raman spectrograph could simultaneously determine the concentrations of a large number of pollutants. The calculation in Appendix A indicates that a 5 W probe beam (5145 Å) would allow detection of pollutants in the parts per million concentration range

with 10 sec time resolution. This represents a large increase in performance over currently available instruments.

2. It was the conclusion of a study sponsored by the American Physical Society (Princeton, July 1974) on the application of physics to problems in combustion (Hartley et al., 1975) that there is a demonstrable need for diagnostic measurements of combustion processes. As will be explained in Chap. 5, Raman scattering can be used to measure the temperatures of flame constituents. The most accurate measurements require a full spectrum to be acquired (50 to 100 points), not just one or two points. It is possible to acquire such a spectrum in about two minutes using a conventional detector (Lapp, 1974), but variations in experimental conditions (i.e., instability or turbulence in the flame) make much shorter scans desirable. We have demonstrated the capability of measuring flame temperatures in less than one millisecond by using the PCD system. This time resolution is sufficient to study turbulent burning in some cases.
3. It is possible to monitor the relative concentration of a single gaseous species at many points along the usable track length of a laser probe beam. For instance, the radial concentration profile of gas emitted from a small cylindrical jet can be measured during the time span of a single pulse from a ruby laser. The

> intrinsically parallel data acquisition of the PCD insures that results for all points along the concentration profile refer to exactly the same event, not to possibly different events separated by macroscopic time intervals.

Thus, there was no lack of justification for our desire to develop a useful parallel-channel detector.

In our laboratory, interest in the PCD was based on its utility as a high-speed detector for use in Raman scattering experiments. Since scattering cross sections for nonresonant Raman processes are typically quite small, the Raman spectroscopist is often forced to deal with very weak spectra (less than 100 photons/spectral element/sec). A representative Raman scattering experiment is shown in Fig. 1. The output of the spectrograph consists of a series of light and dark vertical bands. Ideally, all radiation of a given wavelength will be imaged onto a single vertical line of uniform intensity, while the horizontal position of the line should be linearly related to wavelength (or wavenumber). The objective of any detection system is to accurately determine the location and intensity of each line in the spectrum. Several parameters are useful in evaluating the performance of a detector: spectral resolution, spectral coverage, sensitivity, dynamic range. For a PCD, the first two parameters are complementary since we can always increase spectral coverage by accepting lower resolution (selecting a spectrograph with less dispersion). A suitable figure of merit is: R = (spectral coverage)/(spectral resolution). For an ideal spectrograph, we see that R is just the spatial resolution of the detector. For a television camera, R is usually expressed as

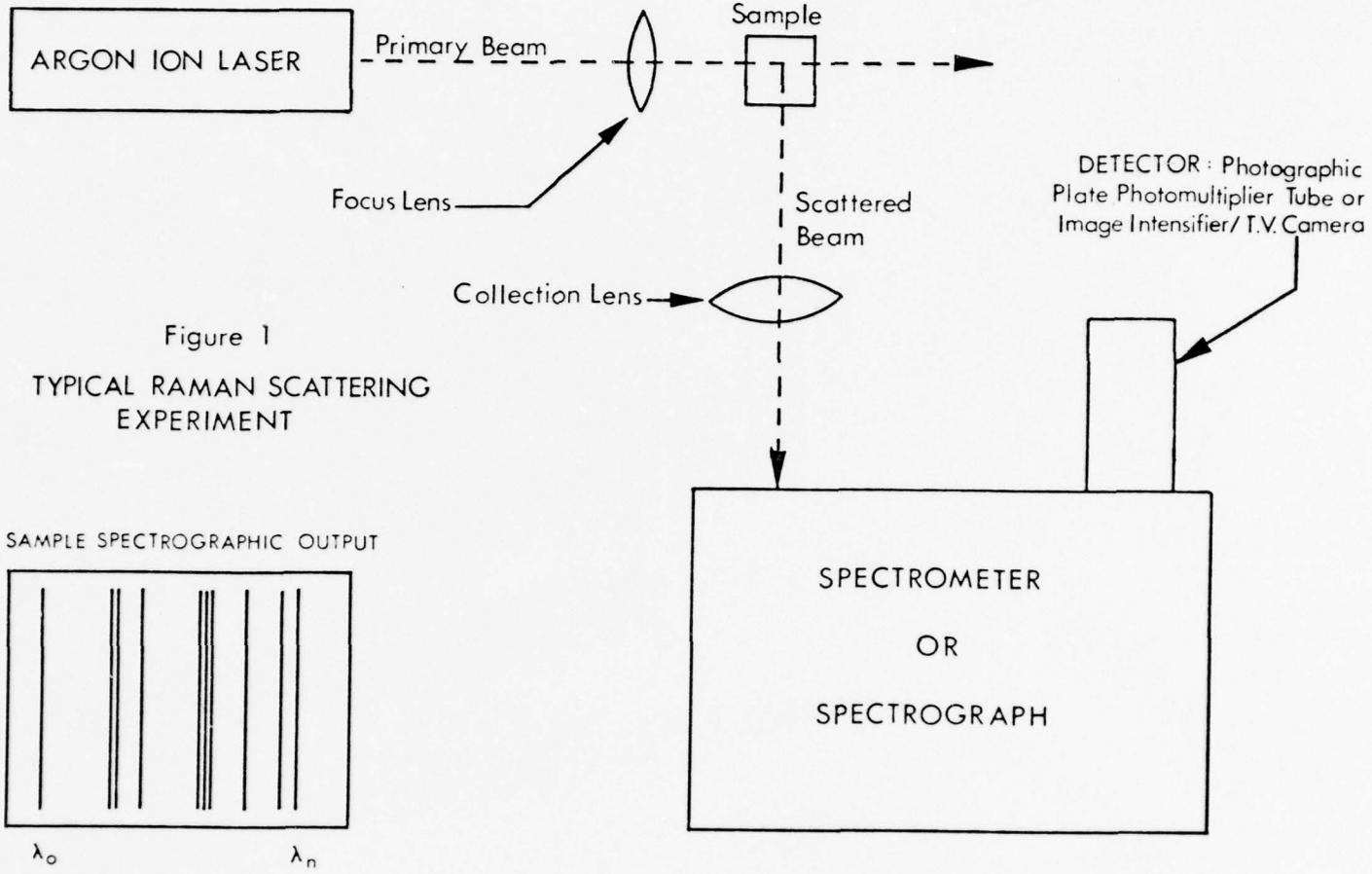


Figure 1

TYPICAL RAMAN SCATTERING EXPERIMENT

"TV lines per raster height," 525 lines being the industry standard. Table I gives a summary of parameters for three possible detectors. Note that for R = 100, the PCD system is by far the fastest of the three.

TABLE I

RELATIVE DETECTOR SPEED

	Photographic Emulsion Kodak IIa-0	PMT	PCD System
Maximum QDE (visible region)	0.3%	30%	30%
Number of resolvable spectral elements per measurement	R	1	R
Time per measurement	100t	t	t
Acquisition time for R channels	100t	Rt	t
Acquisition time per spectral element, assuming R = 100	t	t	t/100

$$R = (\text{spectral coverage})/(\text{resolution})$$

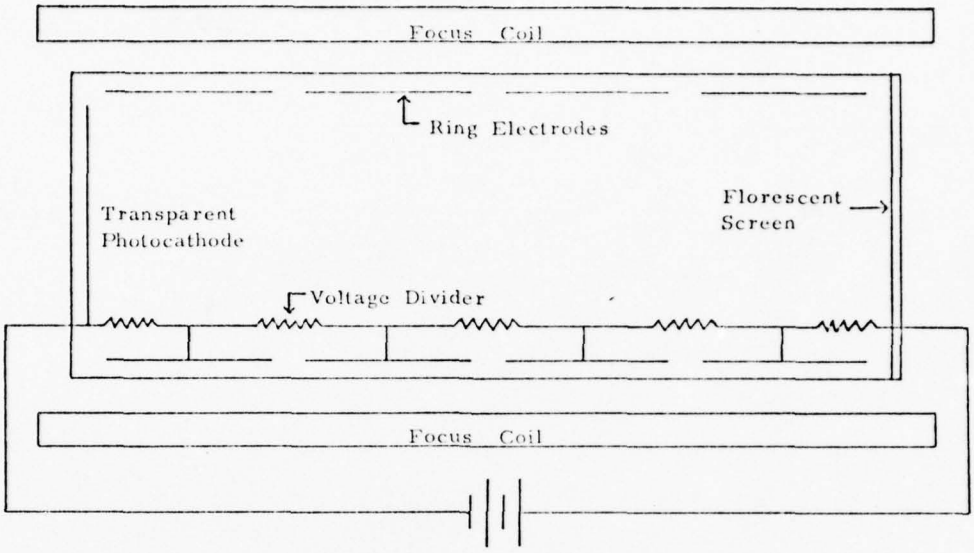
1.2 Early Low-Light Level Image Recording Systems

The need to record/analyze low-light level images is not unique to Raman spectroscopy, or even to spectroscopy in general. Much of the early research in low-light level systems was directed toward detection problems in the fields of nuclear physics (bubble chambers) and astronomy. In astronomy, it was very advantageous to replace the unaided human observer with a photographic emulsion (film plate), thereby providing a permanent record of each image. The major disadvantages of the film plate detector were its low dynamic range and quantum efficiency. Detection could be enhanced via long exposures, but this subjected the image to resolution degradation caused by atmospheric turbulence and tracking errors--i.e., as in spectroscopy "stationary" conditions can seldom be maintained over very long periods of time. For the nuclear physicist, transient event recording was the prime objective. Unfortunately, the response of photographic emulsions proved to be nonlinear for very short events.

In the 1920s, research began on a new type of imaging device: the image intensifier. The purpose of an image intensifier is to provide optical gain and/or wavelength conversion of an input image. Fig. 2 depicts a one-stage magnetically focused image intensifier in plan view. Photoelectrons ejected from the rear surface of the photocathode are accelerated toward the fluorescent screen, attaining a final energy of 10 to 15 keV. The device exhibits optical gain since each high energy electron causes the phosphor to emit a large number of photons. The axial magnetic field causes electrons emitted from the photocathode to strike a corresponding point on the phosphor screen, thereby maintaining the geometric integrity of the source image. Early tubes

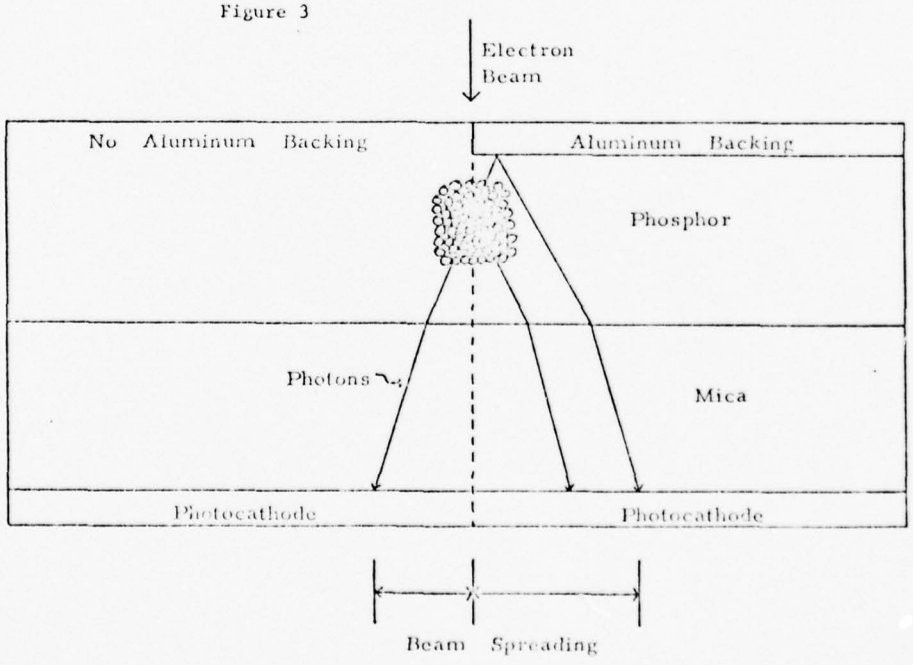
SINGLE STAGE MAGNETICALLY FOCUSED IMAGE INTENSIFIER

Figure 2



PHOSPHOR - PHOTOCATHODE INTERSTAGE SECTION

Figure 3



typically employed S-1 cathodes which provided better quantum efficiency in the near infrared than film plates. These devices could be more accurately called infrared-to-visible image converter tubes, since gains were always less than unity. (The combination of an S-1 photocathode and the best available output phosphor resulted in fewer photons being emitted from the output phosphor than photons striking the photocathode.)

In the 1940s, development of the cesium antimonide photocathode (Goerlich, 1941) and more efficient phosphors allowed gains of more than unity to be realized. The first practical multistage unit constructed by RCA (1949) used an interstage section wherein a thin ($\simeq$ 4 μm) mica substrate supported the phosphor of one stage and also the succeeding photocathode (Fig. 3, preceding page). The aluminum backing shown in the right half of Fig. 3 represents a compromise among several parameters. Its primary purpose is to prevent photons generated in the phosphor from returning to the previous photocathode, thereby causing an undesirable loss in image contrast. However, there is some reduction in gain due to the energy lost by photoelectrons in penetrating the aluminum backing and, as shown in the diagram, there is also a loss in resolution. In general, multistage intensifiers provide large gain at the expense of resolution, contrast, and image distortion.

Multistage intensifiers were extremely expensive due to the difficulty of fabricating the entire device as a single unit. (The interstage "sandwich" could not be split.) The availability of modular cascade image intensifiers had to await the development of fiber-optic plates in the 1950s. Such plates consist of a registered array of tiny fibers fused together, each fiber consisting of a core of high index of

refraction glass coated with a sheath of lower index of refraction glass. Photons entering a fiber at one end are transmitted very efficiently to the other end by a total internal reflection process.

In many modern intensifiers, the phosphor and photocathode of each stage are coated onto fiber-optic plates. This is particularly important for electrostatically focused units for which the best focusing geometry is obtained by placing the phosphor and photocathode on concave spherical surfaces. With fiber-optic plates, these internal surfaces can be curved even though the outer surfaces remain flat, allowing simple coupling between successive (modular) stages. This type of interstage coupling is very efficient if an index matching oil or cement is used between the two plates. By the early 1960s, it was possible to obtain relatively compact, high gain, cascade image intensifiers of the type described above, so-called first generation tubes, at a reasonable cost ($1,000 to $3,000 per stage). Following are some characteristic parameters for commercially available image intensifiers:

Input DQE	Photocathodes are the same as those in PMTs. Quantum efficiencies of 10% to 30% in the visible are common.
Gain	50 to 100 per stage. Multistage units provide gains of 10^4 to 10^7.
Resolution	Single stage center resolution of 60 line pairs per millimeter (lp/mm) at 3% contrast. Three- or four-stage units yield 25 lp/mm.
Geometric Distortion	A few percent per stage. Increases linearly with successive stages.

A typical data sheet is included in Appendix E.

A low-light level image recording system could consist of a photographic emulsion in conjunction with a suitable image intensifier. Indeed, many early astronomical detectors employed this method. Once exposed, the photographic plate can be developed and then analyzed with the aid of a densitometer. However, it is more appropriate to replace the film plate with a device which allows direct electronic readout of the intensified image, i.e., a television camera.

In many ways, a television camera is the modern electro-optic analog of a photographic plate. Fig. 4 is a cross-sectional view of a vidicon camera tube and yoke assembly. The vidicon camera is the least sophisticated television camera available but shares many operating principles with its more exotic relatives, Electron Bombarded Silicon or Silicon Intensifier Tube, Image Isocon, Image Orthicon, Secondary Electron Conduction tube, silicon vidicon, plumbicon, etc. (The underlined letters form widely used abbreviations for the camera names.) Photons enter the camera and strike the photoconductive target, causing the ejection of electrons from its rear surface. The loss of electrons from a particular point on the target results in a net positive charge at that spot. Since the target material is highly resistive, the positive charge center remains well localized. A low velocity electron beam constantly scans the back surface of the target. The beam electrons are boiled off a hot filament, accelerated to about 300 eV, and then traverse a section of constant electric potential where the beam is magnetically deflected. Just before the target, the beam is decelerated to near zero energy. As the beam is scanned across the target, it supplies enough electrons to the areas of positive charge to

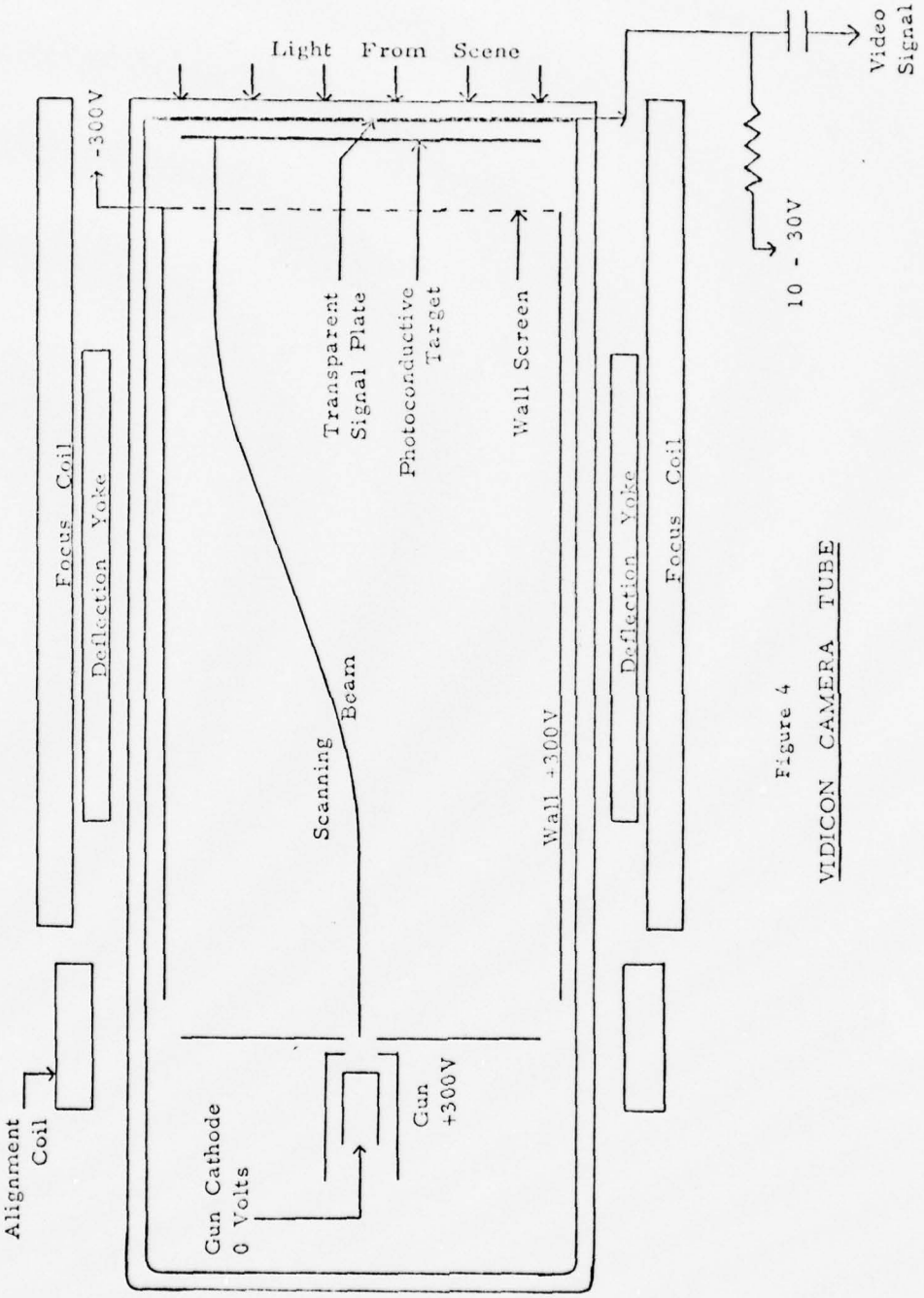


Figure 4

VIDICON CAMERA TUBE

restore the target to a charge-neutral state. This "erases" the information stored on the target, leaving it ready to accept a new image. Monitoring the target current provides a video signal which is directly proportional to the amount of light accepted by the target. The Electronics Industry Association standard frame rate is 30 frames per sec--that is, the entire target is scanned 30 times per sec.

Thus we see that the television camera is similar to an erasable film plate (photographic emulsion) with direct electronic readout. One must take care not to be misled by the serial manner of readout. The scanning electron beam reads/erases only one portion of the target at any instant in time, returning again after some time period T (the frame period). However, the target acts as a short-term integrator, continually storing any incoming photons as charge patterns, thereby recording all events. The process is entirely analogous to reading information from a film plate with a densitometer: readout is serial but data acquisition/integration is accomplished in an intrinsically "parallel" manner. A particular advantage of the television camera is that erasure occurs during readout, and data acquisition occurs throughout the entire procedure.

1.3 Early Parallel-Channel Detector Systems

An investigation of the parallel-channel detector concept was carried out in our laboratory early in 1971. Due to the unique advantages of using an intensified television camera as the primary detection/readout device, we became committed to the development of a low-light level television system (L^3TV). Perhaps the best established researcher in the L^3TV field at that time was Prof. M. Delhaye of the Université des Sciences et Techniques de Lille (France). Prof. Delhaye and his coworkers had enjoyed considerable success using an intensified SEC camera for ultra-rapid Raman spectroscopy (Delhaye, 1968; Bridoux and Delhaye, 1970). However, single photoelectron event recording had not been reported by this group. Johnson et al. (1971) worked with an "un-intensified" Image Orthicon camera, the principal message being that more gain was needed. Indeed, it seemed that no commercially available camera tube would provide quantum-limited response without the aid of an image intensifier. Mende (1971) employed a lens-coupled I^4Plumbicon (I^4Pb) system operating in the normal manner for a studio camera (Electronics Industry Association standard 525-line interlaced scan). A careful analysis of the system's modulation transfer function (MTF) was made with particular emphasis on specifying overall response to single-photon events. Of particular interest (see Fig. 5) was the fact that even though the (four-stage) intensifier output pulse-height distribution* for single-photon events showed a distinct peak, the complete

*The pulse-height distribution is typically measured as follows: Single photons are allowed to enter the electro-optic system. For each accepted photon an output event occurs, which is classified according to its size (by some measure). After many events have been measured, a histogram can be formed showing "size of event" vs. "probability of occurrence." If all events are nearly identical, a sharply peaked distribution occurs. A peaked distribution allows reliable discrimination between real events and noise (i.e., good photon counting), whereas a non-peaked distribution makes such discrimination very difficult.

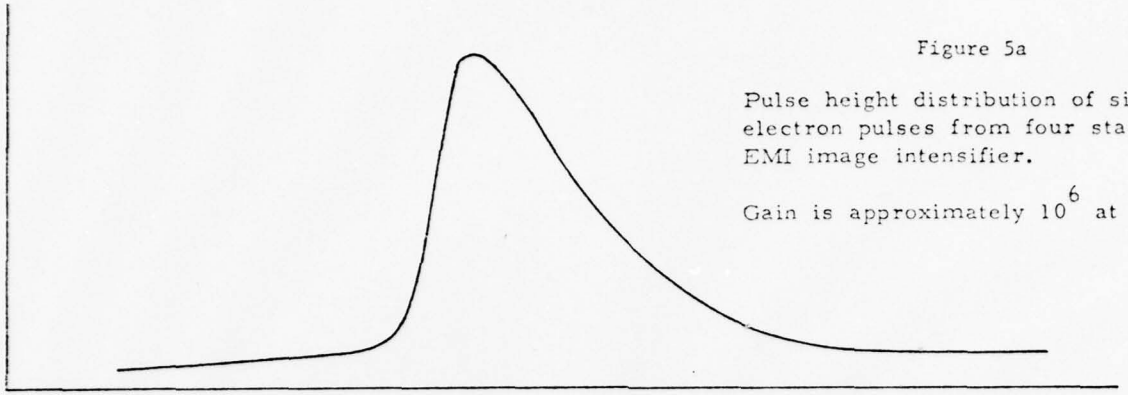


Figure 5a

Pulse height distribution of single electron pulses from four stage EMI image intensifier.

Gain is approximately 10^6 at 37KV.

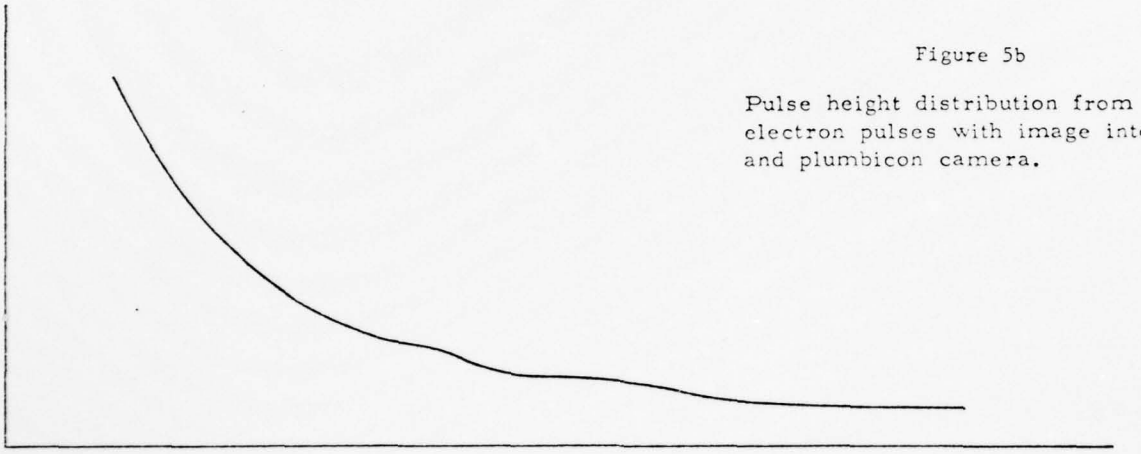


Figure 5b

Pulse height distribution from single electron pulses with image intensifier and plumbicon camera.

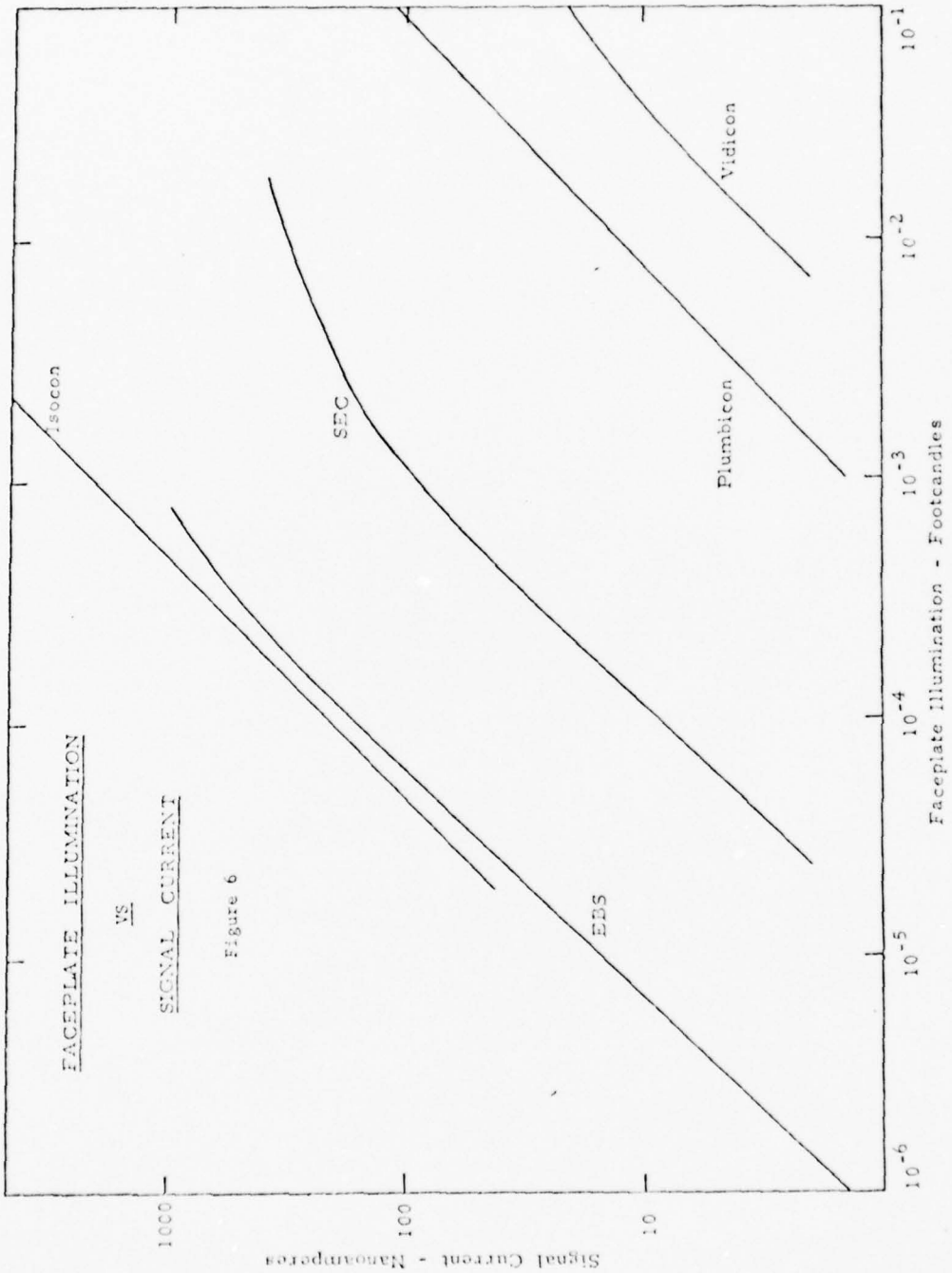
I^4Pb assembly showed a monotonically decreasing pulse-height distribution. The primary reason for this unfortunate outcome was thought to be a mismatch between the scan pattern of the camera and the apparent size of a photon event. In effect, photon events caused charge "bumps" on the vidicon target which were much larger than the pixel (least resolvable element) size of the camera. Thus, a single event would be "sliced up" by the read beam, making identification difficult. Savage and Maker (1971) were more successful in detecting single-photon events with their lens-coupled I^3Isocon system. They employed a more flexible sweep system, attaining best performance at 20 frames/sec with a 250-line raster. Major problems were resolution (about 100 lines) and dynamic range. (Linear detection was not possible for more than 5 events/frame/line.)

In short, it was clear that none of the existing systems met all of our design goals for a parallel-channel detector: ability to count single photons, good resolution (over 100 lines), and wide dynamic range (at least 1000:1). Of equal importance was the fact that none of the above-mentioned detectors were commercially available as a complete, packaged system. The only reasonable choice was to design and construct our own PCD.

1.4 Choice of Components

The most fundamental design decision regarding the PCD system was the selection of electro-optic devices for the L^3TV detector head. Our initial evaluation of camera tubes and image intensifiers was based on the available information concerning cost, sensitivity, resolution, and dynamic range. Data collected at that time are presented to illustrate the basis for our particular choice in components. With the exception of price, most of this information is still valid today. However, actual experience with the PCD caused some modification of our original opinions regarding the relative importance of various parameters. Discussion of those realizations is reserved for later chapters, and we concentrate here on the comparative analysis performed in 1971.

Inclusion of an image intensifier as part of the parallel-channel detector has a definite effect on the choice of a camera tube. First, the particular advantages of special photocathodes used in some cameras (silicon vidicon, plumbicon) are negated by the fact that the initial detector will, in any case, be the first-stage image intensifier photocathode. Second, we were not constrained to consider only the camera tube having the very best low-light level response. Instead we were forced to consider various image intensifier/TV camera combinations, compensating for reduced camera sensitivity by increasing numbers of intensifier gain stages. Camera sensitivity is still an important consideration since intensifier resolution degrades as the number of stages increases. Fig. 6 shows comparative sensitivity data taken from manufacturers' specification sheets for several camera types. The EBS or SIT tube is the clear winner here in terms of low-light level response, but it is noteworthy that the Isocon features output signal


FACEPLATE ILLUMINATION
VS
SIGNAL CURRENT
Figure 6
Isocon
SEC
EBS
Plumbicon
Vidicon
1000
100
10
10^{-6}
10^{-5}
10^{-4}
10^{-3}
10^{-2}
10^{-1}
Signal Current - Nanoamperes
Faceplate Illumination - Footcandles

currents comparable to the EBS camera in the region of overlapping response and peak currents (10 μA) an order of magnitude greater than any other camera shown. This increased signal current can be expected to reduce the effects of electronically induced noise and signal degradation during subsequent processing of the video signal. The Vidicon and the Plumbicon have insufficient sensitivity.

Fig. 7 depicts the second parameter of interest: resolution vs. faceplate illumination. Again the EBS camera dominates at extremely low-light levels, with the Isocon clearly superior for highlight illumination. In terms of dynamic range, all the cameras of interest are limited to a linear range of about 100:1 within a given scene. Table II summarizes the available information concerning quantum-limited television camera systems. The required number of intensifier stages was based on the assumed requirement of attaining a pre-target gain of about 10^6. Although this figure seems excessive for the Isocon, it is necessary if one expects to operate the camera tube in the input illumination range which allows best dynamic range and large output current. Overall, the final choice seemed to rest between the I^1SIT and the I^3Isocon. After consideration, the I^3Isocon was chosen for the following reasons:

1. Large output signal current: Eases the design requirements for the video amplifier.
2. Greater highlight resolution: It was not clear whether or not this advantage would be lost in the three-stage intensifier.
3. Cost: The 40 mm I^3Isocon system was approximately one-half as expensive as a 40 mm I^1SIT assembly.

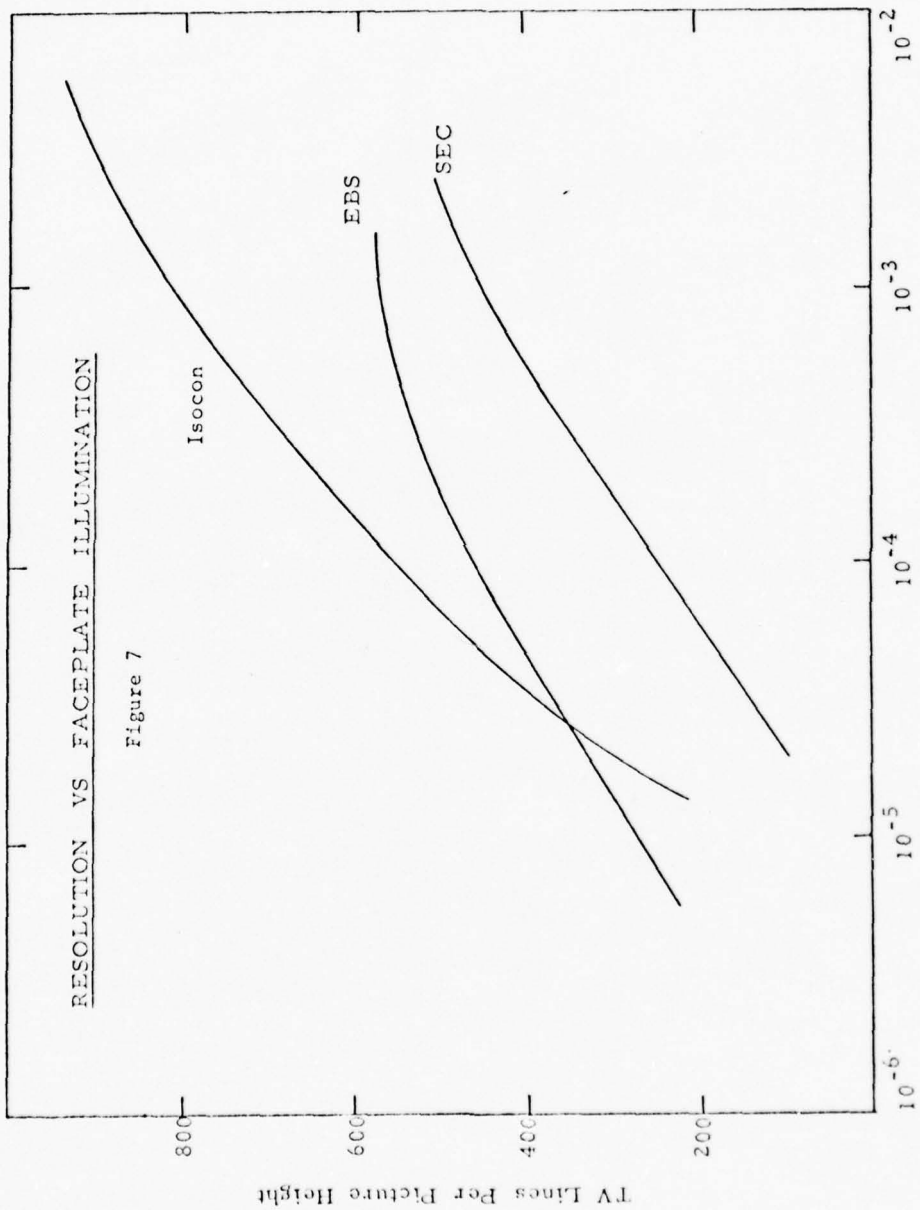

RESOLUTION VS FACEPLATE ILLUMINATION
Isocon
EBS
SEC
800
600
400
200
10^{-6}
10^{-5}
10^{-4}
10^{-3}
10^{-2}
TV Lines Per Picture Height
Faceplate Illumination - Footcandles

Figure 7

TABLE II

QUANTUM-LIMITED II/TV SYSTEMS

	SIT or EBS	SEC	Image Isocon	Silicon Vidicon	Standard Vidicon
Gain to target	2000	100	5	1	1
Advantages	High gain.	Long target retention time. Low dark noise Excellent point source imaging.	Gain of 1000 after the target. High resolution.	High-quantum efficiency.	Low cost.
Disadvantages	High cost. Low resolution.	Low signal current.	Large size, expensive yoke.	No fiber-optic faceplate.	Low overall performance.
Necessary image intensifier stages	1	2	3	4	4

The choice of an image intensifier was fairly straightforward. When a magnetically focused intensifier is used, lens coupling to the TV camera is advised, so that neither device is disturbed by the (very different) axial magnetic field of the other. The calculation of Appendix B shows that, for a phosphor which radiates uniformly over 2π steradians (nearly true), lens coupling at f/1.5 (Mende, 1971) results in 5% collection efficiency. If direct fiber-optic coupling is used, the photon transfer is then about 70% efficient. We can now make a direct comparison of two representative intensifiers, as follows:

Parameter	EMI 9694	Varo 8606 (selected)
Focusing method	magnetic	electrostatic
Number of stages	4	3
Maximum gain	2×10^6	1×10^5
Coupling method	lens, f/1.5	fiber-optic
Coupling efficiency	5%	70%
Effective gain	1×10^5	7×10^4
Center resolution	20 lp/mm	28 lp/mm
Distortion	low, S-type	21% max, pincushion
Overall size	9" x 18-1/2"	4" x 12"
Weight	84 lbs.	4 lbs.
Approximate cost	$10,000	$3,000.

Note that there is little difference in effective gain between the two intensifiers despite the difference in numbers of stages. However, the Varo holds a clear advantage in resolution, size, weight and cost, the only disconcerting specification being distortion (21%), certainly worse than that of the EMI 9694. The following alternatives were considered briefly:

1. Lens coupling from a magnetic intensifier with fiber-optic output: The acceptance (and exit) angle for modern fiber-optic bundles is so large as to nearly approximate a uniform hemispherical source, making lens coupling inefficient.
2. Fiber-optic coupling a magnetically focused intensifier to the Isocon camera: too many unknowns. The camera and intensifier typically operate with very different axial magnetic fields. If the two devices could be made to work properly in a common magnetic yoke, performance would be maximized. Unfortunately, custom development of electro-optic devices was beyond the scope of our "in-house" capabilities.
3. 'Channeltron' (Galileo Industries) plate intensifier: a marvelous device featuring high gain, acceptable resolution, zero distortion and small size. However, at $14,000 each, price was the deciding factor.

In the balance, the Varo 8606 seemed to be the most reasonable choice. A specially selected unit was obtained, having high gain (10^5), low distortion, and a particularly quiet first stage with extended red S-20 spectral response. Thus the essentially irreversible commitment was made to base the parallel-channel detection system on the RCA 4807A Image Isocon television camera, fiber-optic coupled to the Varo 8606 image intensifier.

Chapter 2

INITIAL PARALLEL-CHANNEL DETECTOR CONFIGURATION

2.1 The Isocon Camera

In order to gain a better understanding of the parallel-channel detector, a more detailed description of the operating principles of the Image Isocon TV camera is necessary. Unlike the vidicon family of cameras (including the SEC, SIT, and Plumbicon), the Isocon is a return-beam device. The magnetically focused image section (see Fig. 8) works in the conventional manner. Photoelectrons ejected from the back surface of the photocathode are accelerated toward the target, striking it with an energy of about 700 eV. Secondary electrons are emitted from the target and collected by the target mesh, leaving a net positive charge which remains well localized due to the high resistivity of the target material. The charged target is scanned by a low velocity electron beam produced by the electron gun assembly.

> "The primary (outbound) beam receives the required amount of transverse energy and the proper trajectory to pass through the beam-separation structure by means of transverse fields established by the electrostatic alignment plates and the external magnetic alignment coils. The beam emerging from the beam-separation structure is focused at the target by the magnetic field of the external focusing coils, the electrostatic field of the wall electrode (grid No. 4) and the field mesh (grid No. 5). Under the influence of these fields, each electron traverses a helical path, the paths converging at the target. The fields of the horizontal and vertical steering plates are used to deflect electrons of the primary and return beams to allow control over beam trajectory. Scanning is accomplished by transverse magnetic fields produced by the external scanning coils.
>
> "By proper adjustment of electrode voltages including those of the field mesh (grid No. 5) and grid No. 4, the beam, regardless of its lateral deflection, is caused to approach

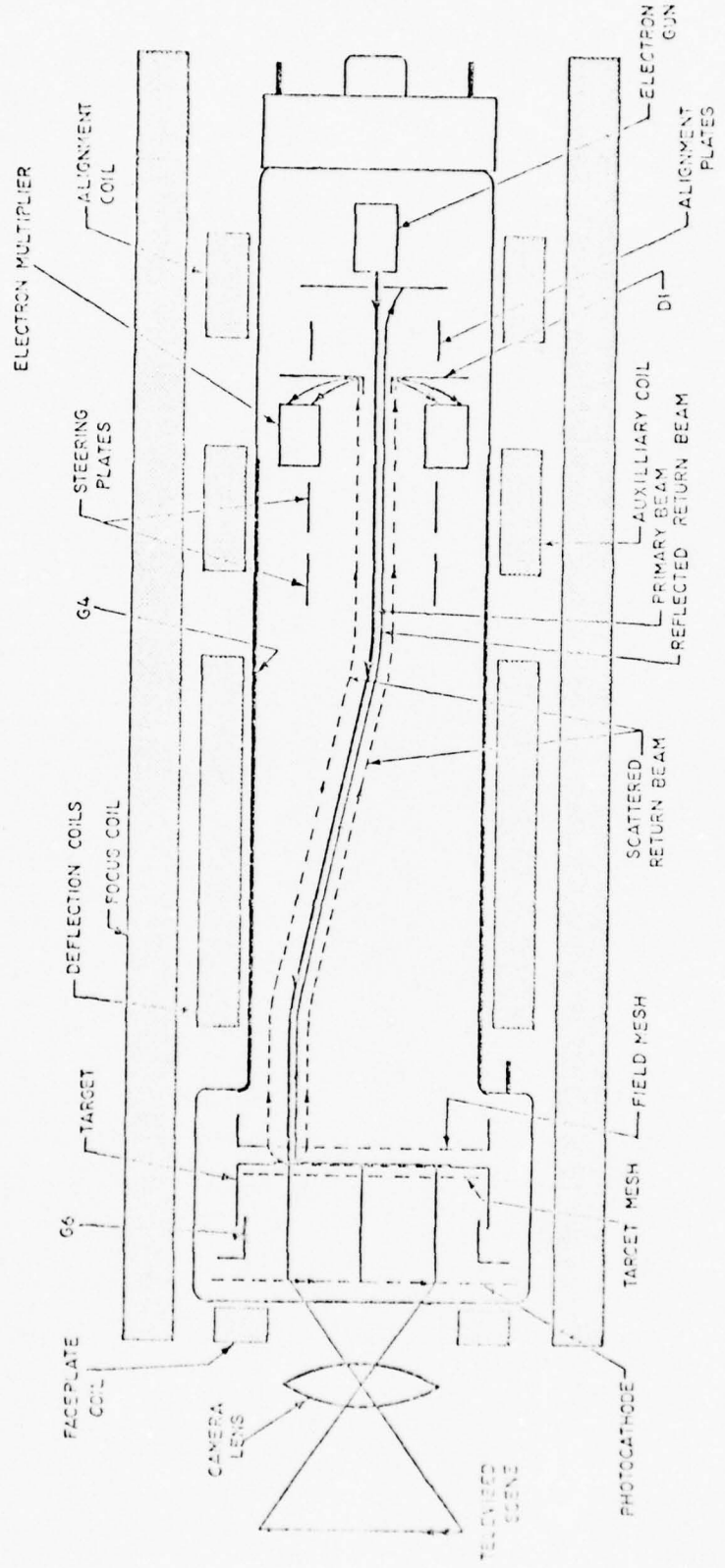


Figure 8: IMAGE ISOCON TELEVISION CAMERA

> the target at a fixed angle with zero or nearly zero velocity. The beam deposits sufficient electrons to neutralize the positive charges accumulated during the preceding frame time. Beam electrons having insufficient energy to reach the target are specularly reflected and constitute part of the return beam. Beam electrons reaching the target at positively charged areas but not captured are scattered and also become part of the return beam.
>
> "The term 'scattered electrons' applies exclusively to the non-specularly reflected electrons obtained when the beam interacts with the surface of the target and thus are distinguished from the remainder of the returning electrons which are termed reflected electrons. The number of scattered electrons obtained is at a maximum in the lighted portions (positively charged areas) and essentially zero in the dark portions of the target. (It is to be noted that although the total return beam is a minimum in the bright areas of the target where electrons are deposited, the number of scattered electrons is a maximum.) The total return beam remains under the influence of the magnetic field of the focusing coil and the electrostatic field of grid No. 4. The helices described by the scattered electron portion have greater diameters than those described by the reflected electrons. The return beam now comes under the influence of the field of the steering plates and is directed toward the beam-separation structure. The beam-separation aperture, which is located at a maximum beam diameter point, is sized to pass the reflected portion of the return beam and to capture the scattered electron portion. The scattered electrons accordingly strike the beam-separation surface, which is also the first dynode of the multiplier section. As a result, secondary emission occurs. The emitted secondaries, after multiplication, are collected by the anode as the signal output current."*

Note that there is some gain involved in the scattering process, since several electrons are scattered for every electron which reaches the target to eliminate (erase) any positive charge. The primary advantage of the return-beam technique is that it allows the use of an electron multiplier to increase the overall gain of the tube, resulting in a maximum signal current which is 1 to 2 orders of magnitude greater than that available from conventional vidicons. Due to the wide bandwidth and very low noise of the multiplier, signal quality is not degraded.

---

*From: RCA Image Isocon Camera Tube C21093 Technical Bulletin, 1968, p. 5.

2.2 Initial Design Parameters

It was noted in Sec. 1.1 that early L^3 TV systems did not provide a sufficient level of performance to meet our design requirements. Improvements were needed in several critical areas: sensitivity, resolution at low-light levels, detection of single-photon events, and dynamic range. After substantial consultation with Dr. R. K. Chang (Advisor) and Dr. P. J. Kindlmann (then Director of the Engineering and Applied Science Department Electronics Shop), a series of design decisions was made which addressed all of the major problems. Of fundamental importance was the commitment to controlling the camera sweep format with (digitally) programmable voltage sources instead of relying on deflection coil inductances to regulate the scan pattern. This required the design and construction of special voltage-to-current transducers (yoke drivers) which would have enough speed and voltage compliance to cope with the high inductance deflection coils of the Isocon yoke. This task was assigned to the Electronics Shop under the supervision of Dr. Kindlmann. Solutions to particular problems took the following form:

1. Gain. Should be acceptable using fiber-optic coupling between intensifier and camera.
2. Single-photon sensitivity. Will be maximized by adjusting the camera scan rate and raster format. The best pulse-height distribution will occur when the read-beam landing size at the target exactly matches the size of the positive "bump" caused by an intensified single-photon event. Could require deliberate beam defocusing.
3. Pulse-height distribution enhancement. If the intensifier pulse height-distribution for single-photon events

is peaked, enhancement in the Isocon might be possible via induced halation. Halation is the phenomenon wherein a bright point source is imaged as a bright spot surrounded by an annulus (halo) which is unusually dark. Normally an undesirable feature of a studio camera, halation might be induced in the Isocon by lowering the target mesh voltage with respect to the target. Ordinarily the target mesh collects secondary electrons emitted from the target. If these secondaries are instead forced back to the target, they will cause a local charge depression (halo) around a point event, which might increase the contrast in the vicinity of the photon event, making its detection more reliable.

4. Resolution. A primary factor in resolution degradation was expected to be geometric distortion in the intensifier. Electrostatically focused intensifiers exhibit a particular type of distortion known as "pincushion distortion." It was realized that pincushion distortion could be almost totally removed by properly predistorting the Isocon scan pattern. The actual technique is described in Chap. 3.

5. Dynamic range. Under certain circumstances, it is possible to increase the effective dynamic range of the TV camera by as much as 10^2 to 10^3 over the dynamic range intrinsically available from the device. This method (dubbed the "Selective-Scan Technique"), devised by the author and Dr. Kindlmann, relies on the ability

to generate a pseudo-random TV scan format. Details of the Selective-Scan Technique are given in Appendix C.

6. Camera control and data collection. Camera control was obviously going to be a rather sophisticated procedure. Further, if the system worked properly, an enormous amount of data could be generated during a single day. It therefore became clear that the entire experiment should be controlled by an on-line digital computer.

The complete project would have the form shown in Fig. 9. However, this was much too expensive and complex a task to be completed in one stage. The immediate priority was to make some initial tests which would either support or invalidate the basic design decisions.

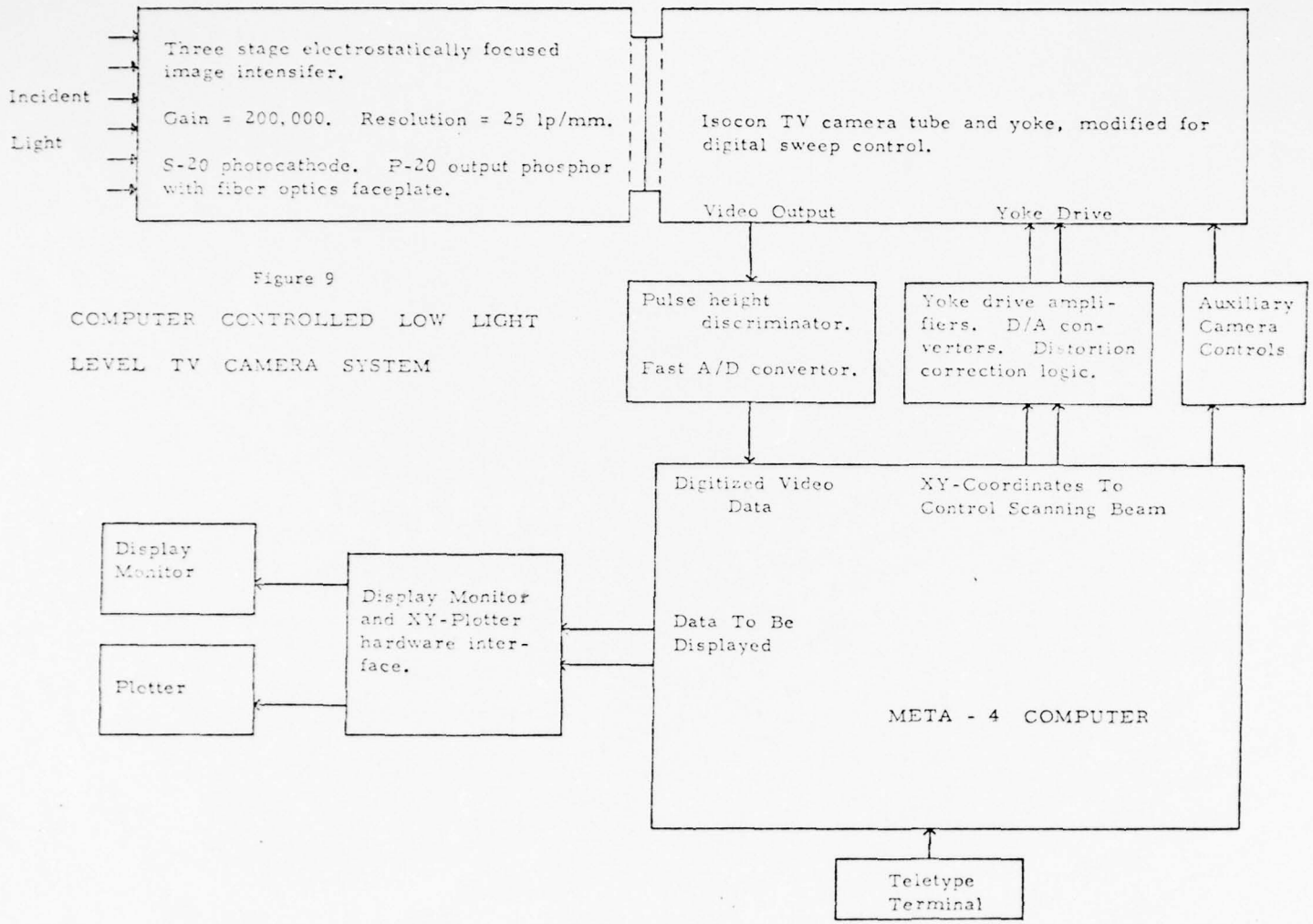


Figure 9

COMPUTER CONTROLLED LOW LIGHT LEVEL TV CAMERA SYSTEM

BEST AVAILABLE COPY

2.3 Device Testing

As a first step, the intensifier and the TV camera were bench-tested as independent devices. Problems were immediately encountered on both fronts. The intensifier was purchased with an integral power supply which accepted a 6 VDC input and supplied the internal accelerating voltage of 30 kV for the device. According to the RCA specifications, it was desirable to avoid large voltage gradients across the Isocon faceplate, so the intensifier was ordered (contrary to standard practice) with the output surface grounded. In order to prevent corona discharge from the input fiber-optic bundle of the intensifier, this surface was covered with a grounded, transparent tin oxide electrode. Despite this, we were plagued by corona discharge problems. Each small arc produced enough light to momentarily "blind" the tube, causing an overload condition from which it took minutes to recover. A long list of remedies was applied with little success. Finally the entire intensifier was pressed into a thick plastic case (open only at the rear) with a specially prepared conductive outer surface which was grounded. This reduced the arcing to a bearable level, but totally satisfactory performance was never obtained in this configuration.

The intensifier was tested for its response to single-photon events, as shown in Fig. 10. A light-emitting diode driven from a pulse generator provided synchronous illumination. The attenuated source was collimated and then masked by a small aperture in front of the intensifier. A similar aperture in contact with the output surface of the intensifier defined the field of view for an uncooled RCA 1P28 photomultiplier tube. After each light pulse, the PMT output was integrated for 10 msec (approximate lifetime of the output phosphor)

BEST AVAILABLE COPY

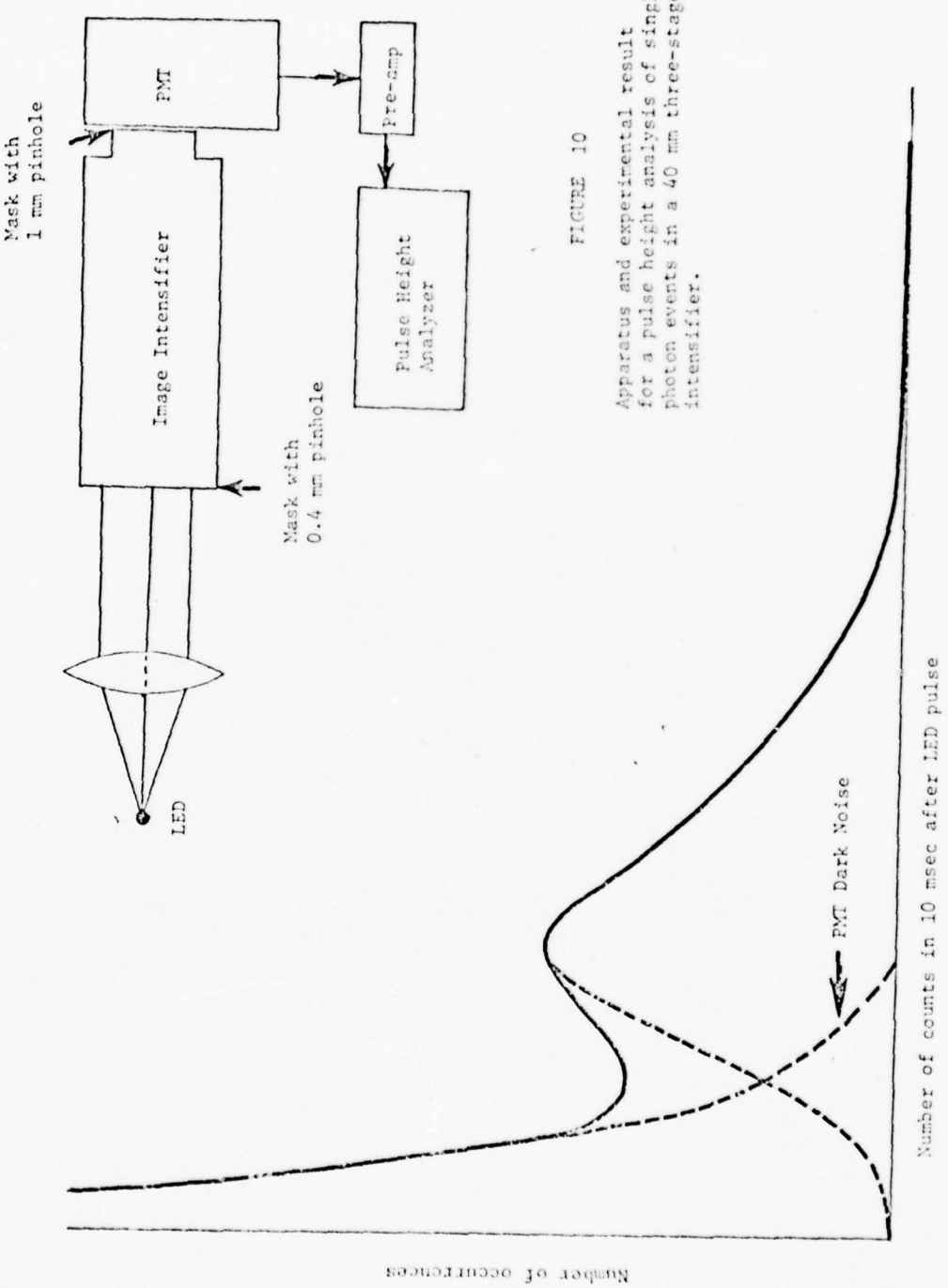


FIGURE 10

Apparatus and experimental result for a pulse height analysis of single-photon events in a 40 mm three-stage intensifier.

and sampled by a pulse-height analyzer. As shown, the pulse-height distribution has a distinct peak. Single-photon events were assured by progressively reducing the illumination level. When further reduction of illumination produced no shift in the peak position, it was known that the single-photon limit had been reached.

Testing of the Isocon camera was pursued as soon as the minimum electronic hardware was built. This included:

1. Power supply chassis providing more than 20 static, adjustable operating voltages and currents for the I^3Isocon.
2. Yoke drivers for the horizontal and vertical deflection coils.
3. Digital sweep generation card.
4. Digital-to-analog converter (DAC) cards for interface to the yoke drivers.
5. Camera head decoupling networks (all passive).
6. Video preamplifier, amplifier, DC restoring (DCR) circuit, integrator, and scope driver.

Items 1, 2, 4 and 5 have remained essentially unchanged from their first usage up until the present date. Electrical details can be found in Appendix E. Only the yoke drivers posed a significant design problem. Our initial intent was to scan each vertical line one pixel (least scan element) at a time, i.e., in a 250 line scan, each vertical line would consist of 250 separate steps, or a total of 62,500 pixels per frame. The proposed sequence of events for each pixel was:

1. Step vertical deflection yoke; wait for settling.
2. Gate camera read-beam on.

3. Integrate video for preset period (400 nsec).
4. Read-beam off.
5. Fast A/D conversion of integrated signal; then further digital processing.

The entire process takes less than 1 μsec per pixel. For this reason, the step response speed and settling time for the vertical yoke had to be very fast, despite the 160 μH yoke inductance. Thus, considerable design effort was expended on the yoke drivers. A particularly interesting technique was the insertion of a set of flexible printed circuit magnetic field sensing coils between the camera tube and its associated yoke. These coils directly sense changes in the fields which steer the read-beam, allowing more effective stabilization of the fast yoke driver circuits. In contrast to the complex yoke drivers, the sweep generation card represented a deliberately minimal effort, providing only the necessary signals for inputs to the horizontal and vertical DACs, plus control signals for the integrator, beam gate, and DCR circuits. The card was designed to be slaved to a multichannel analyzer instead of being interfaced to a general purpose computer.

The video processing circuits are of interest at this point because they represent our initial estimate of the level of sophistication required for the PCD system. As shown in Fig. 11, extensive use was made of fast (100 MHz) operational amplifiers, with very little discrete circuitry. The video preamp (Fig. 11a), which must be located as close as possible to the Isocon anode, is a current-to-voltage converter with a transimpedance of 65 mV/μA. After a secondary voltage gain stage (20x), the video signal is fed "past" the DCR circuit (Fig. 11b) to the integrator and scope driver. The purpose of the DCR circuit is to

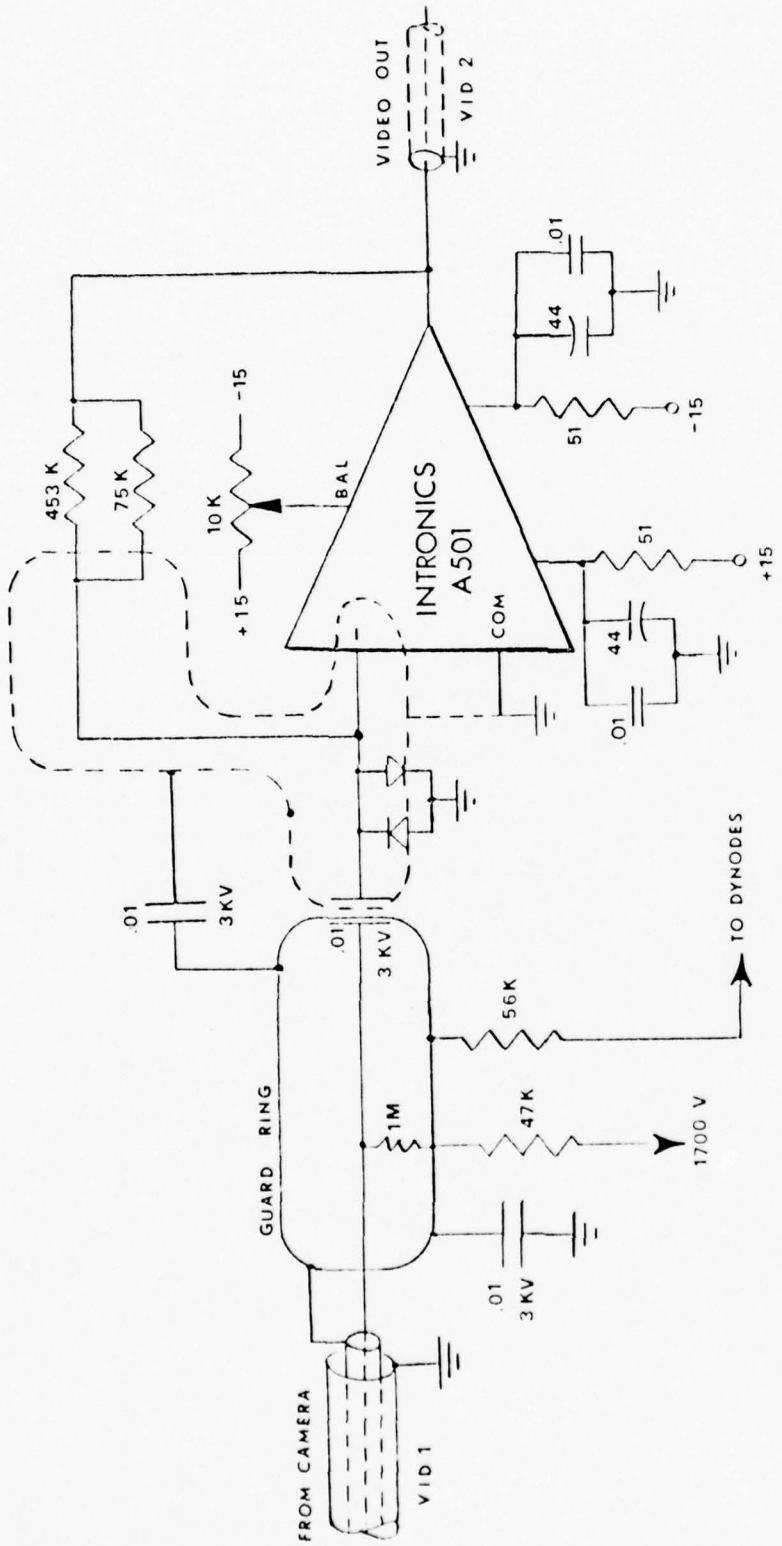


Figure 11a
VIDEO PREAMPLIFIER

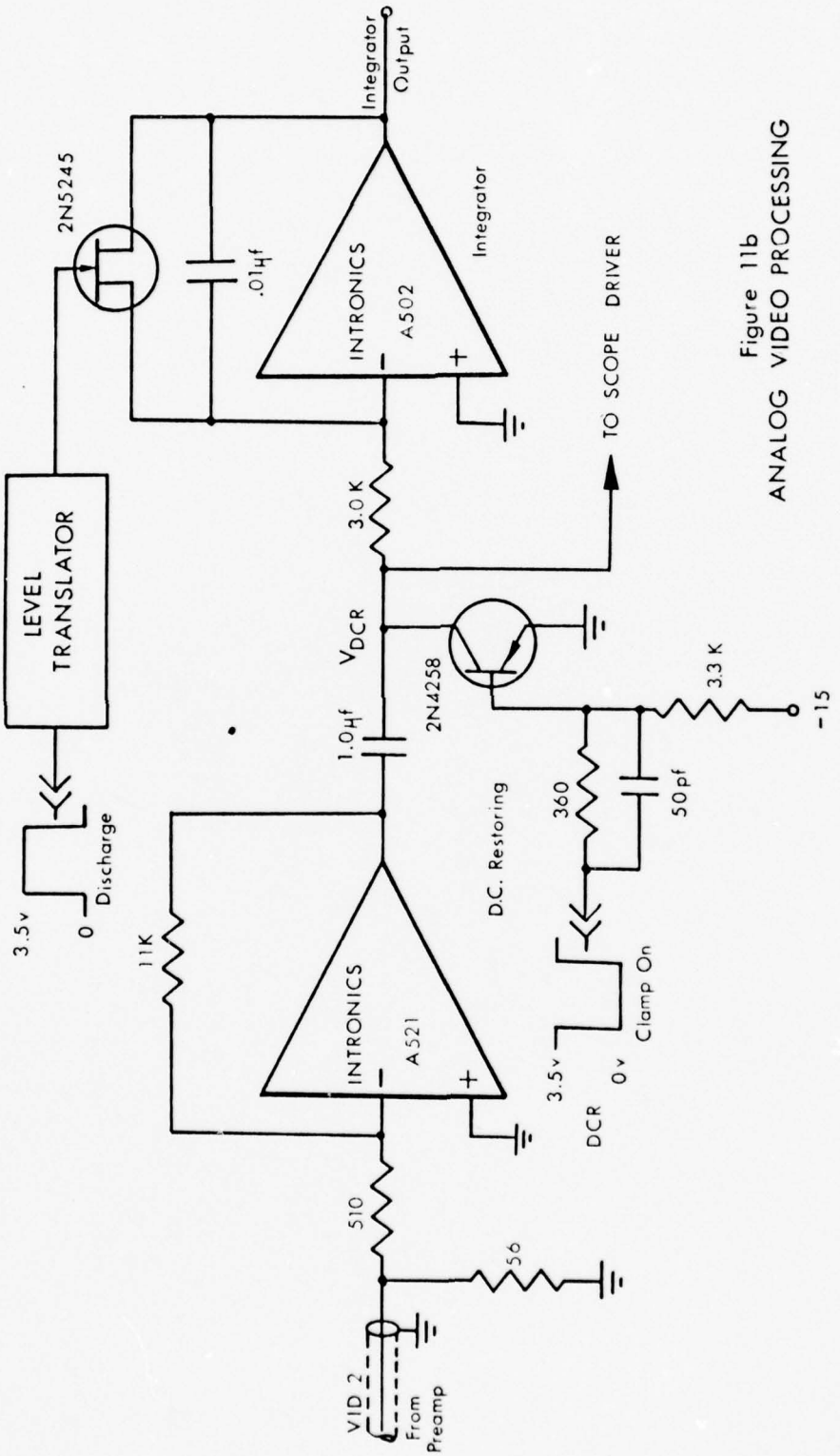


Figure 11b
ANALOG VIDEO PROCESSING

establish the true zero level of the video, despite level shifts caused by the various coupling capacitors in the video signal chain. Each time the camera read-beam is turned off, the DCR circuit clamps the video signal to some fixed level, preferably zero volts. In this case, the resultant value is different from zero by the saturation voltage of the transistor used. The purpose of the scope driver circuit (not shown) is to provide a z-axis modulation voltage (proportional to video signal strength) for an XYZ oscilloscope. By driving the X and Y oscilloscope axes synchronously with the camera deflection coils, a real-time video display is formed. A normal television display monitor cannot be used for this purpose because the camera scan format does not conform to any accepted industry standard.

The first test of the Isocon camera revealed a serious difficulty in that gating the read-beam off and on during each pixel produced "spikes" in the video output which totally obscured any true video signals. Changes in the gating procedure effected no improvement. Further, the fast steps applied to the vertical deflection yoke during each scan also produced video "feedthrough" of objectional proportions. After further investigation and consultation with RCA engineers, we were forced to abandon the pixel-by-pixel approach in favor of a more conventional scan, wherein the read-beam was left on for the entire duration of a complete, smooth vertical traverse. This yielded acceptable performance but left us in possession of a very fast yoke driver which was deliberately slowed down by an order of magnitude. Also, the DCR circuit became rather overworked since it now had only one opportunity per scan line to adjust the video zero point.

Intensifier and camera were coupled and placed in an insulated

sheet metal housing. The detector head was positioned over a Spex 1400 monochromator, as shown in Fig. 12, i.e., in the place normally occupied by a photographic camera in the Spex system. In this position, the dispersion of only one of the two Spex gratings is utilized. The detector head was cooled by an open cycle cold nitrogen gas system, manually controlled, using thermistors for temperature measurement. Initial results from this setup were very satisfactory. Resolution was acceptable at high illumination levels (about 100 TV lines) and sensitivity was good by the current standards. (It was thought that single-photon events could be observed directly, but we now believe that we were misled by the statistical occurrence of multiple events.) A few sample spectra were taken using the multichannel analyzer data collection method. The Raman spectrum of silicon (5145 Å probe) as shown in Fig. 13 is an example of this early work (Black and Kindlmann, 1973). The test conditions were:

Sample	Silicon
Probe	5145 Å, Ar^+ laser, 300 mW
Spectrograph	Spex single, 3/4 meter, plus interference filter
Dispersion	11 Å/mm (second order)
Slit	160 μm (entrance)
Duration	50 sec

Although this level of performance was well below our ultimate goals (peak intensity of this spectrum was about 20,000 counts/sec), these tests confirmed our belief in the utility of the detector and the appropriateness of our early design decisions.

BEST AVAILABLE COPY

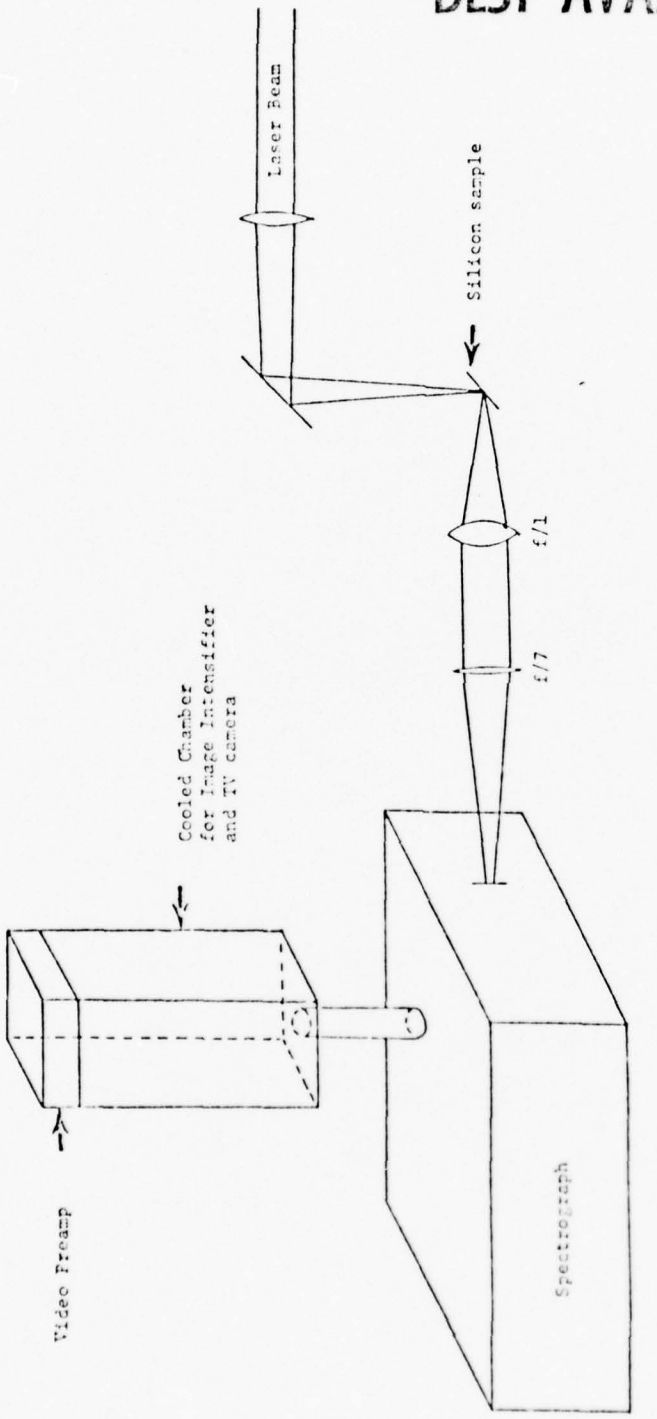


Figure 12

Schematic diagram of the parallel-channel Raman apparatus used in the reflection geometry.

BEST AVAILABLE COPY

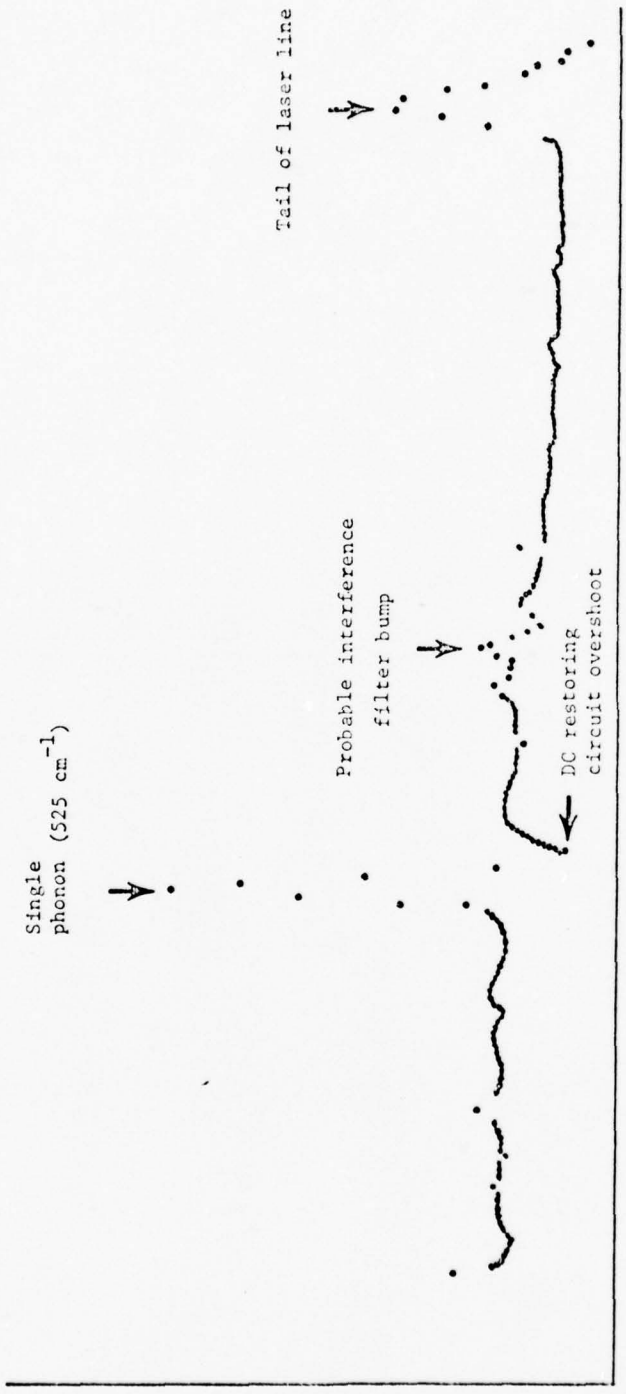


FIGURE 13

Raman scattering from silicon.
Spectral coverage is 300 Å with
maximum resolution of 100 TV lines

Chapter 3

FULL PARALLEL-CHANNEL DETECTOR IMPLEMENTATION

3.1 Performance Problems

Encouraged by the results obtained during the summer of 1973, we decided to embark on the full PCD implementation shown in Fig. 9. At same time, we were painfully aware of the problems exposed by the early efforts, such as:

1. Poor scattered light rejection. The silicon spectrum of Fig. 13 was taken with the aid of an interference filter to reduce scattered light from the probe beam. Interference filters are not always convenient or readily available for every region of interest, especially when different probe wavelengths are desired.
2. Gain non-uniformity. Gain of the I^3Isocon detector was decidedly reduced near the edges of the image. This variation of gain with radial position would make single photon counting very difficult with a standard pulse-height discriminator. In addition, a regular gain modulation was noticed at low-light levels, odd channels showing greater response than even channels.
3. DC restoring. The "negative peak" indicated in Fig. 13 was thought to be the result of inadequate DC restoring. This type of artifact is particularly undesirable since it represents a "memory" of adjacent data in the spectrum.
4. Signal-to-noise ratio (SNR) was not adequate for very

low-light level work. This was due partly to low sensitivity and partly to excessive noise in the video signal, particularly feedthrough from the yoke drivers.

5. Resolution was less than 100 TV lines at low-light levels.
6. Pincushion distortion was readily apparent, contributing further to reduced resolution.
7. An on-line computer was clearly needed in order to allow proper camera control and data acquisition/reduction.
8. The original detector housing was badly under-designed. Too much room light entered the housing and access to the intensifier and camera was severely limited. (Approximately four hours were required to remove the detector from the housing, inspect, and remount it.)
9. Some means for varying the spectral coverage of the detector was needed so that limited bandpass high resolution experiments could be performed.
10. Continued corona discharge from the front of the image intensifier degraded overall performance.

These areas of concern will be treated under four general headings: digital electronics, analog electronics, mechanical/optical considerations, and computer software.

3.2 Digital Electronics

The digital circuitry provides an interface between the (remote) computer and the basic PCD. It must also allow for "stand alone" operation of the detector when the computer is not available. The computer is a Digital Scientific Corp. "META-4" situated approximately 250 feet from the nearest lab station (see Fig. 14). The META-4 is essentially a fast IBM 1800 with the following peripheral devices:

1. 16K memory; 16 bit words.
2. Single-drive tape transport.
3. Magnetic disk drive.
4. Multiterminal communications adapter (MTCA) for controlling up to 8 serial communications devices (i.e., teletype or CRT terminals.
5. Digital I/O adapter providing up to 64 bi-directional 16 bit digital input/output ports.
6. Console teletype.
7. Card reader.

The high-speed and mass-storage capabilities of the META-4 allow us to fully utilize the desirable features of the detector. Cables and distribution hardware have been installed to allow remote operation of two fundamental devices in our laboratory. The first is the CRT terminal which allows the experimenter to communicate with the software controlling the detector. A 300 baud (30 characters per sec) full duplex serial link is used. The second device is our Digital I/O Interface, serviced by a 16 bit bi-directional bus from the digital I/O adapter of the META-4. The maximum data transfer rate is approximately 10^5 words per sec. The Digital I/O Interface is actually a custom

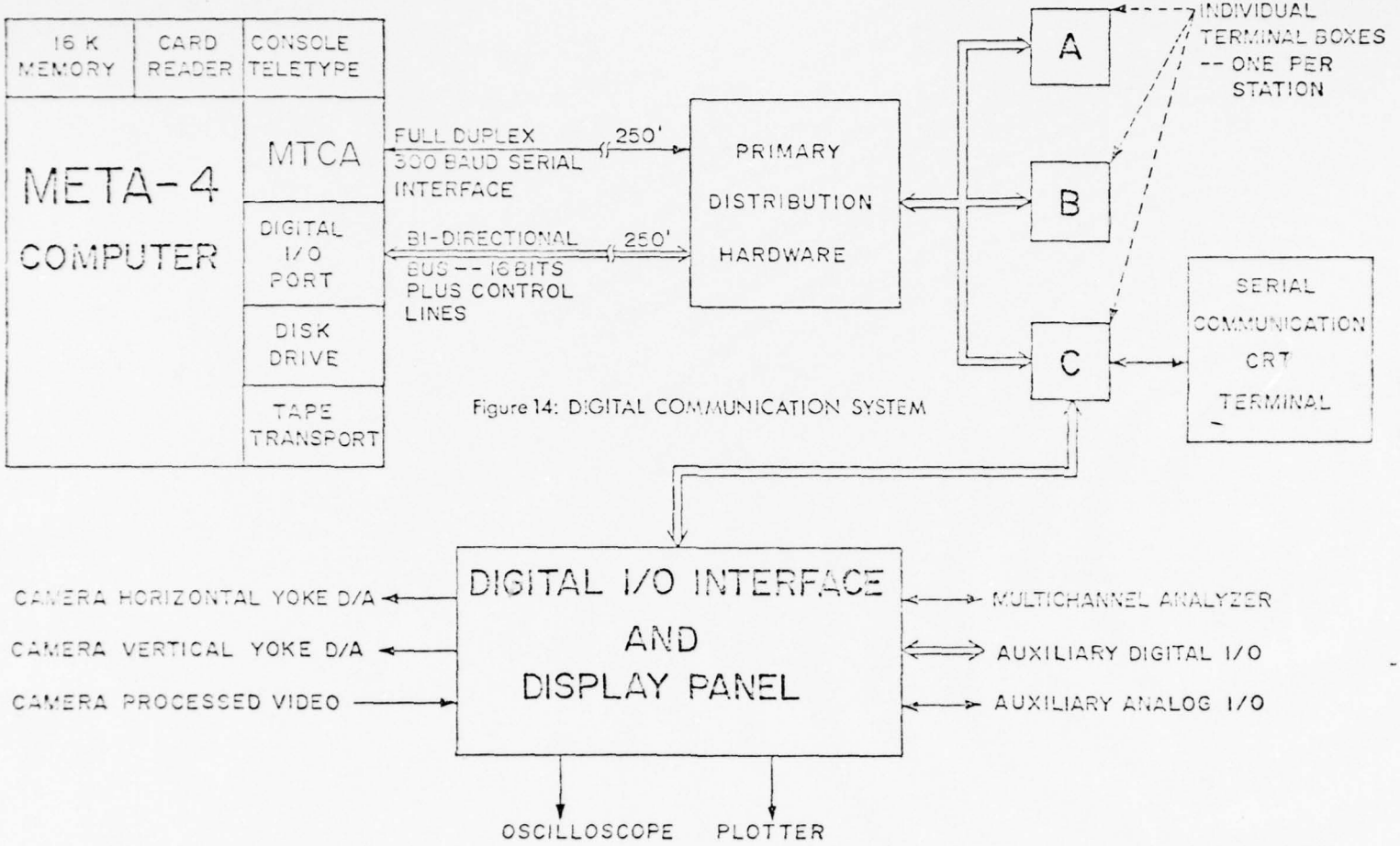


Figure 14: DIGITAL COMMUNICATION SYSTEM

BEST AVAILABLE COPY

demultiplexor and digital processor which can control a large number of peripheral devices. Some of its functions and components are:

1. Automatically generate rasters or subrasters for camera control.
2. Automatically provide timing and sequencing signals for camera analog circuits.
3. Failsafe circuitry for detection of camera sweep failures.
4. Analog discriminator and digital event counter for processing photon events "seen" by the camera.
5. Real-time (digitally controlled) clock.
6. Front panel data entry switches, data display lights, and status indicators.
7. Digital-to-analog converters and control circuitry for driving an oscilloscope or X-Y plotter.
8. Auxiliary DACs for control of experimental parameters.
9. High-speed 10 bit analog-to-digital converter (ADC) with 8 channel multiplexor, sample-and-hold circuit (S/H), and associated timing chain.
10. Auxiliary ports (input and output) for digitally accessed peripheral devices.
11. Interface for a multichannel analyzer (MCA).

In essence, the CRT terminal and Digital I/O Interface (both relatively small devices) provide the experimenter with a proxy computer at his lab station. Commands entered via the CRT terminal cause the META-4 to run experiments involving the detector head and other peripherals through the intermediary hardware of the Digital I/O Interface. Further

details concerning the Digital I/O Interface can be found in Appendix D. As noted in Chap. 2, digital control of the camera is particularly important because it allows the use of a Selective Scan-Technique to increase the effective dynamic range of the PCD.

3.3 Analog Electronics

Aside from the corona discharge problem, the Varo 8606 intensifier showed two distinctly non-ideal traits: pincushion distortion and gain non-uniformity. Corona discharge was eliminated by returning the intensifier to the manufacturer for reversal of the internal acceleration voltages. This left the faceplate at ground potential and the output surface at +30 kV (static). An additional fiber-optic bundle was cemented to the output surface (to reduce the effects of voltage gradients applied across the Isocon faceplate) and the entire assembly was fully potted in silicone rubber. The block diagram of Fig. 15 illustrates the manner in which we compensate for pincushion distortion and gain non-uniformity. The vertical and horizontal scan voltages used to program the yoke drivers are modified by a commercially available (Intronics C-100) pincushion correction module, which was designed for the correction of image distortion in wide-angle, flat-faced CRT displays. The C-100 is manually adjusted to predistort the Isocon scan pattern until it exactly matches the pincushion distortion caused by the image intensifier. Consequently, the video signal from a modified scan line corresponds to the information on a truly vertical line emerging from the spectrograph. In practice, this circuitry performs very well, as indicated by the "before" and "after" pictures of Fig. 16.

The block diagram of Fig. 15 also illustrates gain normalization, which reduces the effect of non-uniform gain in the image intensifier. The uniformly illuminated test image (flat intensity histogram) is perceived by the camera as having less intensity at the edges of the image than at the center. From the geometry correction module there exists a tertiary output, the shape of which is essentially the inverse of the

BEST AVAILABLE COPY

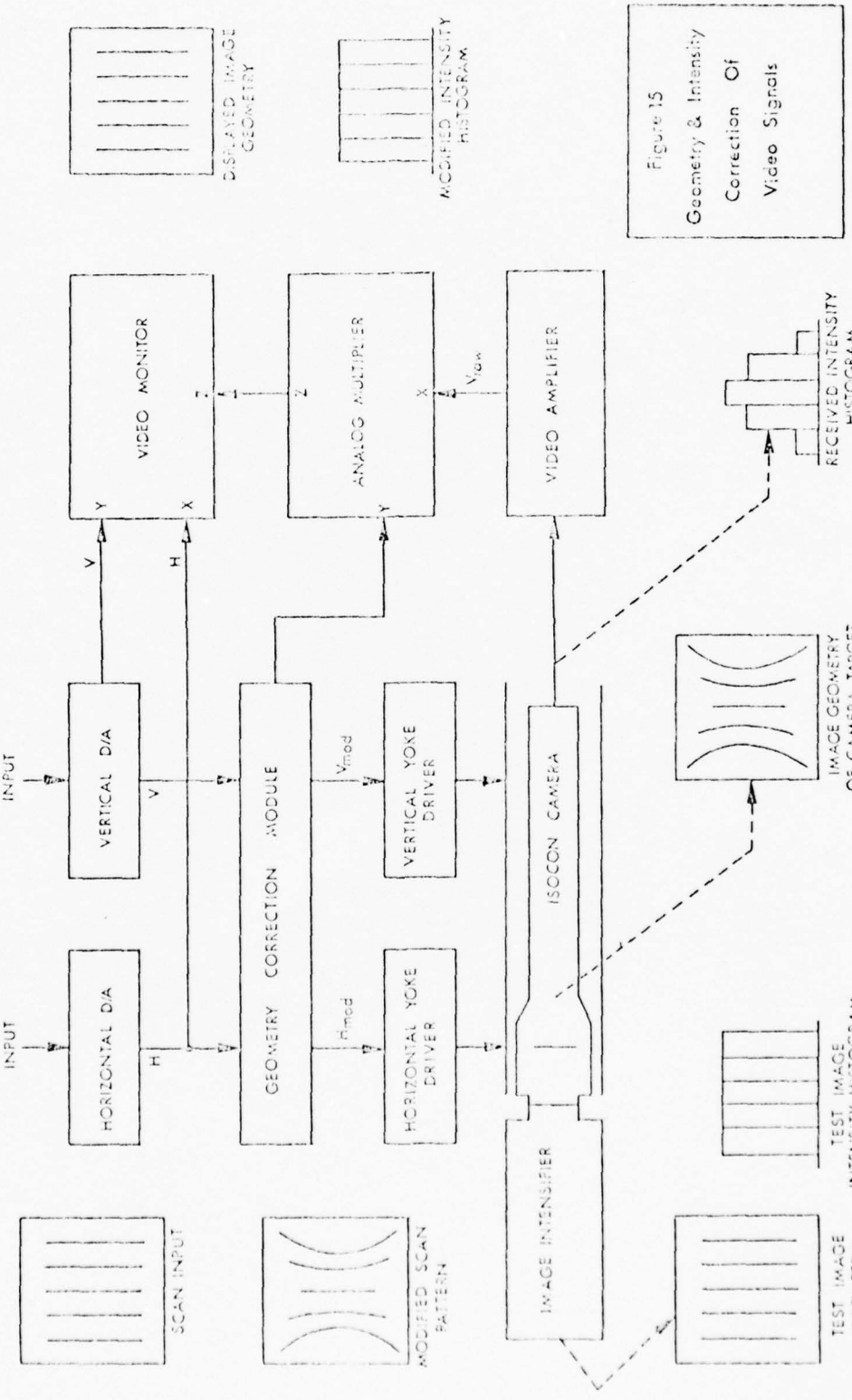
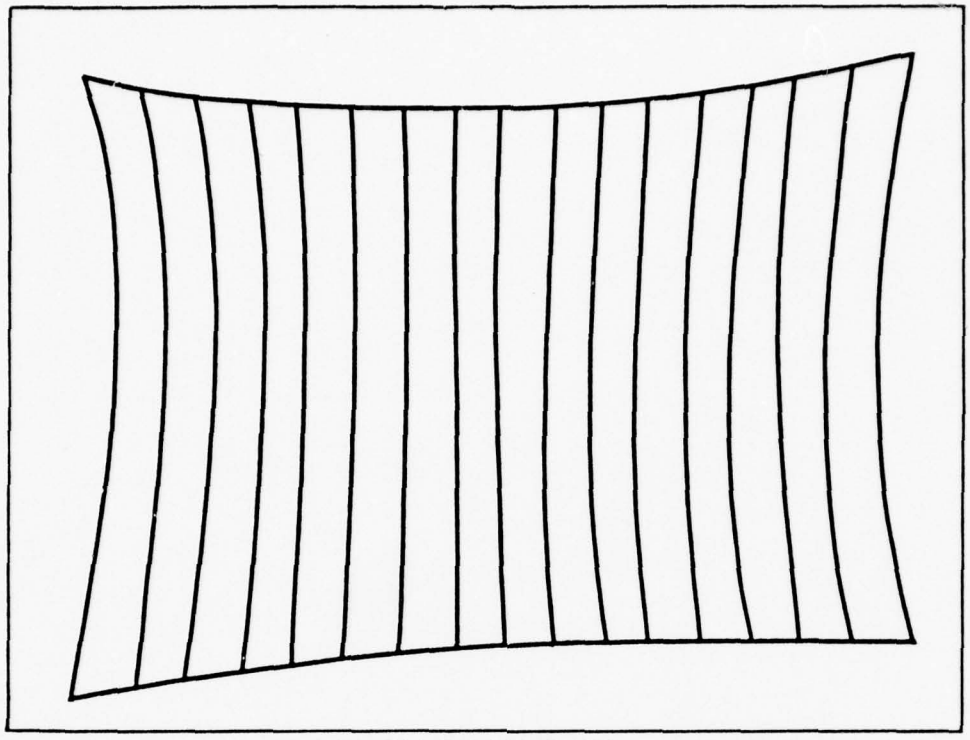
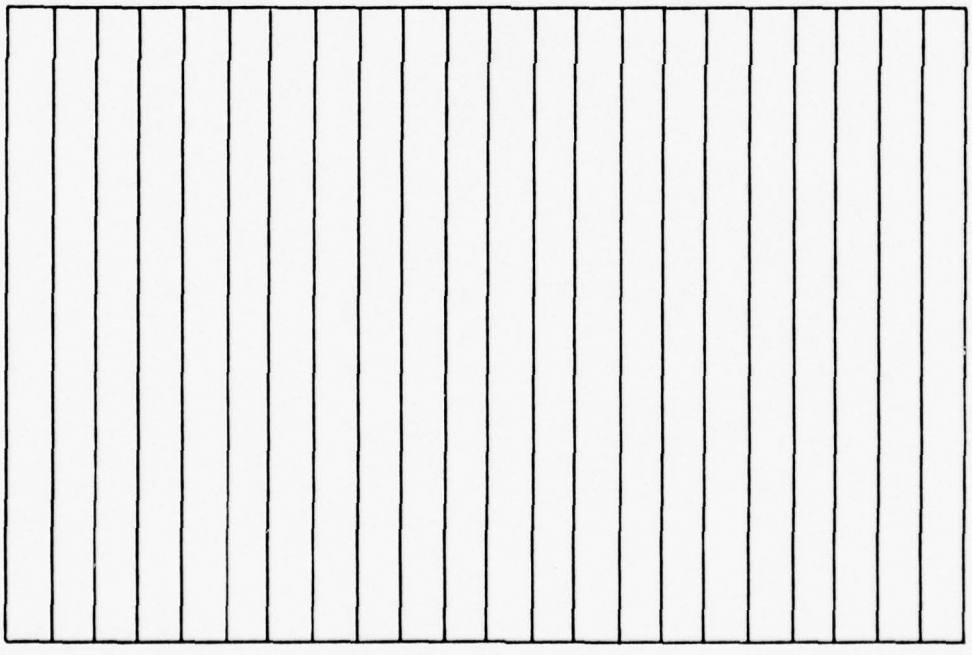


Figure 15
Geometry & Intensity
Correction Of
Video Signals



(a)

IMAGE ON TV MONITOR



(b)

ORIGINAL TEST PATTERN

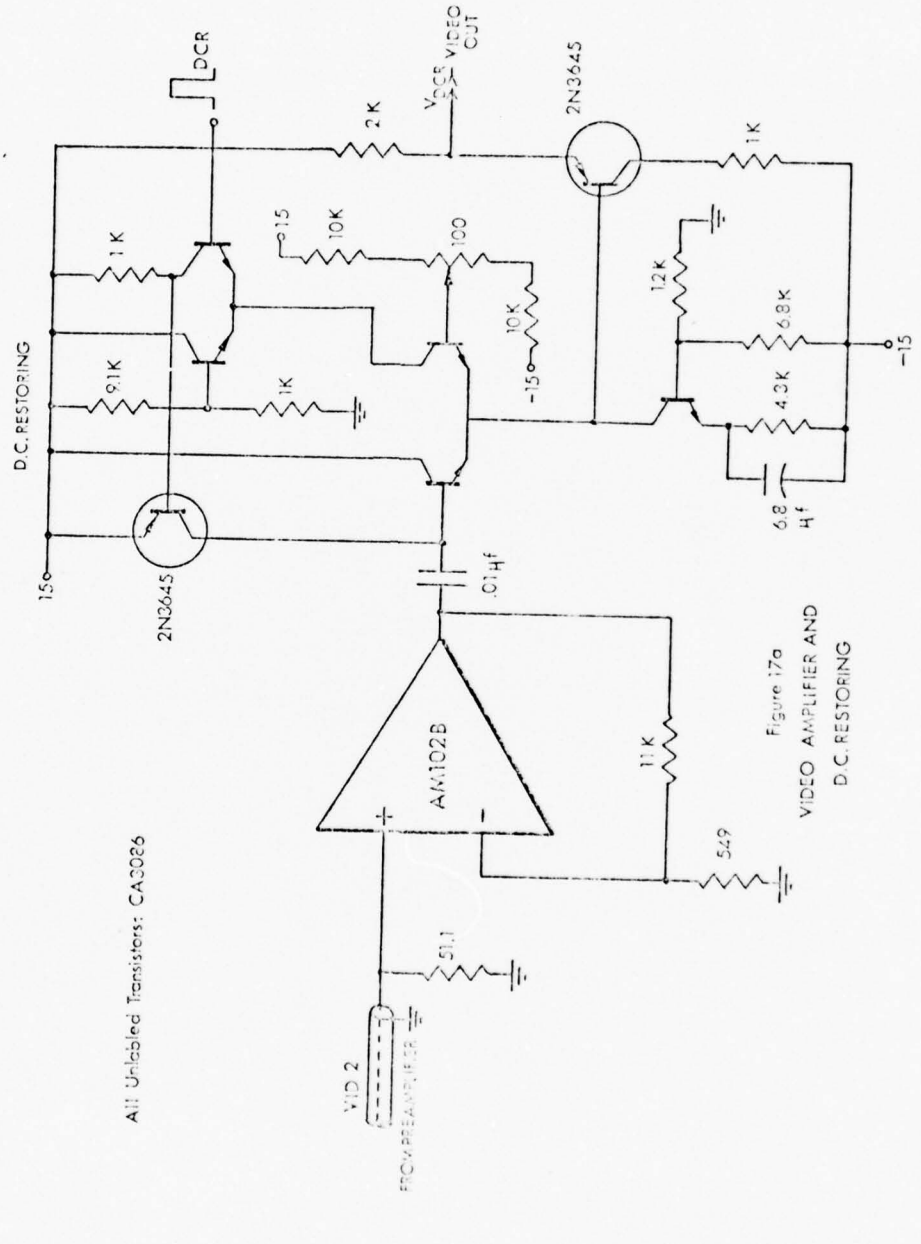
Figure 16

(a) PINCUSHION DISTORTED PATTERN AS OBSERVED ON TV MONITOR.

(b) ORIGINAL TEST PATTERN AS WELL AS OBSERVED PATTERN ON THE MONITOR AFTER GEOMETRY DISTORTION CORRECTION.

intensifier gain curve. Thus we can multiply the intensity-distorted raw video signal by this intensity correction factor and obtain a modified video signal which correctly represents the intensity of the test image. By virtue of the dual mechanisms of geometry and gain compensation, we now have a video signal which faithfully represents the input spectrographic image.

Several changes were made in the video processing circuits. The video preamplifier, integrator and scope driver were not modified, but the video amplifier and DCR circuits of Fig. 11b were replaced by those shown in Fig. 17a. It was hoped that the new DCR circuit would provide a more reliable zero reference for video signals. The analog multiplier of Fig. 17b has already been discussed.



All Unlabled Transistors: CA3026

Figure 17a
VIDEO AMPLIFIER AND
D.C. RESTORING

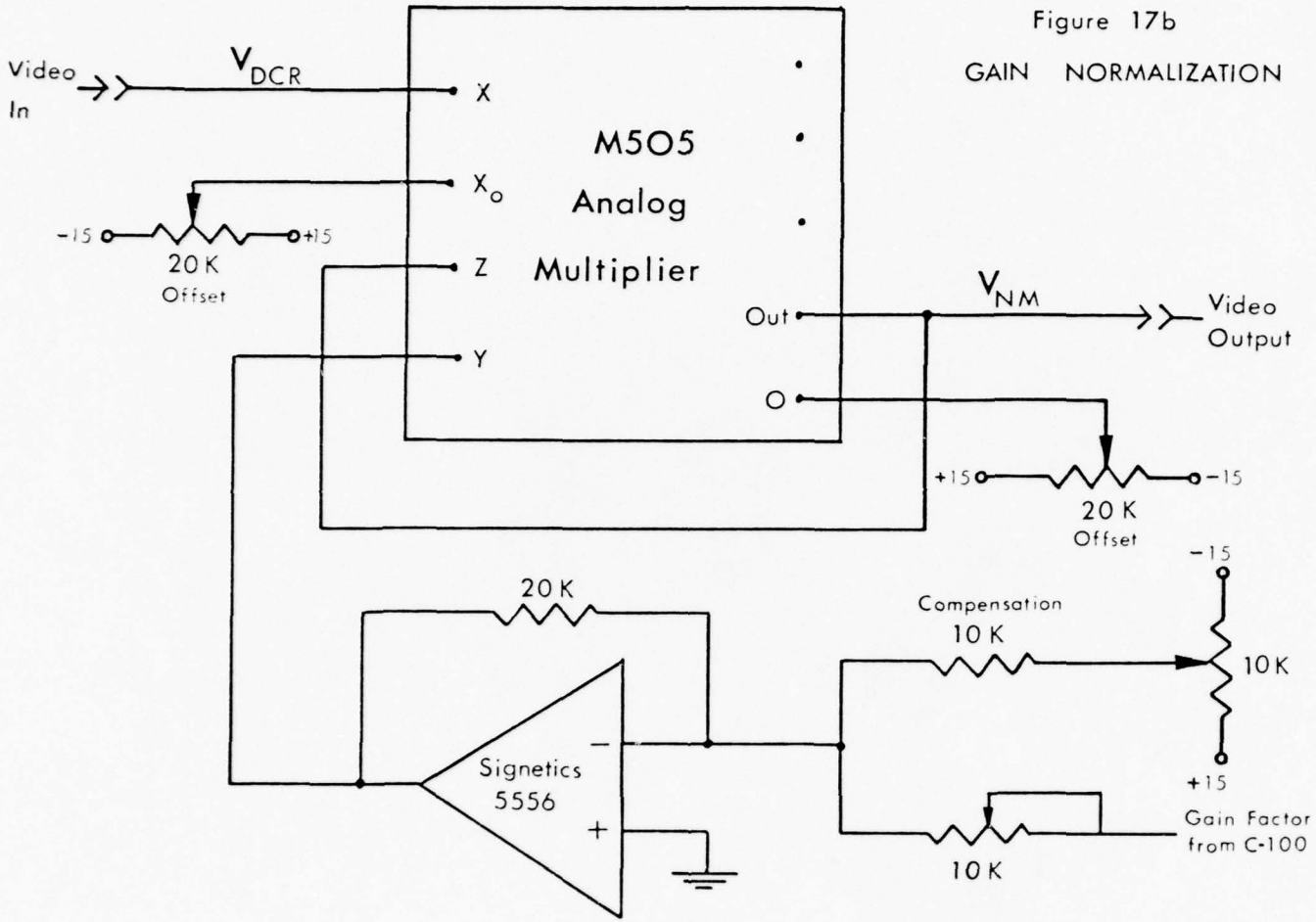


Figure 17b

GAIN NORMALIZATION

3.4 Mechanical/Optical Considerations

The most serious optical problem confronting the PCD was that of scattered light rejection. The single-grating spectrograph allowed far too much probe light to spill over into the Raman spectra. The problem was solved as soon as it was realized that the dual-tandem Spex 1400 scanning monochromator would perform very well as a dual-tandem spectrograph, provided that the intermediate and exit slits were opened wide enough. The detector would be mounted in a horizontal position facing the second-stage exit aperture of the Spex. The change to horizontal mounting was of additional benefit because it allowed for easier access to the detector head and provided a much more stable mechanical support for the entire assembly.

The pictures of Fig. 18 show the end results of our design and construction efforts:

Fig. 18a Enclosure with cover removed, showing details of the yoke clamps and intensifier supports. The intensifier is without a cooling sleeve in this photo.

Fig. 18b Closeup of the front inside surface of the enclosure, viewed from above. The groove for retaining the cover is clearly visible in the lower right-hand corner.

Fig. 18c Enclosure with the cover in place. The transfer assembly was not completed at the time of this photograph.

The main enclosure is 25 cm (10") square by 125 cm (50") long and of metallic construction with a 1" insulating layer of polystyrene foam.

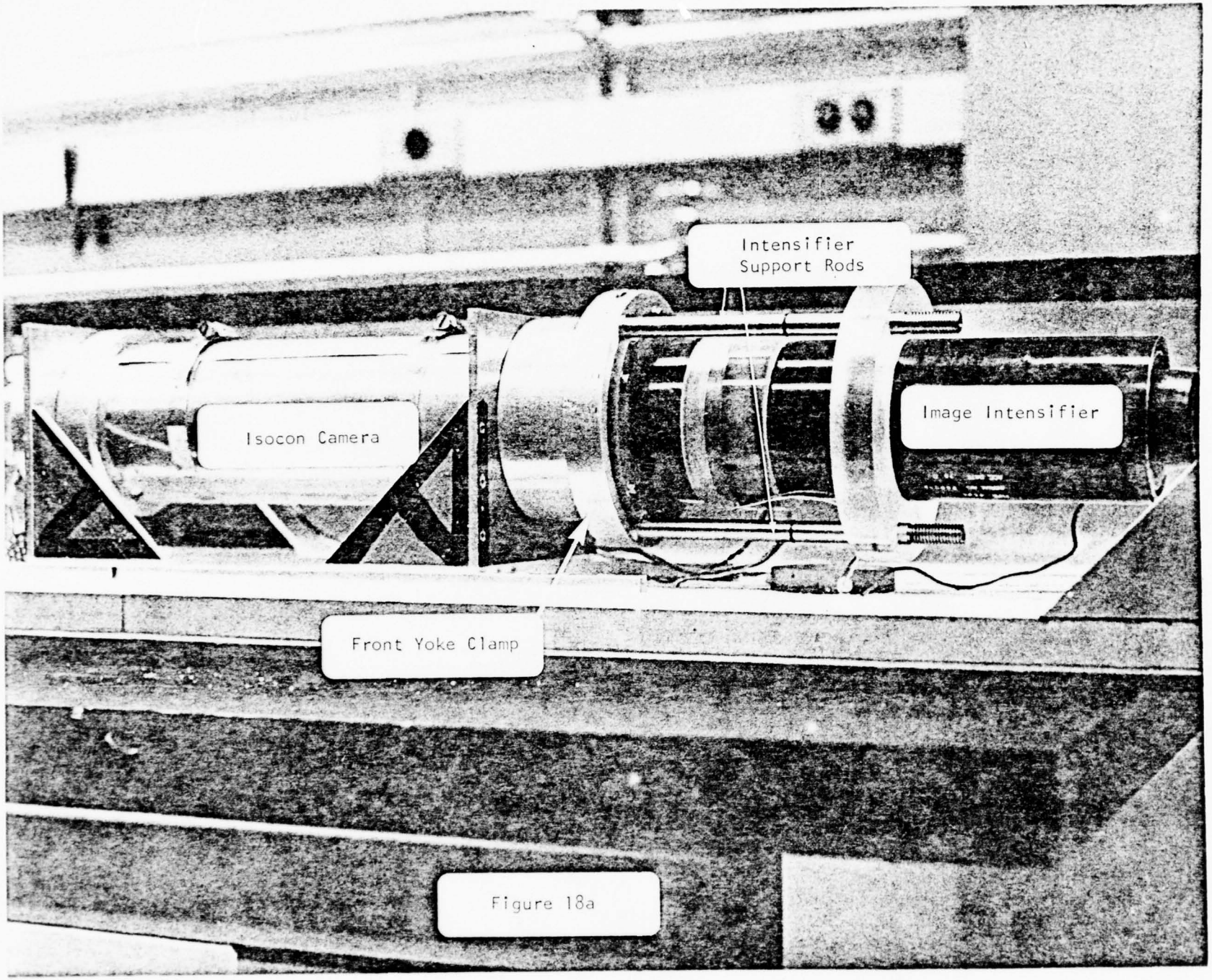

Intensifier
Support Rods
Isocon Camera
Image Intensifier
Front Yoke Clamp

Figure 18a

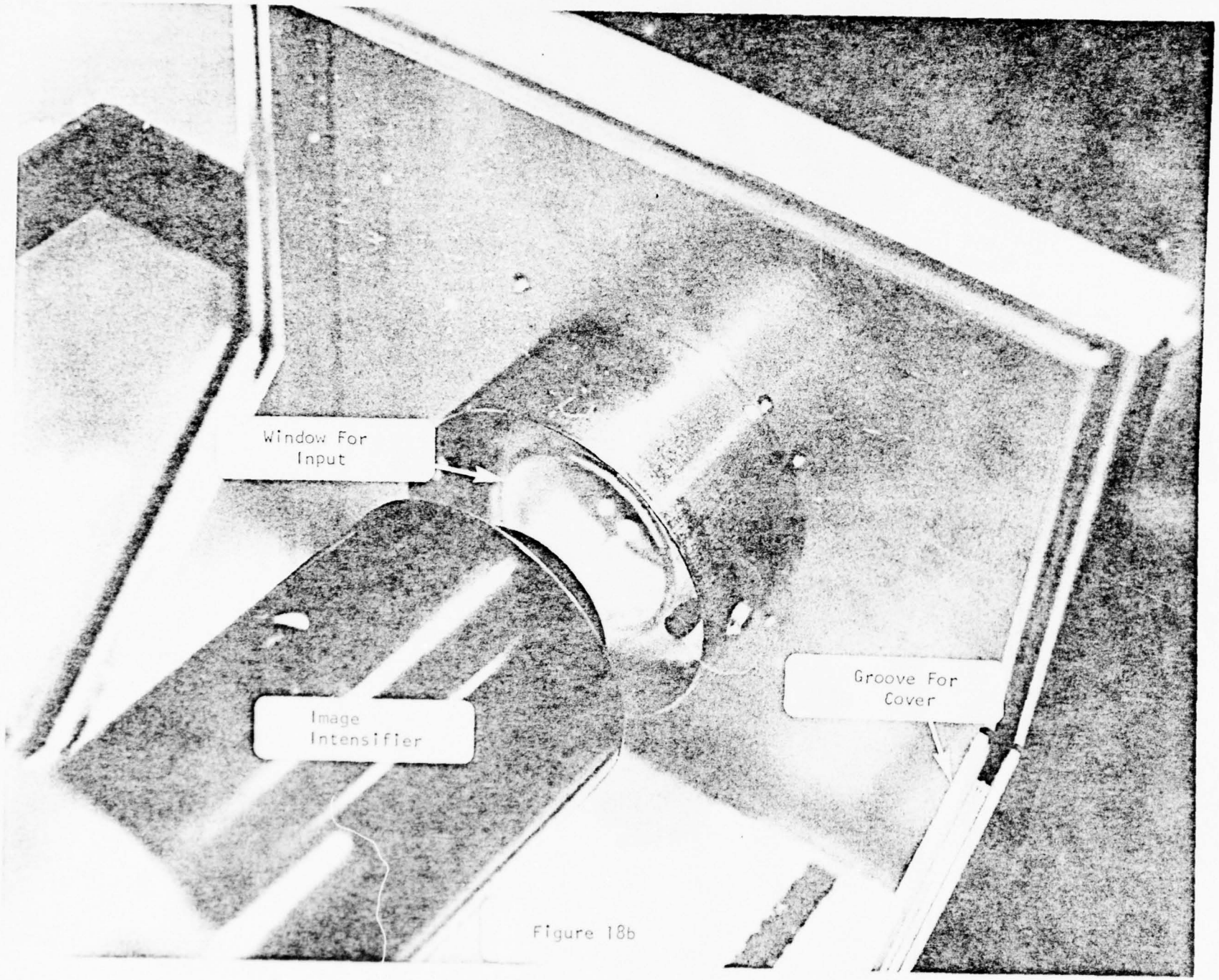


Figure 18b

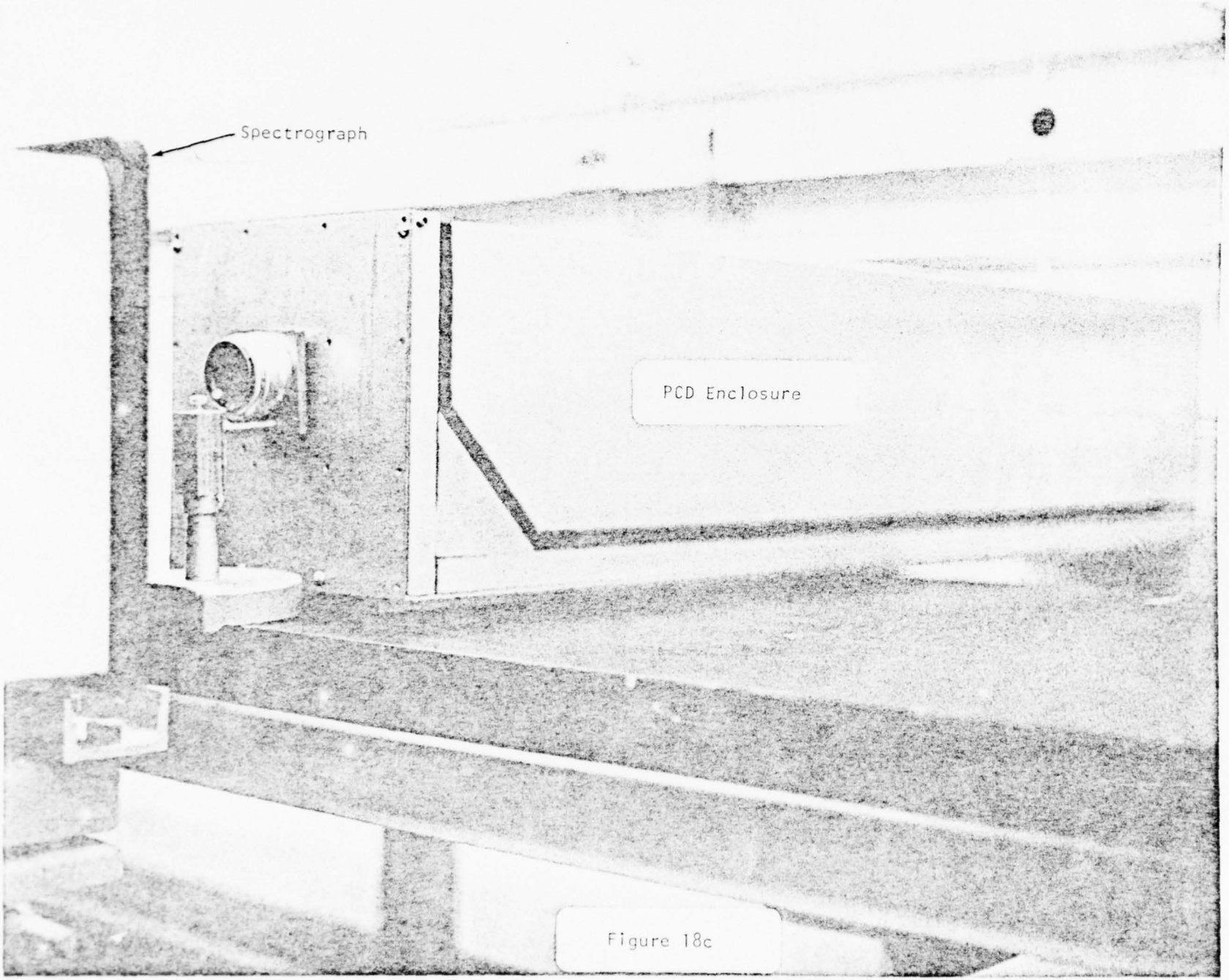


Figure 18c

The removable cover is made from 1/16" aluminum sheet with welded seams, and the edges are wrapped with 1/16" thick black neoprene which has proven to be an extraordinarily good light-sealing material. The cover has no fasteners; the wrapped edges seat in a matching groove in the enclosure body to form a "knife edge" type of light seal. This allows extremely fast access to the inside of the enclosure (about 30 sec), yet provides a seal which is completely light tight and essentially gas tight (at low pressures). The body of the enclosure was fabricated in several pieces, all joints and feedthroughs having light-tight gaskets.

The Isocon yoke is rigidly retained at both ends by two aluminum clamp rings. (No magnetic materials were used in the enclosure.) The front yoke clamp supports not only the yoke but also the Isocon camera tube and the image intensifier. Our greatest fear in designing these mounts was that misalignment or thermal expansion would cause excessive pressure at the interface between the camera and the intensifier, possibly fracturing one of the fiber-optic bundles. Basic colinearity of the two devices was assured by referencing the axis of each device to the front yoke clamp. The camera tube is rigidly mounted to this clamp, but the intensifier has a somewhat "soft" mount, allowing both axial and rotational movement. Support for the intensifier is provided by three 1/2" dia stainless steel rods protruding from the Isocon yoke clamp. The plastic intensifier clamp slides on these rods, allowing free movement during thermal cycling of the detector, which is periodically cooled to -25°C. Adequate faceplate pressure (about 3 kg) is insured by springs located at the forward end of each rod. Of special importance is the fact that the intensifier clamp ring is soft mounted

to the stainless rods, riding on three "O" rings which permit a slight rocking motion of the entire device. This allows the output surface of the intensifier to seek exact alignment with the input surface of the camera tube when initial contact is made between the two fiber-optic bundles. A thin layer of index matching oil is used between the two bundles.

Cooling is accomplished by an open cycle cold nitrogen gas system. A cartridge heater vaporizes liquid nitrogen in an external dewar, forcing the cold gas into the PCD enclosure through two separate input lines with individual control valves. One line directs coolant to the camera, which is usually operated at approximately 0°C (measured on the bulb near the target ring). This low operating temperature improves the ability of the target to retain signals for longer periods than the standard 1/30 sec required for studio usage. In order to limit the possibility of thermal shock and provide additional cooling of the yoke, the gas circulates through internal passages in the front yoke clamp before being directed into the annulus between the yoke and the camera tube. Exhaust is at the rear of the camera.

The second coolant line is dedicated to the intensifier, which should be maintained near -25°C for best gain and low dark noise. Unlike the camera which dissipates up to 50 W in operation, the intensifier dissipates very little energy. Originally the intensifier was cooled by forcing the ambient temperature in the entire enclosure down to -25°C. This proved to be rather inefficient, so a cooling sleeve was added. A copper cylinder of 1/32" wall thickness was wound with approximately 10' of 3/8" dia copper tubing and then covered with a layer of insulation. Cold gas passes through the sleeve assembly for

proper thermalization and then flows over the intensifier faceplate and back through the space between the intensifier and cooling sleeve, exiting at the rear of the intensifier. This has proven to be a much more efficient scheme for cooling the intensifier, reducing nitrogen usage by about 40%. (Liquid nitrogen consumption is 5 liters/hour.) Diodes (1N4446), used as temperature sensors at several points on the intensifier and camera tube, were chosen because they are linear, and fairly robust (compared to the previous thermistors). Forward biased from a constant current supply, the voltage drop across each diode shows a temperature sensitivity of about 2 mV/°C. The actual voltage is scaled and offset so that a direct reading in °C is obtained on a digital panel meter. Long term accuracy is better than ± 1°C.

The structure connecting the spectrograph to the detector enclosure (transfer assembly) contains several devices, each of which may be operated from outside the transfer assembly. Replacing the normal Spex exit slit is a larger slit assembly designed to allow an aperture of up to 4 cm x 4 cm. Light passing through this aperture is focused on the intensifier faceplate by a relay lens mounted on an externally operated precision traverse. Attached to the front of the camera enclosure (but still inside the transfer assembly) is a 62 mm dia electromechanical shutter (Vincent Associates 262X2H05) which is controlled from the operator's console of the PCD system allowing the detector head to be optically isolated from the spectrograph whenever necessary. By suitable choice of the relay lens, it is possible to attain magnifications of 0.5 to 5, thereby providing a means for altering the spectral coverage (hence spectral resolution) of the PCD.

3.5 Computer Software

It is axiomatic that software will fill whatever space is available. In this case, 16K-words of memory are available and there have been some problems in keeping the program within this boundary. Details of the actual programs are relatively unimportant, but the operating characteristics of the system are of interest. The operator communicates with the computer via a CRT terminal. A command structure has been implemented which allows the following procedures:

1. Specification of PCD parameters: sweep speed, raster format, type of data acquistion (photon counting or integration), duration of the experiment, operation of external devices, etc.
2. Operation of an oscilloscope display, point plotter, or incremental plotter.
3. Creation, erasure, storage and retrieval of data files. Each data file is identified by a coded title and contains all information pertinent to a single data run: identifier, operator comments, camera operating parameters, acquired data.
4. Mathematical manipulation of data vectors:
   a) Multiply, divide, add, subtract; operands are two vectors, or a vector and a constant.
   b) Fourier transform, inverse transform, differentiation, interpolation; single-vector operations using a standard FFT package.
   c) Integration, exponentiation, log, antilog; single-vector operations.

In practice, the operator defines the relevant PCD operating parameters and also defines a data file to hold the results of the experiment. Each data file (1024 words) has room for 850 characters of free form text to be used for notes and comments. In this way, comments can never be lost or mistakenly associated with the wrong experiment. A typical experiment might be set up as follows:

Instruction	Results
256HOR	256 channel spectrum
512VERT	512 pixels per vertical line
4000CLK	4 MHz step rate, about 1/20 sec per frame
30SEC	30 sec exposure
100DLAY	100 msec between frames
0LASR	use laser 0 = Ar^+ cw laser
INTC	integrate data

On command, the computer executes the predefined experiment. During each frame the camera scans 256 vertical (spectral) lines, electronically integrating each one. At the end of each line, the integrated value (intensity) of the line is converted to a 10 bit binary number which is sent to the computer. Then the integrator is cleared and the next line is scanned. The computer accumulates data (as 32 bit integers) in 256 "channels," performing the same function as a multichannel analyzer. The computer continuously monitors the progress of the experiment, drives the necessary display (usually an oscilloscope which shows the accumulating histogram) and watches for various failures. At the end of the experiment, the data is converted into standard floating point format (FORTRAN compatible) and stored in the selected data file, which is copied onto the disk (holds 150 files) and

later onto magnetic tape (up to 4000 files/tape) for permanent storage. The file may be recalled at any time for examination, mathematical processing, plotting, etc.

3.6 Results

The developments described in the preceding four sections occupied the author, a part-time assistant (W. Nagorski), and some members of the Electronics and Machine Shop staff (periodically) for almost two and one-half years. In many respects the program was a complete success. All of the mechanical/optical goals were realized. The computer software/digital electronics subsystem proved to be a powerful tool for speeding data acquisition and performing on-line data reduction. The performance of the optoelectronic/analog electronics subsystem was considerably improved, but there were still serious shortcomings. The pincushion distortion correction circuitry worked exceptionally well, but resolution at low-light levels was still limited to about 80 to 100 TV lines per raster height. The periodic gain variation noted earlier was found to be caused by the difference in read-beam characteristics between "up" scanning and "down" scanning. The digital circuitry was changed to produce a sawtooth vertical sweep waveform (linear sweep with flyback) instead of a triangle wave, eliminating the problem entirely.

Gain-uniformity correction via analog multiplication proved to be a bad idea. The dynamic range of the multiplier unit limited the performance of the entire video processing chain; yet its only benefits were cosmetic. When using the combined gain/pincushion correction circuitry of Fig. 15, it was possible to perform all of the normalizations intended. However, the signal-to-noise ratio at the edges of the video image was noticeably degraded. A more careful consideration of the operating principles of the image intensifier revealed that an error had been made in treating pincushion distortion and gain

non-uniformity as separate problems. In fact, the primary cause of gain non-uniformity in the Varo 8606 is pincushion distortion. To understand this conclusion, it must be remembered that pincushion distortion is the result of a radially dependent magnification of the image, least magnification occurring at the center. The effect is identical to that obtained by projecting a flat, square grid onto a spherical surface (which is essentially what happens in the electron optics of the intensifier). Now suppose that each square in our grid pattern contains one unit of photon flux. Squares near the center fall on the spherical surface at nearly normal incidence, hence at unity magnification. Squares near the edge of the pattern fall on the spherical surface at decidedly non-normal incidence angles. These projections result in distorted, elongated shapes, i.e., magnification greater than unity. For these squares, we have taken one flux unit per square (intensity = 1 unit flux/square) and projected it into an area of $(1+\varepsilon)$ square. So the intensity on the spherical surface near the edge of the pattern is I = [1 unit flux/$(1+\varepsilon)$ squares], i.e., less than the center intensity. Q.E.D. Geometrically induced pincushion causes an apparent intensity gradient or gain non-uniformity.

From the point of view of the camera, the pixel (square) size is definied by the raster format and remains constant throughout the scan. Typically the read-beam is adjusted for best center performance, ideally creating a beam landing area roughly the same as the pixel area. However, at the edge of the pincushion distorted scene, the pixels defined by our (deliberately) distorted scan pattern become much larger than pixels at the target center. Since the beam landing area is held constant, some areas at the edge of the target are never touched by the

beam. Information is lost, and video output is reduced. Post-multiplication of this sagging output is of little benefit since this also multiplies the (nearly constant) noise content of the signal. Uniformity is achieved, but the SNR gets noticeably worse at the edges of the scene. The ideal solution would be to increase the beam landing area exactly as fast as the pixel size increases. No information would be lost, and a perfect deconvolution for the combined effects of geometric distortion would be attained. Unfortunately, the Isocon is an exceptionally difficult camera with which to implement dynamic beam defocusing. After much discussion with the staff at RCA, the idea was abandoned.

Other expected improvements failed to materialize. Induced halation efforts proved to be totally ineffective; the camera tube was removed and tested, only to find that an internal short existed between the target mesh and the target. The tube is normally operated with these two connections externally shorted, so this had no effect for studio usage, but the induced halation experiment was thoroughly dead. (Cost of a new camera tube would have been approximately $5,000.) Finally, low-light level performance was still below our expectations: 1) The DCR circuit was not quite precise enough to eliminate all artifacts in weak spectra and, in addition, had an unacceptable thermal drift coefficient. 2) Signal-to-noise ratio was still low, possibly due to the analog multiplier. 3) More flexible amplifiers were needed so that video gain could be optimized for every experiment. In short, we had a very powerful data-acquisition system, but the electro-optics and video processing systems still had nontrivial shortcomings.

The critical analysis given above should not be misconstrued to

mean that progress was negligible during this period. On the contrary, the PCD was beginning to attain the status of a useful laboratory instrument for weak spectra. The histogram of Fig. 19 shows the second-order optic phonon band in silicon. The experimental conditions were:

Sample	Silicon, reflection geometry
Probe	4880 Å, 100 mW
Spectrometer	Dual Spex (1400) 3/4 meter
Dispersion	5.5 Å/mm (second order)
Slits	Entrance 600 μm, center 2 mm, exit 10 mm
Duration	10 sec data acquisition
	9 sec background subtraction
Center wavelength	5118 Å.

Note that the histogram of Fig. 10 (same sample) covers this spectral region (and more) but does not show the two-phonon feature, even though the total input energy to the early run was an order of magnitude higher than for Fig. 19. The peak signal intensity of Fig. 19 is thought to be approximately 500 counts/sec.

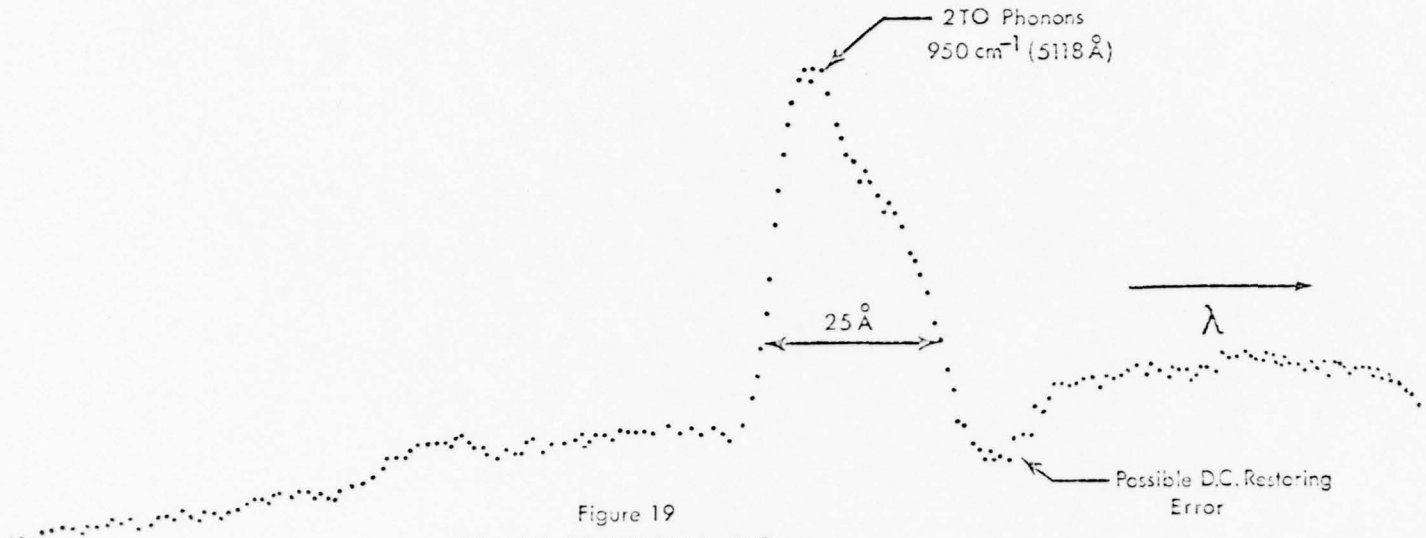


Figure 19
RAMAN SCATTERING FROM
SILICON, $\lambda_o = 4880$ Å

Chapter 4

FINAL CONFIGURATION AND PERFORMANCE CHARACTERISTICS

4.1 Introduction

The most obvious weakness of the PCD system described in Chap. 3 was the analog video signal processing circuitry. Analysis of these circuits indicated that system response began rolling off at just over 1 MHz. A bandwidth of 10 MHz was required to avoid limiting the maximum performance of the Isocon camera (1200 TV lines/raster height). To be useful, this bandwidth would have to be preserved throughout the entire video chain, from the first video amplifier, to the scope driver. If the video monitor does not give a faithful display, it is almost impossible to optimize the camera controls. The additional bandwidth would certainly make us more sensitive to high frequency noise, so special care would have to be taken, especially for the video preamplifier. A discussion of the actual implementation follows.

4.2 Implementation

The video preamplifier was particularly worrisome. The combination of anode/anode-lead capacitance (about 30 pf) and high input impedance meant that even a very fast operational amplifier such as the Intronics A521 (100 MHz) would not deliver the required gain and bandwidth as a simple current-to-voltage converter. It was decided to use a discrete component approach based on an amplifier (7631A) given to us by Westinghouse. This amplifier was designed for use with the SEC camera tube (maximum output current 400 nA) instead of an Isocon camera (10 μA). This seemed to be a very favorable mismatch since our primary concern was the low-light level performance of our camera. The Westinghouse specifications were:

Bandwidth	3 dB down at 30 MHz
Noise current	4.3 nA RMS at 10 MHz with 33 pf target capacitance
Voltage gain	9
Input impedance	50 Kohms
Maximum output	200 mV

A special "mother board" was designed to house the W7631A, including on-board voltage regulators and a metal cover which completely enclosed the preamplifier. Bench tests of this unit proved very satisfactory.

The video preamplifier is followed by two supplemental gain stages, A2 and A3. Each amplifier (Fig. 20a) has two gain settings determined by on-board reed relays. The on-board relays were chosen to keep all leads as short as possible, allowing full utilization of the available amplifier bandwidth. Gains are selected from a single

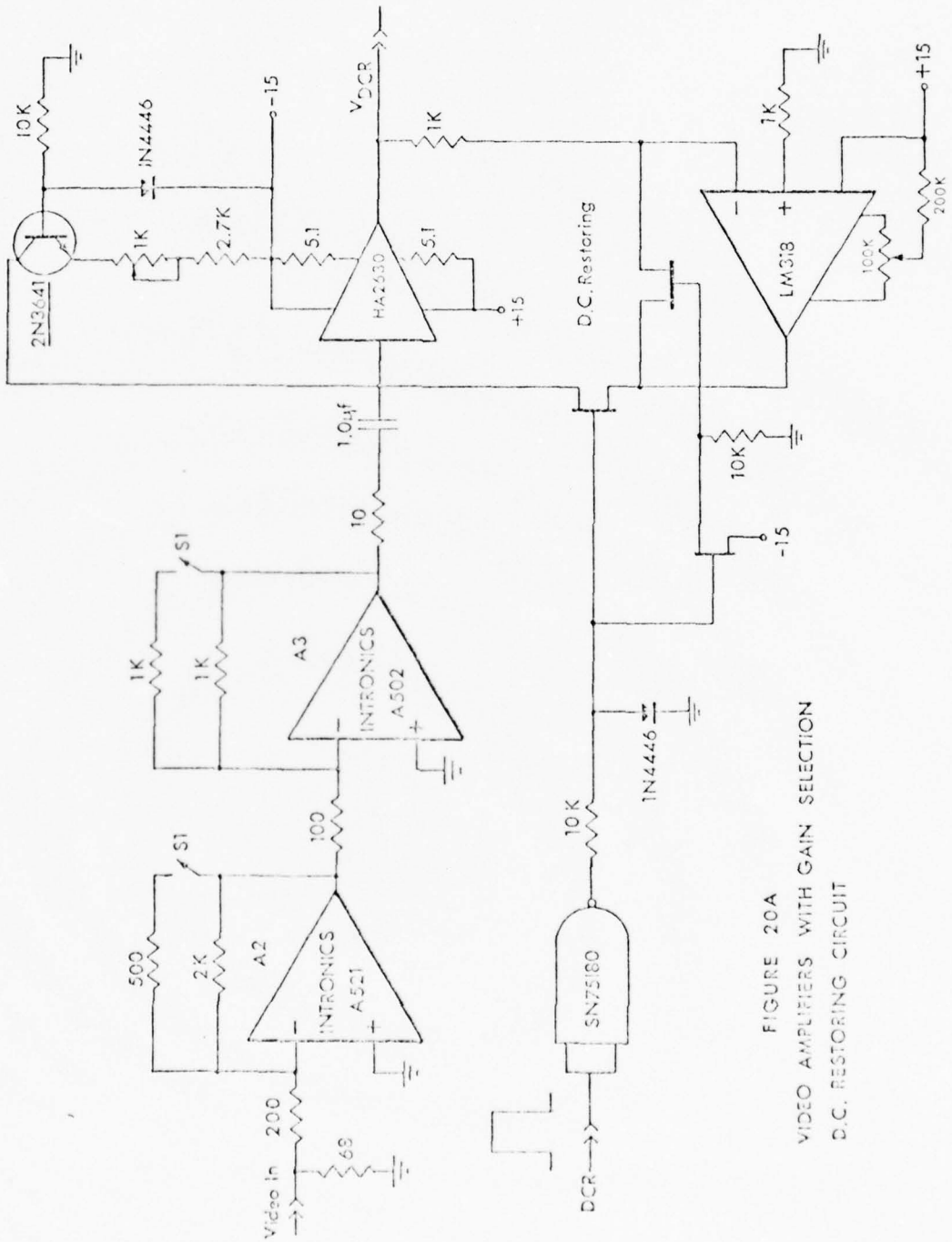


FIGURE 20A

VIDEO AMPLIFIERS WITH GAIN SELECTION

D.C. RESTORING CIRCUIT

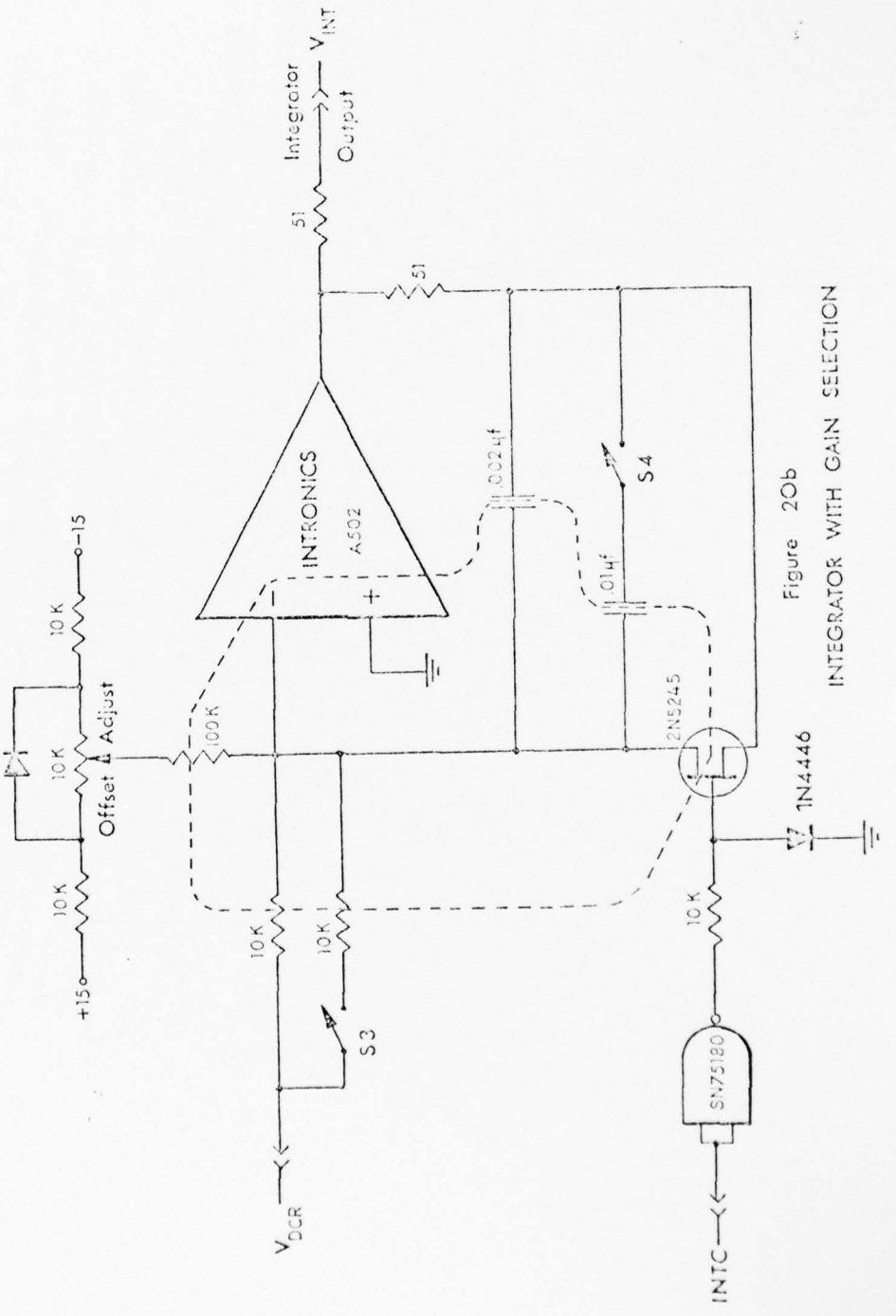


Figure 20b
INTEGRATOR WITH GAIN SELECTION

rotary switch mounted on the front panel, choices being 10, 20, 50, 100. The amplified video signal is then processed by the DC restoring circuit, which provides a considerably higher level of performance than any previous design. Thermal stability is good (dominated by the LM318) and restoring efficiency is more than sufficient (1 mV/V). The DC-restored video (V_{DCR}) drives the two final stages of the chain: the integrator and scope driver circuits. The integrator (Fig. 20b), a modification of the previous circuit, allows gain switching in a 1, 2, 5, 10 sequence. The scope driver represented a more difficult problem: design goals necessitated a 40 V output swing at a slew rate of 2000 V/μsec. The design shown in Fig. 21 turned out to be the least complex circuit capable of withstanding the high voltages while stably producing the necessary slew rates and settling times under realistic operating conditions (100 pf load). It is basically a Class B amplifier using symmetric cascode stages with common collector outputs. Local feedback stabilizes the gain at 4:1. Step response is 20 nsec for a 40 V output swing (settling to 5%).

BEST AVAILABLE COPY

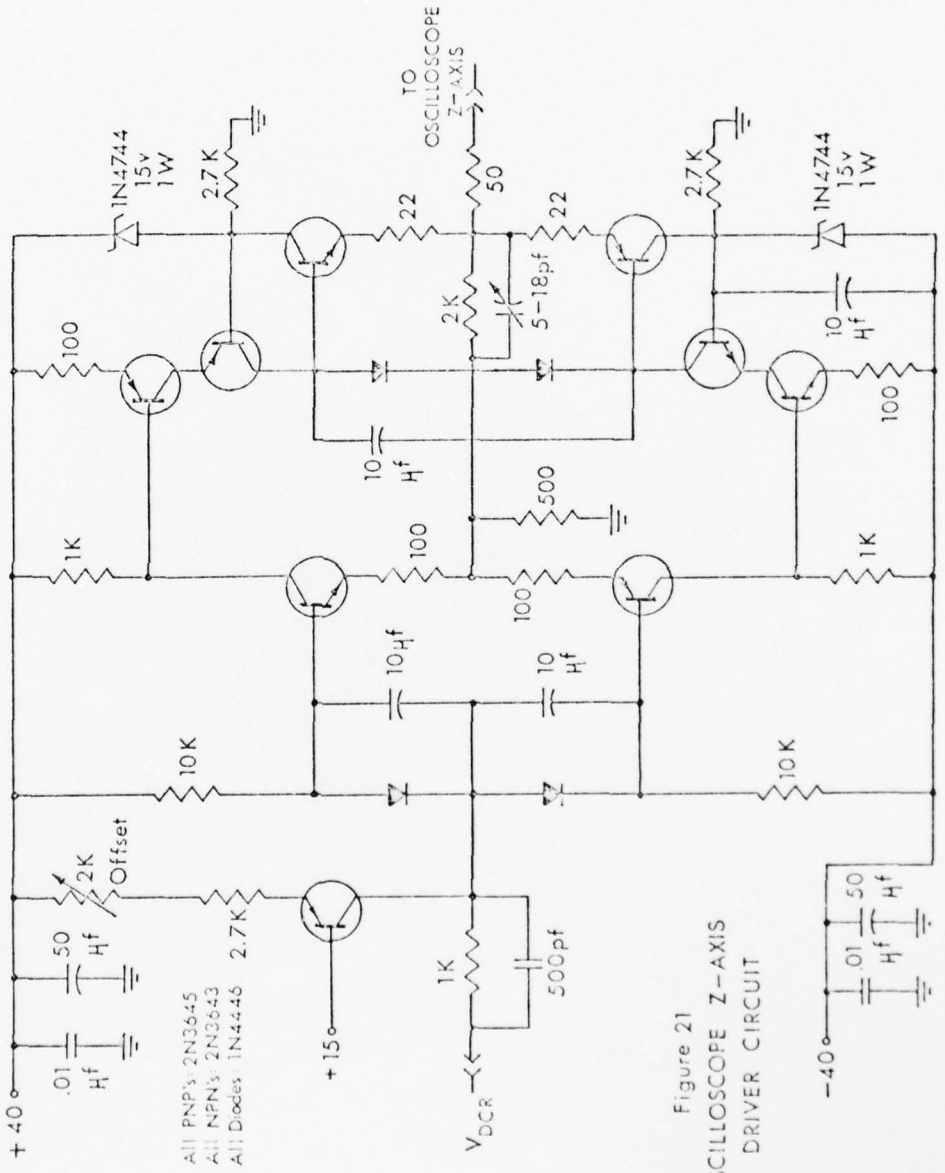


Figure 21
OSCILLOSCOPE Z-AXIS
DRIVER CIRCUIT

4.3 Noise Reduction

The improved bandwidth and sensitivity of the new video circuits provided a greatly enhanced capability for perceiving stray electronic noise. Noise sources included yoke driver feedthrough, TTL digital circuitry spikes, beam gating transients and 60 - 120 Hz hum. Most of the stray signals appeared to be entering the camera enclosure via the (shielded) main power supply and yoke driver cables and then passing through the camera head decoupling networks to the various camera tube electrodes. Apparently the coupling between these electrodes and the Isocon anode is nontrivial, although the exact mechanisms are not clearly understood. The most useful countermeasures were found to be:

1. Double shielding of all cables carrying video signals or camera grid voltages, both internal and external to the camera enclosure.
2. More effective decoupling networks for camera tube electrodes. Decoupling networks housed in shielded enclosures.
3. Completely shielded enclosure for TTL circuitry in the mainframe. Noise suppression circuits for selected TTL output signals.
4. Separate power supplies dedicated to the vertical yoke driver.
5. Ground loop decoupling chokes for selected signal lines.

The net result was approximately a 200-fold decrease in the worst high frequency noise components and a reduction of low frequency components to a very acceptable level. The preamplifier was then

modified to produce the desired performance for the Isocon camera:

Voltage gain	20
Input impedance	12.5 Kohms
Output voltage	1 V (4 μA input).

Frequency response proved to be flat from below 50 kHz to 2 MHz, down 3 dB at 10 MHz, rolling off at 6 dB/octave thereafter. However, once the rest of the video-processing circuitry was connected, a persistent oscillation set in which overloaded most of the amplifiers. In retrospect, this result is not very surprising since the overall voltage gain of the system is nearly 10^4. Feedback paths were isolated and identified, resulting in the decision to build a separate shielded enclosure for the video amplifier and scope driver circuits in the mainframe. This remedy proved very effective, finally allowing proper operation of the video amplifier chain.

4.4 Resolution Enhancement

The newly completed system showed remarkable sensitivity and freedom from artifacts, but resolution was unacceptable (less than 50 TV lines). This was largely due to the increase in sensitivity--i.e., we were beginning to run the system at truly low-light levels and suffering the inevitable loss in resolution which accompanies diminishing faceplate illumination. Even so, this seemed to be an unacceptably low level of performance. The image intensifier was decoupled from the camera so that both devices could be tested separately. The image intensifier tested out at 800 TV-line resolution under (extreme) high-light illumination, whereas the camera would produce no more than 150 TV-line resolution under any conditions.

Clearly the Isocon was at fault. It was then discovered that the Isocon photocathode voltage (which governs image section focus) attained its optimum value at V_{pc} = -600 V, some 150 V less negative than the "typical operating value." Guessing that this was the result of too weak a magnetic field in the image section, the camera tube was remounted, moving it back an additional 0.2" into the yoke. Resolution immediately jumped to 300 TV lines. A series of phone calls to RCA revealed that their initial instructions to us regarding axial position of the camera tube within the yoke had been erroneous. In fact, we were still 0.5" removed from the optimum position. Remachining of the camera mounts allowed a further axial repositioning of 0.2", pushing center resolution into the 800 - 1000 TV-line range. Further axial motion of the camera tube was not possible due to difficulties in coupling to the intensifier.

4.5 Final Parallel-Channel Detector Characteristics

The PCD was reassembled and tested for a variety of performance characteristics. Resolution at the lowest light levels is approximately 200 TV lines. It is interesting that the "standard frame" which has evolved for our I^3Isocon is identical to that used by Savage and Maker (1971) in their Isocon system: 250-line raster and 20 frames per sec. Until very recently, all PCD data were acquired in the integration mode, whereby each vertical scan line is electronically integrated to determine its intensity. This method of data acquisition has worked surprisingly well, even for very weak signals. Under the most favorable operating conditions (stand-alone operation, low ambient electrical noise), we require only a few (2 - 5) photon events/line/frame to maintain a signal-to-noise ratio of unity. For the standard frame, this implies a signal level of about 100 (accepted) photons per sec on a single raster line. This figure is improved by working at reduced frame rates, thereby allowing more time for information to be integrated on the camera target before readout. The Isocon target (at 0°C) will not store data for longer than 500 msec without significant signal degradation. This limits the lowest frame rate to 2 Hz, establishing a lower detection limit of approximately 10 photon events/line/sec. Gain non-uniformity is readily apparent in the integrated data, but this is not a source of particular concern because the non-uniformity can be easily deconvoluted by the computer. It is likely that further cooling of the camera (to -25°C) would extend the maximum integration time to 5 sec, with a corresponding increase in sensitivity.

Unfortunately, it is difficult to obtain this level of performance under real life operating conditions, particularly when the

computer is controlling the camera system. Despite our best efforts, a certain amount of noise from external sources and from the TTL circuits in the Digital I/O Interface appears in the video signal. The noise content of the acquired data can be reduced by time averaging, but overall signal quality is still degraded. In order to improve the low-light level performance of the PCD, circuits were installed for the purpose of photon-event discrimination and counting, a technique which has been very successful for PMT detectors. A bandpass video-level discriminator was designed (Figs. 22 and 23) which would "track" the radial gain profile of the detector head. Due to the nature of event counting, it is not possible to make a post-operative correction for faulty discrimination. For this reason, the discriminator thresholds must be correct at every point in the TV raster if accurate counting is to be achieved. The curve followed by the tracking discriminator is calculated by the C-100 geometry correction module.

Initial tests of the discriminator confirmed its ability to detect photon events, but the resultant SNR was no better than that of the integrator. It was found that noise events were triggering the discriminator, resulting in a "dark noise" of 4 to 5 counts/line/frame. Direct examination of the real-time video signal revealed that a single photon event appears as a (roughly) Gaussian bump in the video, having a half width of 1 to 2 μsec and a peak height at least 2:1 above the RMS noise level. Two major sources of noise were residual 120 Hz hum and occasional sharp spikes (10 to 100 nsec) caused by the local TTL circuitry. Regular transients related to vertical flyback and beam gating were also noticed.

As a result of these observations, the following modifications

BEST AVAILABLE COPY

Figure 22
PHOTON EVENT DETECTOR
DUAL DISCRIMINATOR AND
THRESHOLD MODULATION

REPRODUCED FROM BEST AVAILABLE COPY
COPY AVAILABLE TO DTIC DOES NOT
PERMIT FULLY LEGIBLE REPRODUCTION

BEST AVAILABLE COPY

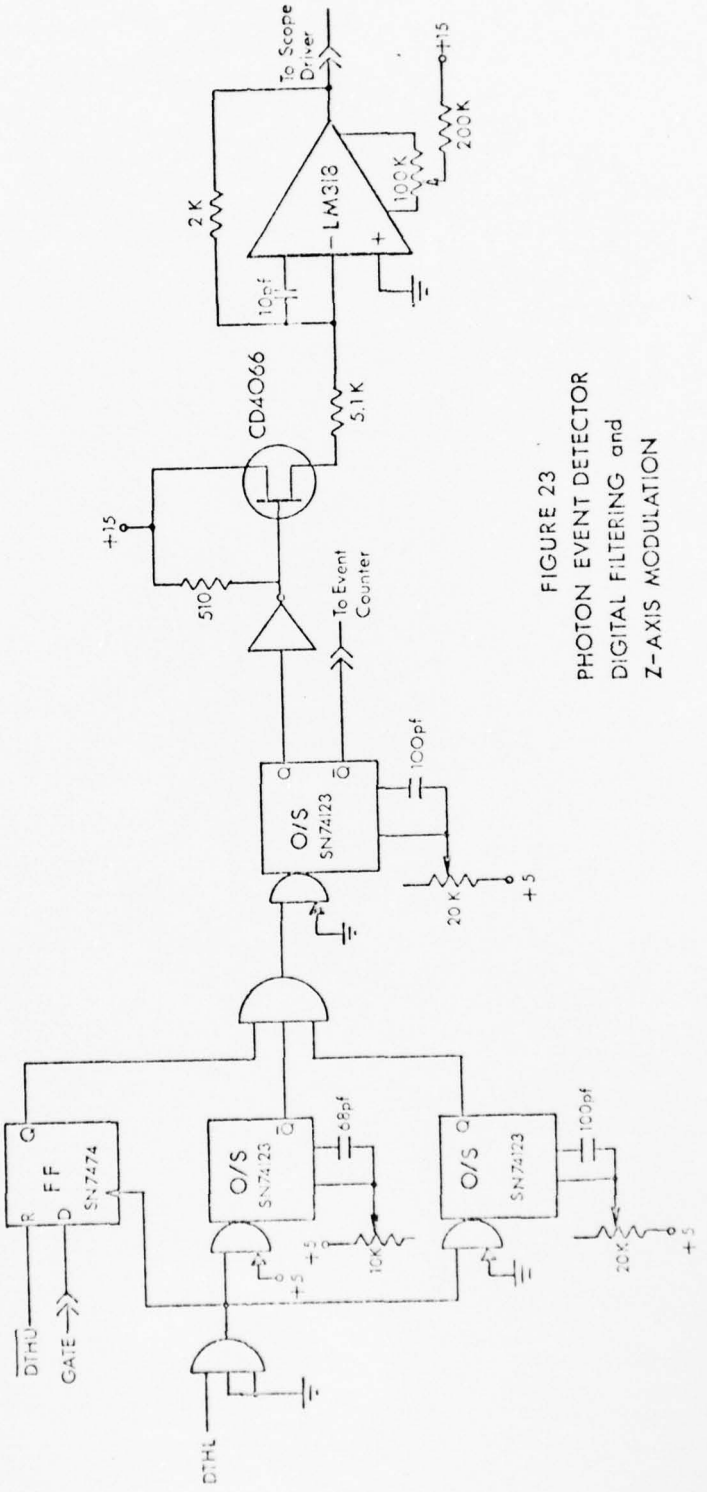


FIGURE 23
PHOTON EVENT DETECTOR
DIGITAL FILTERING and
Z-AXIS MODULATION

were made to the photon counter:

1. Improved gating of the detector, causing it to ignore periodic transients.
2. Bandpass filtering in the analog frequency domain to reject unwanted signals.
3. Digital filtering to suppress all events of less than 500 nsec duration.

As a result, the dark noise count rate dropped to 0.01 counts/line/frame or approximately 50 counts/frame/sec, which is the expected dark noise figure for a cooled 40 mm S-20 photocathode. Counting efficiency for real photon events has not been obviously impaired. Further, the discriminator appears to be totally insensitive to the presence of TTL noise from the computer interface.

Fig. 24 shows a recently acquired spectrum of silicon under essentially the same conditions as for previous tests (Figs. 10 and 19). However, the total input energy for the single-phonon spectra was 0.1 mJ (10^{-5} relative to Fig. 10) and for the two-phonon spectra was 10 mJ (10^{-2} relative to Fig. 19). These energy ratios indicate the relative performance level of the PCD during each stage of the development program--i.e., sensitivity has been improved by a factor of 10^4 overall. Fig. 24 also demonstrates the advantage of using the photon-counting technique. Due to the very low dark noise per detector channel (0.2 counts/sec), PCD performance in each channel should be superior to that of a typical PMT for weak spectra. Dynamic range in the photon-counting mode is not as great as that of a PMT, being limited to peak intensities of about 1000 counts/line/sec, but this range can be extended by a variety of techniques.

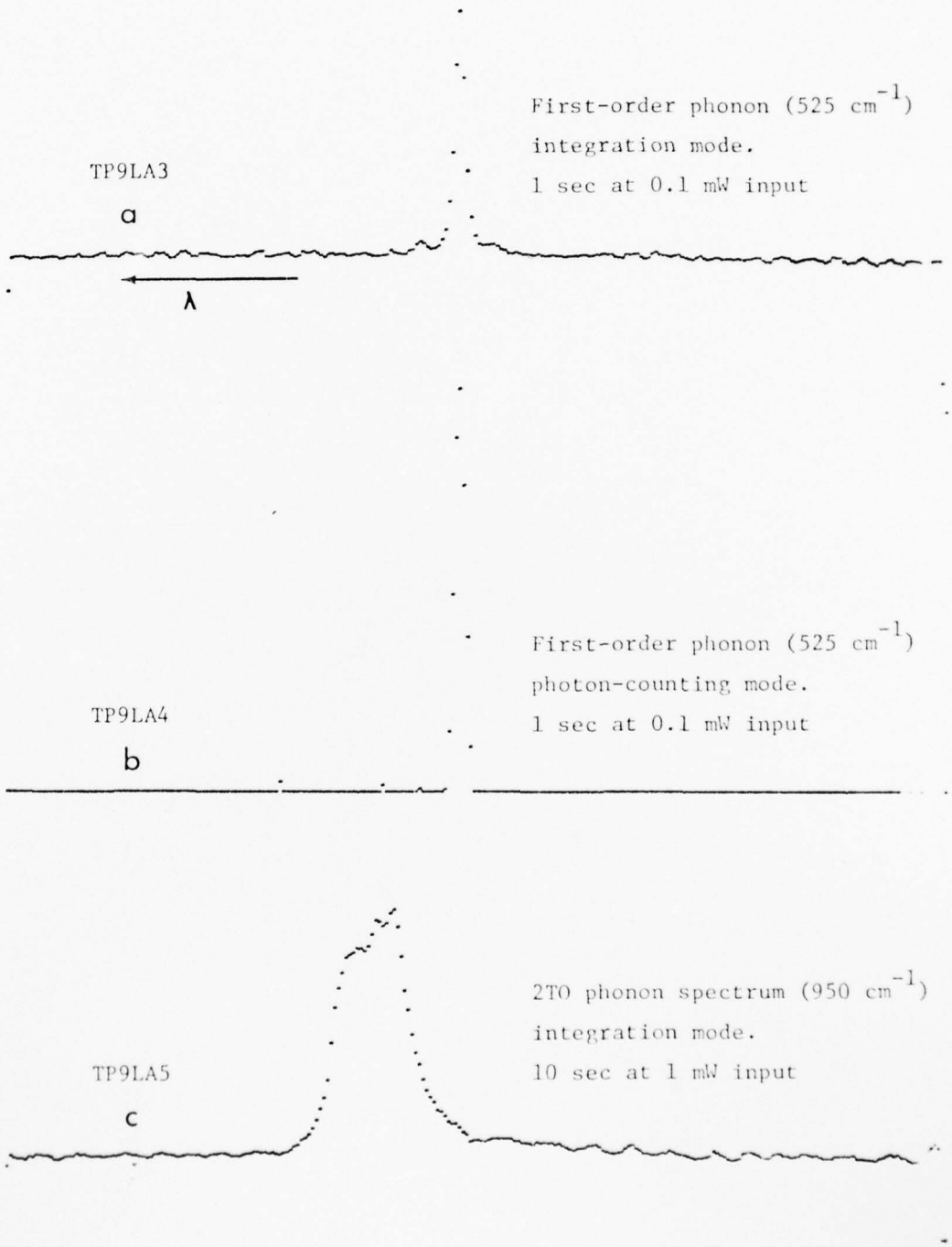


Figure 24

Silicon in reflection geometry, 4880 Å probe.

In conclusion, the design goals have been met. We now have a spectrographic detector optimized for the acquisition of weak signals which achieves at least a 100:1 speed advantage over conventional detectors such as the photomultiplier tube.

4.6 Other Modern Parallel-Channel Detector Systems

The inherent advantages of parallel-channel spectrographic detection have been recognized (and pursued) by a large number of investigators. The earliest work in this field (see Sec. 1.2) provided a much needed source of information regarding the low-light level characteristics of imaging devices and also revealed some of the more subtle pitfalls affecting overall system operation. On the basis of these early results, later groups (ours included) were able to develop substantially improved parallel-channel detectors by integrating the available electro-optic components into systems which were fully engineered for maximum performance.

The most recent advances in this field have resulted from the availability (at reasonable cost) of more advanced imaging devices, such as second generation (GEN-II) intensifiers and "off the shelf" ISIT cameras. Each year the available resources (components, subsystems and engineering design data) have grown, thereby reducing the time and expense of constructing high-speed spectrographic detectors. In addition, it is also possible to purchase parallel-acquisition detectors from a number of manufacturers, including Princeton Applied Research Corp. (OMA), Spex Industries (TOMCA), Electronic Vision Corp. (Digicon), and Tektronix, Inc.

A natural result of the above conditions is that the use of low-light level imaging systems is growing rapidly, especially in those fields where low-light levels have been a chronic problem, i.e., astronomy and Raman scattering. Unfortunately, it is still expensive and time consuming to equip one's laboratory for PCD data acquisition. If we consider only quantum-limited (or nearly quantum-limited)

systems for spectroscopy:

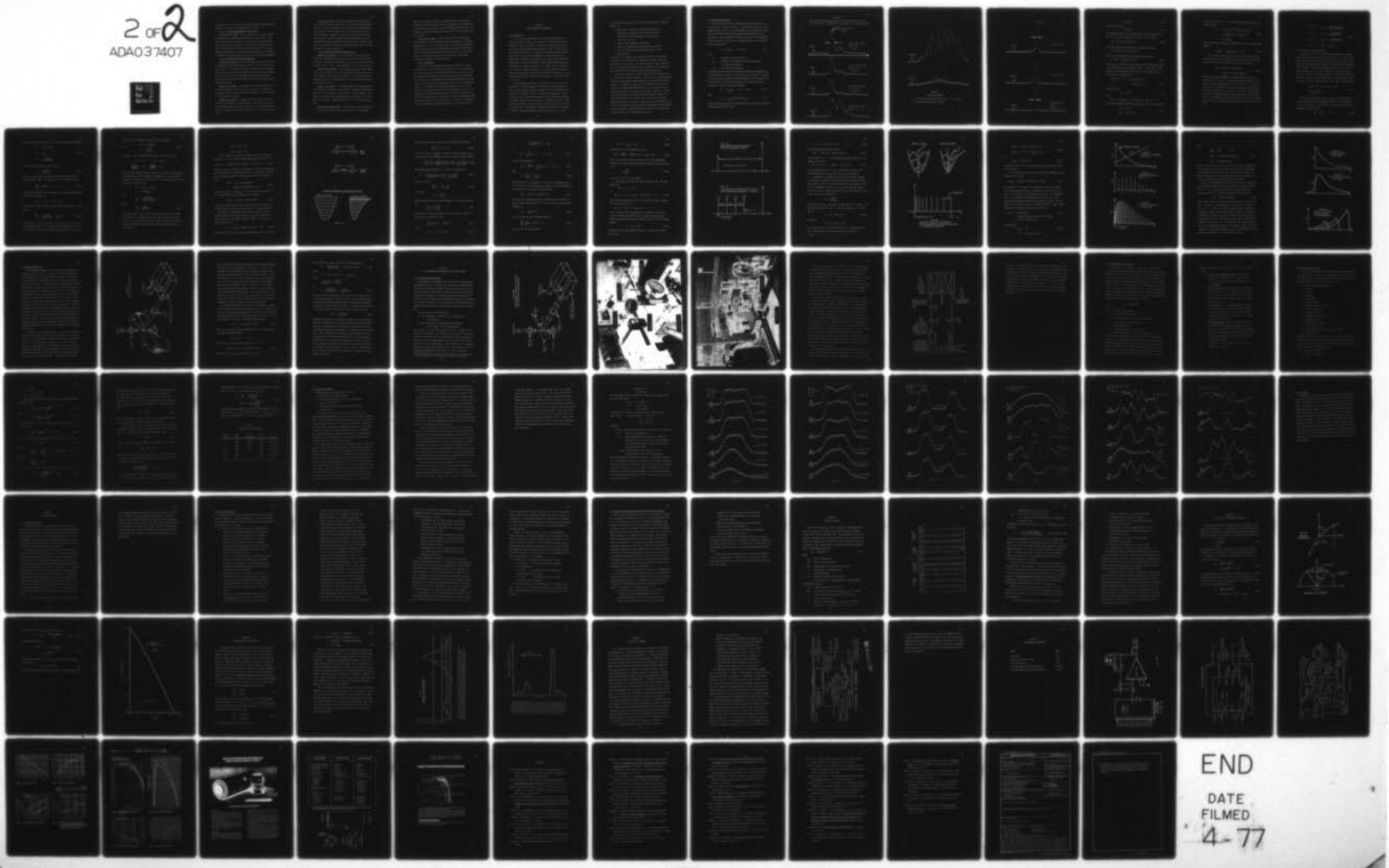
1. The detector alone usually costs more than $20,000 including imaging devices, electronics, cooled housing, etc.
2. Nontrivial modifications of existing equipment are often required. For instance, in Raman scattering experiments it is almost always necessary to equip the spectrograph with holographically ruled gratings, additional dispersion stages or filters in order to reduce stray light levels.
3. Most experimenters have incorporated on-line computers into their PCD systems as an aid in data acquisition, experimental control and data reduction.

As an example of the total cost involved, our PCD represents a time investment of approximately 10 man-years (over a five-year period, due primarily to custom development and testing) and includes capital equipment (detector head, enclosure, dedicated electronics and computer) valued at well over $100,000.

There is an unfortunate consequence of such large commitments of time and money. Once the system is operational, the researcher immediately begins performing one or more scientific investigations, attempting to get some professional benefit from his investment. Often very little time is "wasted" in assessing the exact characteristics and performance limits of the detector. This circumstance, combined with a lack of uniformly accepted evaluation procedures, makes it very difficult to undertake performance comparisons among different low-light level imaging systems. However, it is possible to gain some

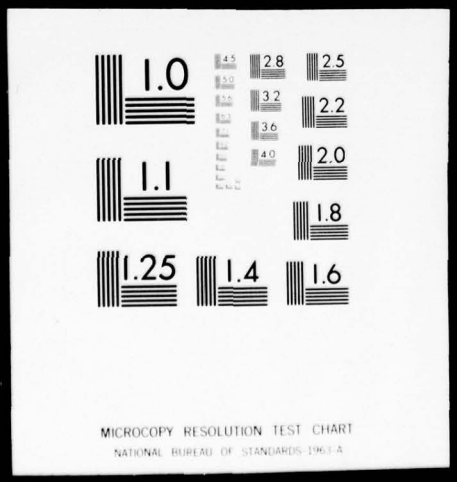
AD-A037 407 YALE UNIV NEW HAVEN CONN DEPT OF ENGINEERING AND AP--ETC F/G 7/4
THE DEVELOPMENT OF A PARALLEL-CHANNEL SPECTROGRAPHIC DETECTOR: --ETC(U)
MAR 77 P C BLACK N00014-76-C-0643
UNCLASSIFIED TR-1 NL

2 OF 2
ADA037407



END
DATE FILMED
4-77

2 OF 2
ADA037407



insight into the current state of the art by summarizing the published results of some recent investigators in this field.

4.6.1 Intensifier/Photographic Plate Method

Willetts et al. (1974). This is probably the most direct method of accomplishing parallel-channel detection of weak spectra. A two-stage intensifier (not cooled) was lens coupled to the photographic plate, providing high resolution (55 lp/mm), low distortion, low reciprocity failure in the film, and reasonable sensitivity. The advantages (and difficulties) of direct electronic readout were eliminated. A holographically ruled grating was used in the one-stage spectrograph.

4.6.2 Low-Sensitivity TV Camera Systems

Busch et al. (1974) used an un-intensified silicon vidicon detector (purchased from Princeton Applied Research Corp.) for flame emission analysis. This detector proved to be considerably less sensitive than a PMT (in each channel) and demonstrated some gain non-uniformity. More sensitive detectors are available from the same manufacturer, using SIT and ISIT cameras, the latter of which should provide quantum-limited performance.

Kuroda et al. (1974): An uncooled two-stage intensifier coupled to an Image Orthicon television camera. The system is optimized for recording (on video disk) ultra-short light pulses. No data were given on resolution or sensitivity.

Gordon et al. (1974): An image converter tube with streak capability, lens coupled to a vidicon camera. Data acquisition was via a 2000-channel transient recorder. The presence of geometric distortion was noted, but no absolute data were given on resolution or sensitivity.

Wood et al. (1975): An uncooled, proximity focused image converter tube, fiber-optic coupled to an SEC camera for flame emission analysis. These investigators used a cross-dispersed (prism-echelle) spectrograph to form the spectrum into a two-dimensional array of spectral elements. Digital X-Y addressing of the camera read-beam position enabled selective readout, although apparently not in the time-dependent manner required by the Selective-Scan Technique. Resolution was approximately 200 lines per raster height, and the entire apparatus was computer controlled.

4.6.3 High-Sensitivity TV Camera Detectors

Sanford et al. (1976): An "off the shelf" ISIT (S-1) used for astronomy. Quantum-limited performance was achieved with 300 TV-line resolution. Integration periods of up to 15 min were possible with the detector cooled to -40°C. Data acquisition was via a video recorder.

French and Long (1975): A four-stage magnetically focused intensifier, lens coupled to an SIT tube, designed for hyper Raman scattering experiments. The detector was gated (25 μsec on time) and fully computer controlled. Single-photon events were detected and counted, using a 256-line raster.

Colgate et al. (1975): A one-stage magnetically focused intensifier, fiber-optic coupled to an SIT camera. Designed for astronomical usage, the cooled detector was controlled by a remote computer. Resolution was 128 lines at 90% modulation depth, operating in slow scan mode (20 μsec/pixel). Signal-to-noise was 1:1 at the single-photon limit.

Stafford and Gilblom (1976): GEN-II image intensifier (essentially a one-stage intensifier tube directly coupled to a microchannel

plate) was fiber-optic coupled to a standard vidicon. Specific performance data were not given, but this system appears to be competitive (in resolution and sensitivity) with an I^3Vidicon or ISIT camera. The developers claim better image quality than the I^3Vidicon and lower cost than the ISIT.

Delhaye et al. (1976). Delhaye and his group have been established leaders in this field for many years and continue to maintain a strong position. Several different camera systems exhibiting quantum-limited sensitivity have been investigated, including an ISIT and an I^4SEC. Emphasis has been placed on the utilization of TV camera detectors for novel applications, such as the detection of picosecond pulses and experiments in Raman microscopy.

4.6.4 Discussion

The purpose of the preceding subsections has been to illustrate the breadth of the PCD field and the diversity of possible approaches to the detector problem. Our primary interest is, of course, in those detectors which are suitable for extremely low-light level operation. The essential goal of quantum-limited detection has been obtained from a variety of instrumental configurations, each with its own particular merits. It is probable that further developmental efforts in this field will be directed toward cost and size reductions as well as improvements in resolution, dynamic range, accuracy of photon counting, response uniformity, and ease of operation. Accurate comparisons based on these parameters will be possible only to the extent that reliable quantitative performance evaluations appear in the open literature.

Chapter 5

FLAME TEMPERATURE MEASUREMENTS

5.1 Introduction

It has been well established in the literature (Hartley et al., 1975) that further insights into the nature of combustion would be of substantial value to the nation. Advances in both diagnostic measurements and combustion modelling are required in order to make significant progress in this area. A variety of perturbing and nonperturbing probes have been used in the examination of combustion processes: thermocouple temperature measurements; laser Doppler velocimetry (LDV) measurements of velocity (Trolinger, 1974); ordinary Raman scattering measurements of temperature (Bandy et al., 1973), density (Lederman et al., 1974) and composition (Arden et al., 1974); coherent anti-Stokes Raman scattering (CARS) measurements of temperature (Moya et al., 1975); Rayleigh scattering and fluorescence measurements of temperature (Vear et al., 1972).

Raman scattering can be used in a variety of ways to measure the temperature of a gaseous sample. Temperature dependent spectral features include rotational scattering structure (shift of band peaks, intensities of individual lines vs. rotational quantum number, contour or envelope fit of band) and vibrational scattering structure (Stokes/anti-Stokes intensity ratio, intensities of individual bands vs. vibrational quantum number, shifts and widths of various bands, full contour or envelope fit). The method of temperature determination by contour fitting the vibrational Raman scattering bands appears to be one of

the most viable techniques for the laboratory environment. Among its virtues are:

1. Specificity: can probe a small volume element, determining the temperature of a particular species.
2. Response relatively independent of gas concentration, flow rates, etc.
3. Yields direct temperature information.
4. Capable of determining non-equilibrium temperatures.
5. Lack of interference from overlapping bands or lines.
6. Nonperturbing.

In contrast to vibrational scattering, methods based on rotational scattering can be complicated by overlapping rotational lines from other species in the sample. The Stokes/anti-Stokes ratio method requires a large spectral coverage (the two peaks are often separated by 3000 cm^{-1} to 6000 cm^{-1}) which can make calibration difficult.

The greatest drawback of Raman scattering for this application is the weakness of the desired spectrum. This can lead to serious problems in cases involving highly luminous flames or operation under daylight conditions. Although the effects of background radiation can be reduced by synchronous detection methods, the time variance of flame luminosity reduces the utility of this approach. Arden et al. (1974) have demonstrated that the random flame scintillation temporal frequency can be driven into resonance by an acoustic wave (600 Hz), thereby improving their ability to reject this unwanted component. The effort in our laboratory has been toward performing ultra-short temperature measurements so that high temporal resolution is obtained while minimizing the effects of background radiation.

5.2 The Scattering Process

Typical Q-branch vibrational-rotational Raman spectra of hot N_2 and O_2 are shown in Figs. 25 and 26. To understand the origin of the shapes and their relation to gas temperature, it is necessary to review the theory of Raman scattering from diatomic gases (Gaufres, 1974). Classically, light scattering is understood in terms of an oscillating dipole induced by the E-field of the exciting radiation. The induced dipole has components

$$M_j = \sum_k \alpha_{jk} E_k \qquad j,k = x,y,z, \tag{5.1}$$

where

E_k k-component of external field

α_{jk} components of polarizability tensor of the molecule, generally symmetric

x,y,z axes fixed in the molecule.

Vibrational Raman scattering is explained in terms of the modulation of the polarizability elements by the vibration of the molecule. The pure rotational scattering results from the modulation of the elements of $\underline{\alpha}$, when expressed in laboratory coordinates, as the molecule rotates. Changing to laboratory coordinates (X,Y,Z):

$$M_\rho = \sum_{jk} \alpha_{\rho\sigma} E_\sigma \qquad (\rho,\sigma = X,Y,Z) \tag{5.2}$$

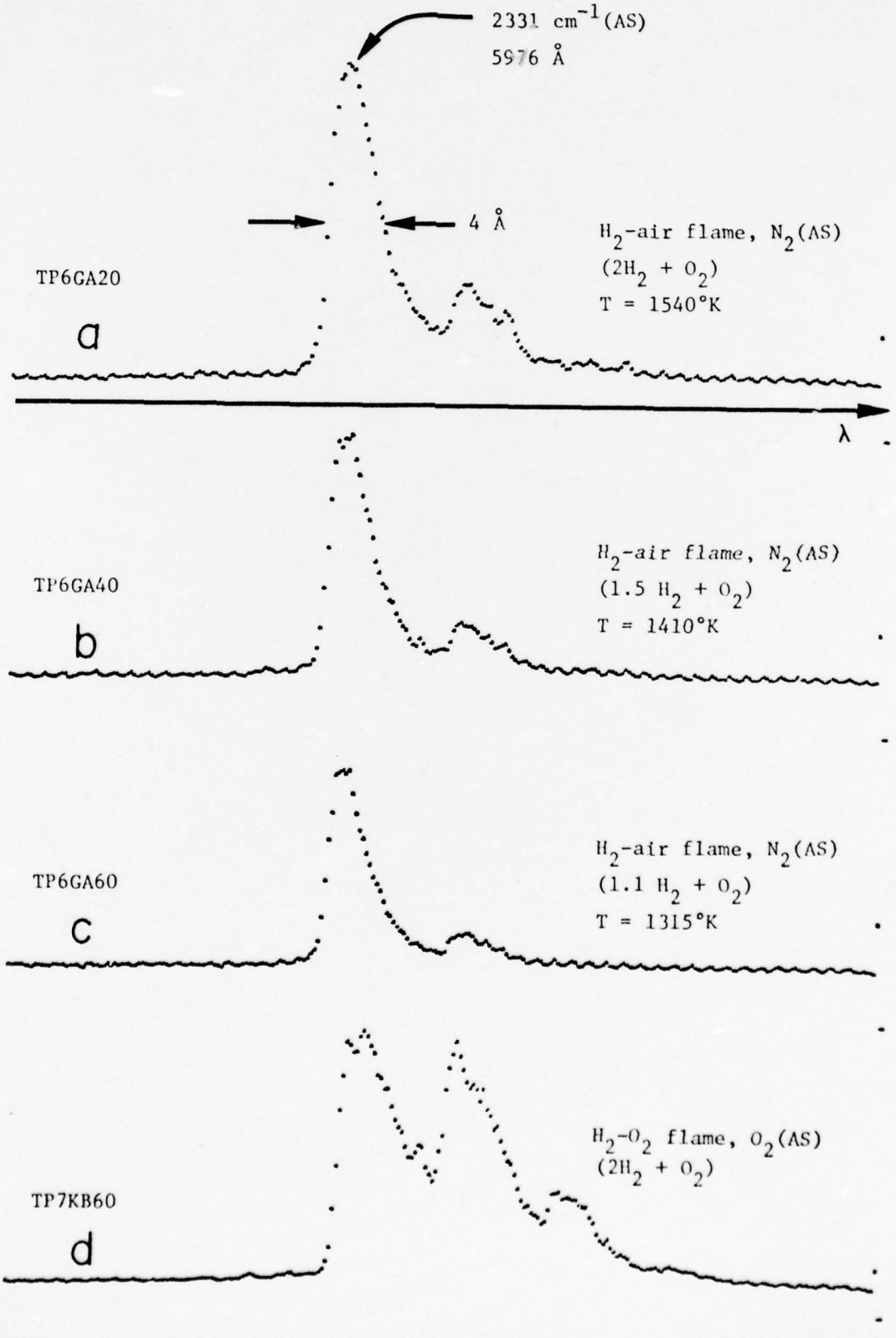
and

$$\alpha_{\rho\sigma} = \sum_{jk} \cos(j,\rho)\cos(k,\sigma)\alpha_{jk}, \tag{5.3}$$

where $\cos(j,\rho)$ and $\cos(k,\sigma)$ are direction cosines. We wish to consider vibrational terms of the form

Figure 25

Vibrational temperature measurements for various burner conditions. Probe is 6943 Å, 15 Joules/pulse, 1 msec duration, 20 pulses/histogram.



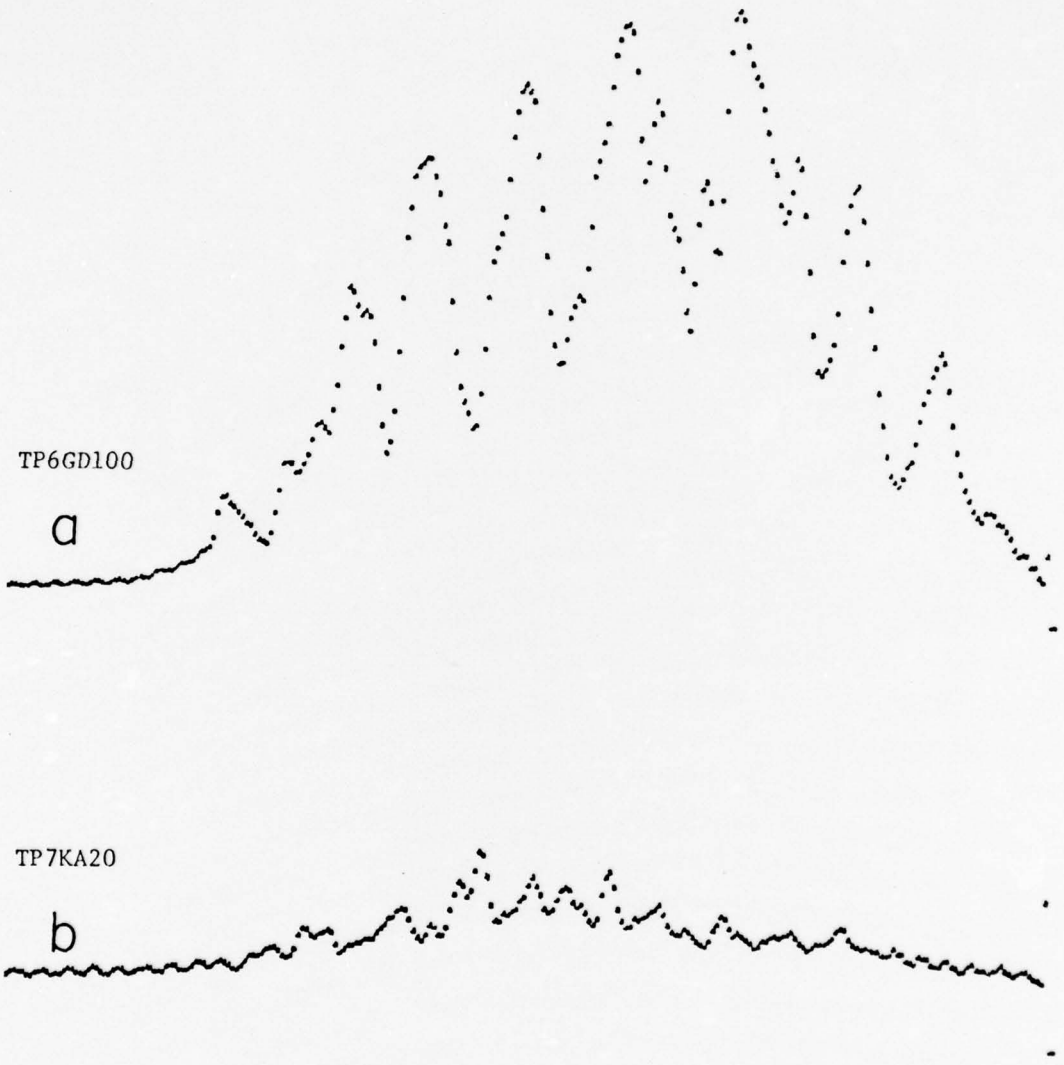


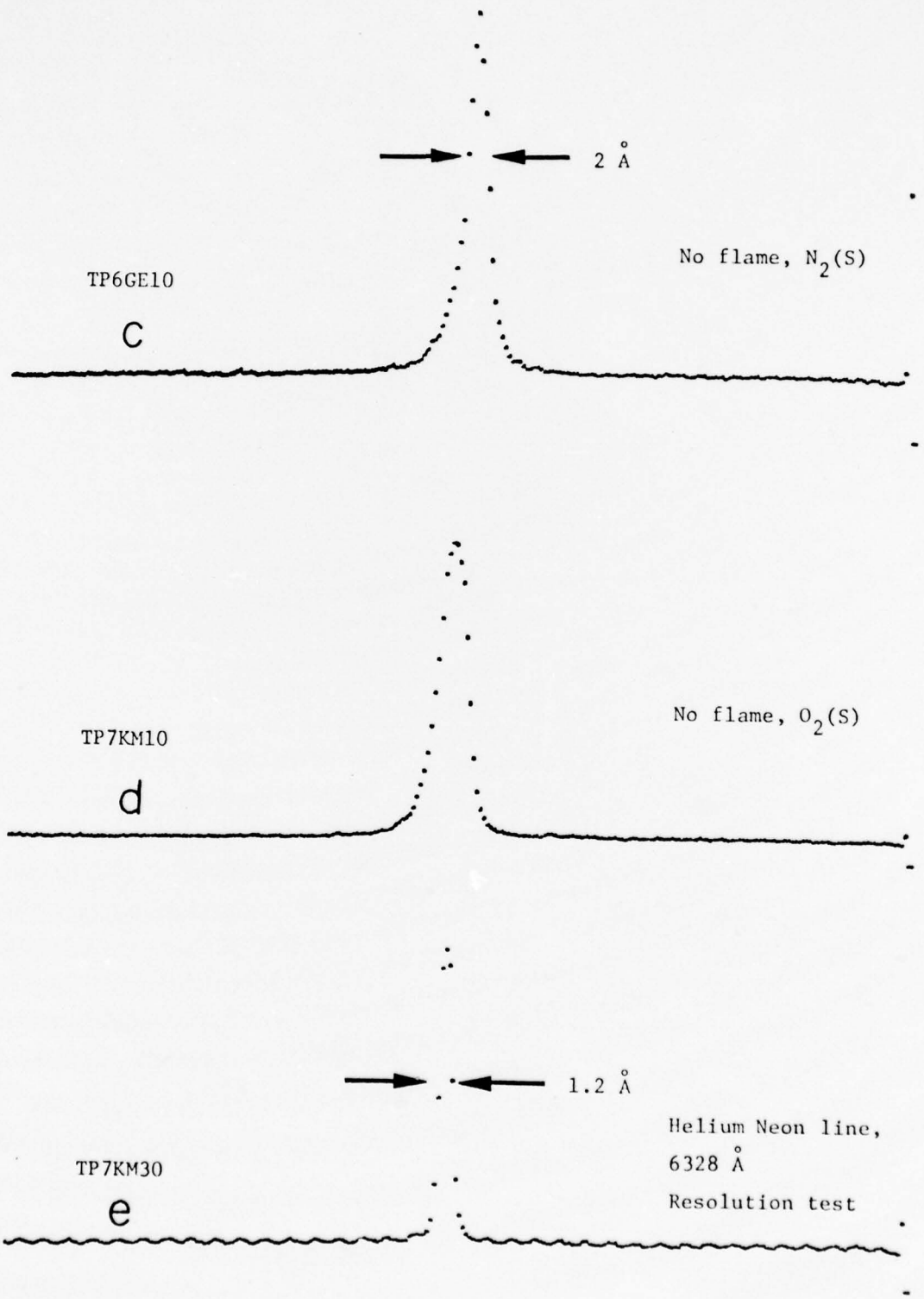
Figure 26

FLAME MEASUREMENTS

a. Flame luminescence near 8283 Å = $N_2(S)$. No probe beam.

b. Luminescence near 5976 Å = $N_2(\Lambda S)$.

Figure 26


2 Å
No flame, N_2(S)
TP6GE10
c
No flame, O_2(S)
TP7KM10
d
1.2 Å
Helium Neon line,
6328 Å
Resolution test
TP7KM30
e

$$\langle V''|\alpha_{jk}|V'\rangle \tag{5.4}$$

and rotational terms

$$\langle J''|\alpha_{\rho\sigma}|J'\rangle \ , \tag{5.5}$$

where quantum numbers of no interest (n,M) have been suppressed in Eq. 5.5. This last expression is, in fact, a sum of terms

$$\sum_{jk} \langle J''|\alpha_{jk} \cos(j,\rho)\cos(k,\sigma)|J'\rangle. \tag{5.6}$$

For a vibrational-rotational jump, we find matrix elements

$$\langle V'',J''|\alpha_{jk} \cos(j,\rho)\cos(k,\sigma)|V',J'\rangle,$$

which can be separated to give a product representation

$$\langle V''|\alpha_{jk}|V'\rangle \langle J''|\Phi_{\rho\sigma jk}(\theta,\phi,\chi)|J'\rangle \tag{5.7}$$

where $\Phi_{\rho\sigma jk}$ is a function of the Eulerian angles defining the orientation of the molecule in the laboratory axes. ρ and σ refer to the directions of polarization of the scattered and exciting light. For fixed ρ and σ, the intensity is

$$I_{\rho\sigma}(V'',J'' \to V',J') \propto \sum_{jk} |\langle V''|\alpha_{jk}|V'\rangle|^2 \cdot |\langle J''|\Phi_{\rho\sigma jk}|J'\rangle|^2. \tag{5.8}$$

Suppose we write

$$\underline{\underline{\alpha}} = \underline{\underline{\alpha}}^o + \underline{\underline{\alpha}}^1 \tag{5.9}$$

where

$$\alpha^o_{ij} = 1/3\ \mathrm{Tr}(\underline{\underline{\alpha}})\delta_{ij} = 1/3\ (\alpha_{xx} + \alpha_{yy} + \alpha_{zz})\delta_{ij} = \alpha,$$

so that $\underline{\underline{\alpha}}^o$ is diagonal and has the same trace as $\underline{\underline{\alpha}}$. This fixes $\underline{\underline{\alpha}}^1$ as

$$\begin{aligned} \alpha^1_{jj} &= \alpha_{jj} - \alpha \\ \alpha^1_{ij} &= \alpha_{ij} \ (j \neq k) \end{aligned} \tag{5.10}$$

so that $\underline{\underline{\alpha}}^1$ has zero trace. If we decompose the matrix elements in a similar fashion,

$$\begin{aligned} I_{\rho\sigma} &\propto |\langle V''|\alpha\delta_{jk}|V'\rangle|^2 \, |\langle J''|\Phi^0_{\rho\sigma jk}\delta_{jk}|J'\rangle|^2 \\ &+ |\langle V''|\alpha^1_{jk}|V'\rangle|^2 \, |\langle J''|\Phi^1_{\rho\sigma jk}|J'\rangle|^2 \\ &= I_{TR} + I_{ANIS}, \end{aligned} \tag{5.11}$$

called the trace and anisotropy contributions. Since α is spherically symmetric,

$$\Phi^0_{\rho\sigma jk}\delta_{jk} = \Phi^0_{\rho\sigma jk}\delta_{\rho\sigma}\delta_{jk} = \delta_{\rho\sigma}\delta_{jk}. \tag{5.12}$$

It can be shown that the overall shape of the vibrational-rotational Raman spectrum is dominated by I_{TR} for the cases of interest. The effect of rotational structure within a band is given by:

$$\begin{aligned} I_{\rho\sigma} &= C_{TR}(2J + 1) \exp(-E_{ROT}/kT) \\ &+ C_{AN}(2J + 1)S(J) \exp(-E_{ROT}/kT), \end{aligned} \tag{5.13}$$

where C_{TR} and C_{AN} are constants. In general, Raman scattering is allowed for $\Delta J = 0, \pm 1, \pm 2$ so we expect five different bands. These bands are commonly designated O, P, Q, R, S for $\Delta J = -2, -1, 0, +1, +2$, respectively. As a result of Eq. 5.12, trace scattering contributes only to the Q-branch ($\Delta J = 0$), whereas it is possible for anisotropy scattering to contribute to any of the five branches. The term S(J) in Eq. 5.13 determines the relative intensity of anisotropy scattering for each branch. According to Placzek and Teller (1933), these terms are:

$$\begin{aligned}
\Delta J &= +2 \qquad S_S(J) = \frac{3(J+1)(J+2)}{2(2J+1)(2J+3)} \\
\Delta J &= -2 \qquad S_O(J) = \frac{3(J-1)J}{2(2J-1)(2J+1)} \\
\Delta J &= 0 \qquad S_Q(J) = \frac{J(J+1)}{(2J-1)(2J+3)} \\
\Delta J &= \pm 1 \qquad S_P(J) = S_R(J) = 0
\end{aligned} \tag{5.14}$$

for a homonuclear diatomic molecule.

Absence of the $\Delta J = \pm 1$ branches can be understood by considering the rotation of the polarizability ellipsoid. For rotations perpendicular to the principal molecular axis, the polarizability ellipsoid of a homonuclear diatomic molecule is unchanged after undergoing a 180° rotation. Thus, the polarizability varies at twice the rotational frequency ($\Delta J = 2$) and the fundamental rotational frequency ($\Delta J = 1$) is absent from the Raman spectrum. The division of scattered intensity among the allowed branches can be estimated from the limiting values of S(J) as J becomes large. These values for large J are:

$$\begin{aligned}
&S_S(J) \to 3/8 \qquad S_O(J) \to 3/8 \qquad S_Q(J) \to 1/4 \\
&\text{and} \sum_{O,Q,S} S(J) = 1
\end{aligned} \tag{5.15}$$

The relative strengths of I_{TR} and I_{AN} can be deduced from the available data concerning depolarization ratios. The depolarization factor ρ is defined to be the ratio of the minimum scattered power to the maximum scattered power:

$$\rho = \frac{I_{\perp}}{I_{\parallel}} = \frac{I_{\rho\sigma}}{I_{\rho\rho}} \qquad \rho \neq \sigma, \tag{5.16}$$

which can be expressed in terms of the trace and anisotropy components:

$$I_{\parallel} \propto 45I_{TR} + 4I_{AN}$$

$$I_{\perp} \propto 3I_{AN} \tag{5.17}$$

$$\rho = \frac{3I_{AN}}{45I_{TR} + 4I_{AN}} .$$

In a notation more familiar to some readers,

$$\rho = \frac{3\gamma^2}{45a^2 + 4\gamma^2} , \tag{5.18}$$

where a,γ are the mean value and anisotropy of the polarizability tensor $\underline{\alpha}$ (Weber, 1973). This equation can be rearranged to yield:

$$\frac{I_{TR}}{I_{AN}} = \frac{3 - 4\rho}{45\rho} = R. \tag{5.19}$$

If the Raman scattered light is collected in a polarization independent manner, the total signal is

$$I_T = I_{\parallel} + I_{\perp} = 45I_{TR} + 7I_{AN}.$$

The fraction of collected signal contributed by the anisotropic scattering is:

$$\frac{I_{AN}}{I_T} = \frac{7I_{AN}}{45I_{TR} + 7I_{AN}} = \frac{7}{45R + 7} . \tag{5.20}$$

A recent value of the depolarization ratio for N_2 reported by Bridge and Buckingham (1966) is $\rho = 1.018\%$ for 6328 Å illumination. A value given by Weber et al. (1967) for 6943 Å illumination is ρ^Q (Q-branch

only) = 0.59%. Estimating ρ from ρ^Q via the relationship

$$\rho^Q = 1/4\left(\frac{\rho}{1-\rho}\right)$$

or:

$$\rho = \frac{4\rho^Q}{1+4\rho^Q}, \tag{5.21}$$

we find $\rho = 2.3\%$. Using these values ($\rho_B = 1.018\%$, $\rho_w = 2.3\%$),

$$R_B = 6.46\% \qquad R_w = 2.81\%$$

$$\left(\frac{I_{AN}}{I_T}\right)_B = 2.4\% \qquad \left(\frac{I_{AN}}{I_T}\right)_w = 5.2\%.$$

Thus the trace scattering alone accounts for at least 95% of the Raman signal from N_2 in this experimental configuration. It is possible to estimate the intensity of either the O- or the S-branch relative to the Q-branch by using Eq. 5.15.

$$I_Q \simeq 45I_{TR} + 7(1/4)I_{AN}$$

$$I_O \simeq 7(3/8)I_{AN}$$

and

$$\frac{I_O}{I_Q} = \frac{(21/8)I_{AN}}{45I_{TR} + (7/4)I_{AN}} .$$

Thus:

$$\frac{I_O}{I_Q} = \frac{21}{360R + 14}, \tag{5.22}$$

which yields $0.9\% < I_O/I_Q < 2.0\%$. For this reason, it is not likely to detect the O- or S-branches under the current experimental conditions. It is, of course, possible to enhance the relative contribution of trace scattering to the total Raman signal by detecting only $I_{\parallel}$. For this case,

$$1.4\% < I_{AN}/I_T < 3.1\%$$

$$0.5\% < I_O/I_Q < 1.2\%.$$

In the following discussion, we consider only trace scattering (Q-branch, $\Delta J = 0$) for a single vibrational-rotational band ($\Delta V = 1$).

$$I_{TR} \propto (\nu_o - \nu_{RAM})^4 N(J) \sum |\langle V''|\alpha^o_{jj}|V'\rangle|^2 \langle J|\Phi^o_{\rho\rho jj}|J\rangle|^2, \qquad (5.23)$$

where $(\nu_o - \nu_{RAM})$ is the absolute frequency of the Raman line (approximately constant over a narrow band) and N(J) is the number of molecules in the initial state $\langle V''J|$. We know that within the V'' vibrational state

$$\begin{aligned} N(J) &\propto (2J + 1) \exp(-E_{ROT}/kT) \\ &= (\text{degeneracy})(\text{population factor}). \end{aligned} \qquad (5.24)$$

Further, since $\alpha^o_{jj} = \alpha$ and $\Phi^o_{\rho\rho jj} = 1$, we can remove the summation in Eq. 5.23 and lump the matrix elements into a constant:

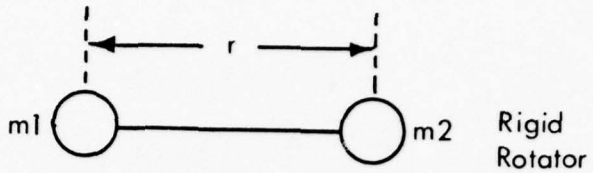
$$I_{TR}(J) \propto C_{TR}(2J + 1) \exp(-E_{ROT}/kT). \qquad (5.25)$$

In order to find the shape of the Q-band, we must now determine the allowed vibrational-rotational energy states of a diatomic molecule.

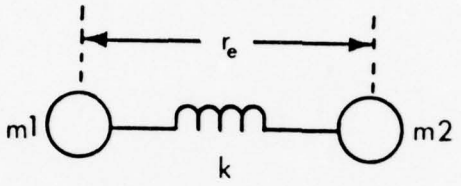
The simplest approximation for rotational energies is that of a rigid rotator (see Fig. 27) consisting of two masses connected by a rigid, massless bar of length r (Herzberg, 1950). We know that the moment of inertia is:

$$I = \sum m_i r_i^2 = (m_1 m_2 r^2)/(m_1 + m_2) = \mu r^2. \qquad (5.26)$$

If we represent this as a single particle of reduced mass μ at a fixed



Rigid Rotator



Nonrigid Rotator

POTENTIAL ENERGIES AND VIBRATIONAL LEVELS

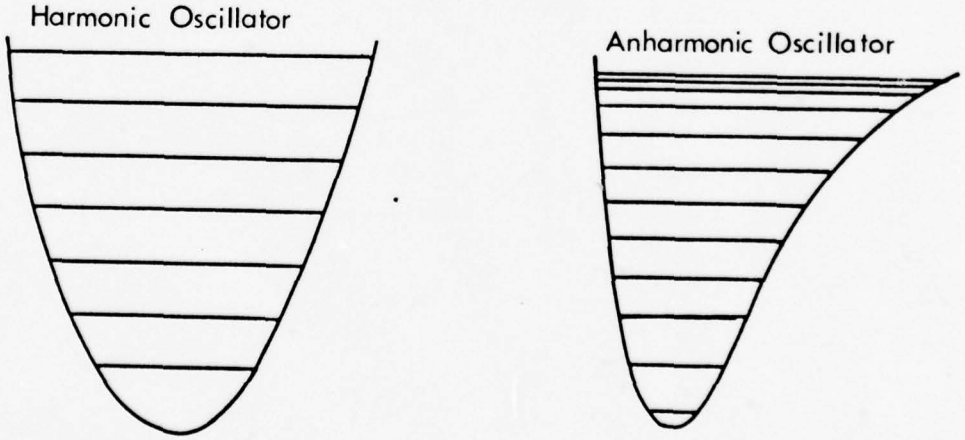


Figure 27

radius r from the origin, we can solve the Schroedinger equation

$$\frac{-\hbar^2}{2\mu} \nabla^2 \psi + V\psi = E\psi \tag{5.27}$$

with $V(r) = 0$ and r = constant. The kinetic energy operator can be written in spherical coordinates (r,θ,ϕ) as (Dicke and Wittke, 1960):

$$\nabla^2 = \left(\frac{1}{r}\frac{\partial}{\partial r} r\right)^2 + \frac{1}{r^2}\left[\frac{1}{\sin\theta}\frac{\partial}{\partial\theta}\left(\sin\theta\frac{\partial}{\partial\theta}\right) + \frac{1}{\sin^2\theta}\frac{\partial^2}{\partial\theta^2}\right]. \tag{5.28}$$

The angular momentum operator L^2 in the same coordinates is:

$$L^2 = -\hbar^2\left[\frac{1}{\sin\theta}\frac{\partial}{\partial\theta}\left(\sin\theta\frac{\partial}{\partial\theta}\right) + \frac{1}{\sin^2\theta}\frac{\partial^2}{\partial\theta^2}\right]. \tag{5.29}$$

Thus we can write:

$$\frac{-\hbar^2}{2\mu}\nabla^2 = \frac{P_r^2}{2\mu} + \frac{L^2}{2\mu r^2} \tag{5.30}$$

by defining

$$P_r = -i\hbar\frac{1}{r}\frac{\partial}{\partial r} r,$$

thereby separating out the radial dependence. Now the wave equation is:

$$\left[\frac{1}{2\mu}P_r^2 + \frac{L^2}{2\mu r^2}\right]\Psi = E\Psi. \tag{5.31}$$

We know that ψ is not a function of r, so we can let $\psi = Y_{Jm}(\theta,\phi)$ without loss of generality. Thus,

$$\frac{L^2}{2r^2\mu} Y_{Jm}(\theta,\phi) = EY_{Jm}(\theta,\phi). \tag{5.32}$$

Since

$$L^2 Y_{Jm} = \hbar^2 J(J+1)Y_{Jm}, \tag{5.33}$$

$$\frac{\hbar^2 J(J+1)}{2\mu r^2} Y_{Jm} = EY_{Jm}$$

or

$$E(J) = \frac{h^2}{8\pi^2 I} J(J+1) \qquad J = 0,1,2... \tag{5.34}$$

In terms of wave numbers,

$$F(J) = \frac{E(J)}{hc} = \frac{h}{8\pi^2 cI} J(J+1) = BJ(J+1) \tag{5.35}$$

where

$$B = \frac{h}{8\pi^2 cI} = \frac{h}{8\pi^2 c\mu r^2} . \tag{5.36}$$

We can extend the above argument to the case of a nonrigid rotator, i.e., one where r increases slightly at higher rotational frequencies. This results in a second-order correction term:

$$F(J) = BJ(J+1) - DJ^2(J+1)^2. \tag{5.37}$$

If we treat our nonrigid rotator as a simple harmonic oscillator so that the radial restoring force is F = -kr, the classical vibrational frequency is:

$$\nu_{osc} = \frac{1}{2\pi}(k/\mu)^{1/2}. \tag{5.38}$$

For the quantum case, the defining equation is:

$$\frac{d^2\psi}{dr^2} + \frac{2\mu}{\hbar^2}(E - kr^2/2)\psi = 0, \tag{5.39}$$

which has the well known energies

$$E(V) = h\nu_{osc}(V + 1/2). \tag{5.40}$$

The term values of the oscillator are thus:

$$G(V) = \frac{E(V)}{hc} = \frac{\nu_{osc}}{c}(V + 1/2) = \omega_e(V + 1/2), \tag{5.41}$$

where ω_e is the vibrational frequency in cm^{-1}. For the harmonic oscillator case, the second-order factor D from Eq. 5.37 can be shown to be:

$$D = \frac{4B^3}{(\nu_{osc})^2}. \tag{5.42}$$

Since $\nu_{osc} >> B$, $D << B$, as expected.

At this point, one might ask how the spectrum looks. The term values are:

$$G(V) = \omega_e(V + 1/2),$$

so

$$G(V \rightarrow V + 1) = \omega_e(V + 1/2) - \omega_e(V + 3/2) = -\omega_e \tag{5.43}$$

and all Stokes transitions for $\Delta V = 1$ have the same shift. Further, for the Q-branch ($\Delta J = 0$),

$$F(J \rightarrow J) = BJ(J + 1) - BJ(J + 1) = 0,$$

so the spectrum in this approximation is a singlet with a shift ω_e from the exciting line (see Fig. 28). However, we know that the potential energy function for the diatomic molecule is not the simple parabola

$$U = f(r - r_e)^2. \tag{5.44}$$

We can refine the approximation by adding in a higher order (anharmonic) term:

Figure 28

LINE POSITIONS FOR SIMPLE HARMONIC OSCILLATOR, NONRIGID ROTATOR

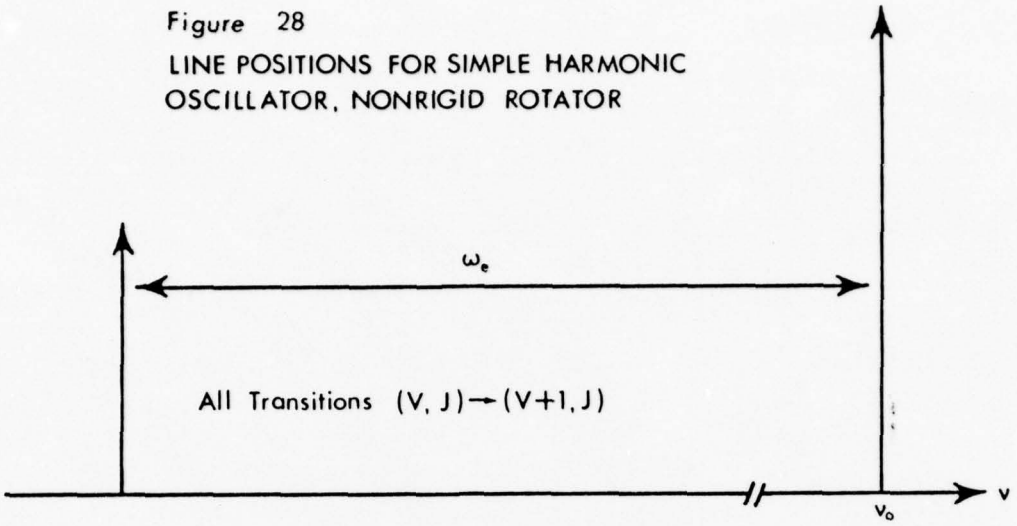
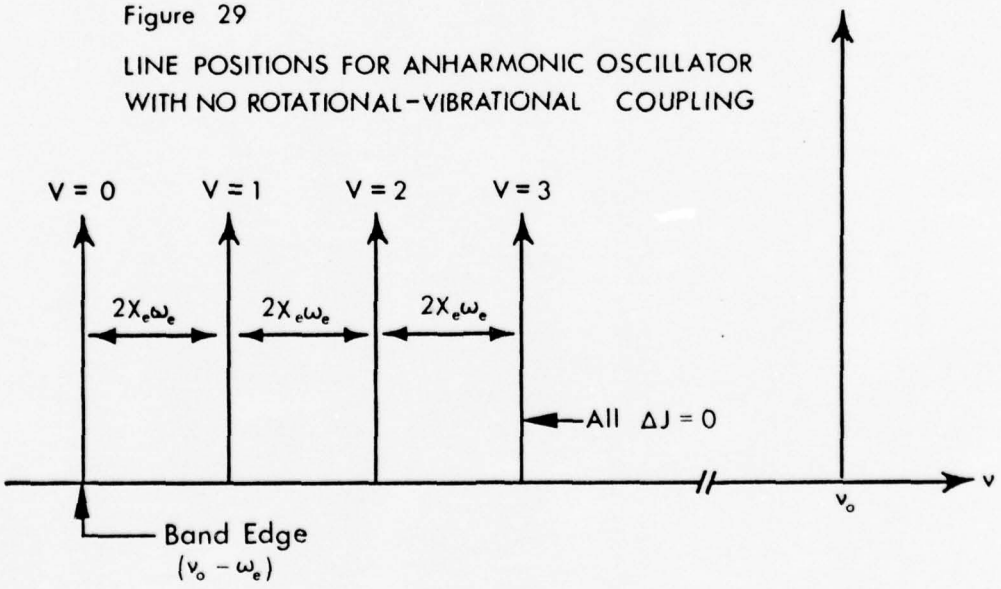


Figure 29

LINE POSITIONS FOR ANHARMONIC OSCILLATOR WITH NO ROTATIONAL-VIBRATIONAL COUPLING



$$U = f(r - r_e)^2 - g(r - r_e)^3 + \ldots \quad f >> g. \tag{5.45}$$

The modified energy term values become:

$$G(V) = \omega_e(V + 1/2) - \omega_e x_e(V + 1/2) + \ldots \tag{5.46}$$

where in general $x_e << 1$. Thus the spacing decreases slowly as V increases. Now we find:

$$G(V \to V + 1) = \omega_e - 2\omega_e x_e V = \omega_e(1 - 2x_e V), \tag{5.47}$$

so that each transition $\Delta V = 1$ has a unique shift, adjacent lines being separated by $\Delta\nu = 2\omega_e x_e$ (see Fig. 29, preceding page).

To understand the finite width of each band (shown as singlets in the figure), we consider the interaction of vibrational and rotational modes. Clearly $r \neq r_e$ during vibration, so we expect $B \propto 1/r^2$ to vary accordingly. Since $\nu_{osc} >> \nu_{ROT}$, we can take the average value of r (in some vibrational state) for our B calculation. The old B we now call B_e (equilibrium), so

$$B_e = \frac{h}{8\pi^2 c\mu r_e^2}.$$

Referring to Fig. 30, we see that $\bar{r}$ (average value of r) equals r_e for the harmonic oscillator, but $\bar{r} > r_e$ for the anharmonic case. The result is:

$$B_V = B_e - \alpha_e(V + 1/2). \tag{5.48}$$

Analogously,

$$D_V = D_e + B_e(V + 1/2),$$

but the latter term is so small an effect as to be neglected in our case. Now consider the full term equation for a single $\Delta V = 1$ transition

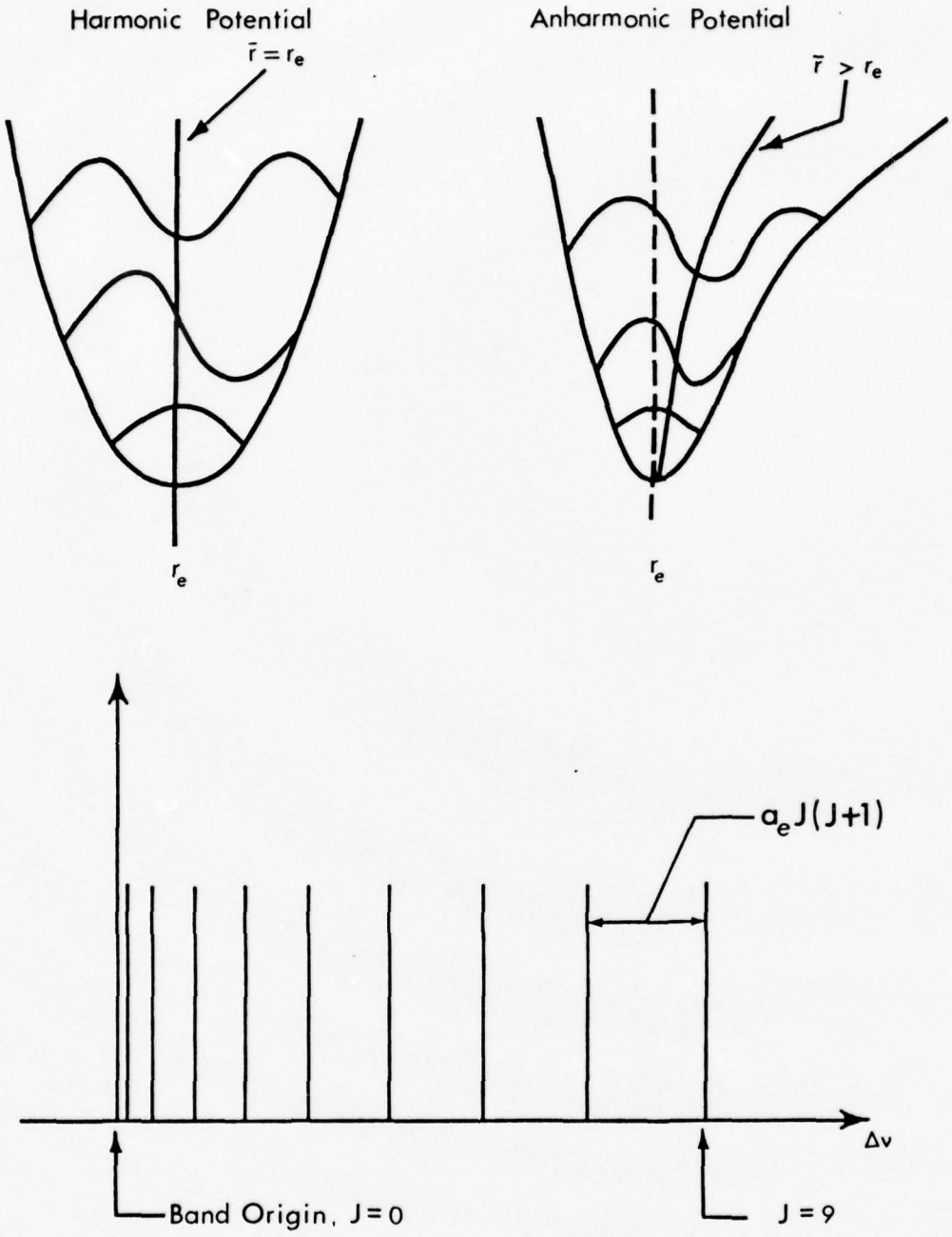


Figure 30
LINE POSITIONS WITHIN A SINGLE BAND.
EFFECTS OF VIBRATIONAL-ROTATIONAL COUPLING
IN ANHARMONIC OSCILLATOR.

$$F(V,J) = B_V J(J+1) - DJ^2(J+1)^2$$

$$F(V, J \to V+1, J) = (B_{V+1} - B_V)\, J(J+1) \tag{5.49}$$

or

$$\Delta\nu_{ROT} = -\alpha_e J(J+1), \tag{5.50}$$

so that for a ($\Delta V = 1$, $\Delta J = 0$) series, the different J terms are distinct (Fig. 30).

It is now possible to calculate the intensities throughout a band. From Eqs. 5.25 and 5.35,

$$I_{TR}(J) \propto C_{TR}(2J+1) \exp(-Bhc\, J(J+1)/kT) \tag{5.51}$$

for a single $V \to V+1$ band. The two terms of Eq. 5.51 are shown in Fig. 31, then summed in Fig. 32. Note, however, that this is in "J-space." We transform to $\Delta\nu$ coordinates by using Eq. 5.50, remembering that $\Delta\nu$ is the distance from the band edge (see Fig. 33). If the spectrum were completely resolved, this would be its shape. This is rarely the case because the $\Delta\nu$ are so small ($\simeq 10^{-3}$ B). Given a finite bandpass, we calculate the intensity per unit $\Delta\nu$ as:

$$I(\Delta\nu) = I(J)\left|dJ/d(\Delta\nu)\right| \tag{5.52}$$

= (average intensity of lines in this region)

· (number of lines in $\Delta\nu$)

We approximate

$$\Delta\nu_{ROT} \simeq \alpha J^2 \tag{5.53}$$

$$I(J) \simeq 2J \exp(-BhcJ^2/kT).$$

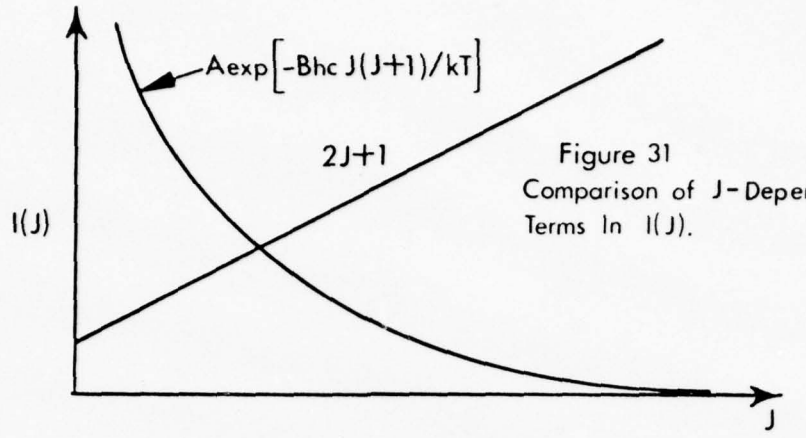


Figure 31
Comparison of J-Dependent Terms In I(J).

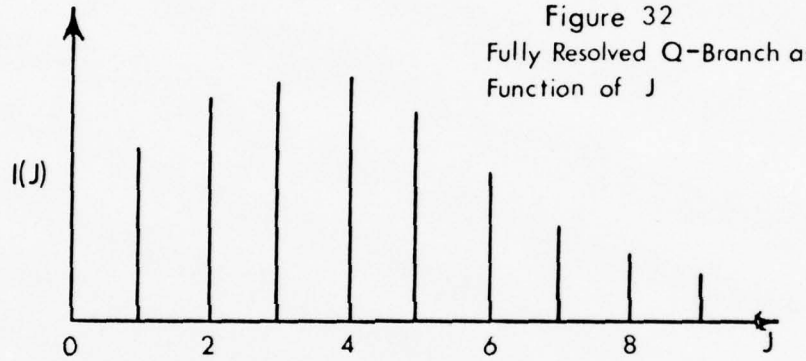


Figure 32
Fully Resolved Q-Branch as a Function of J

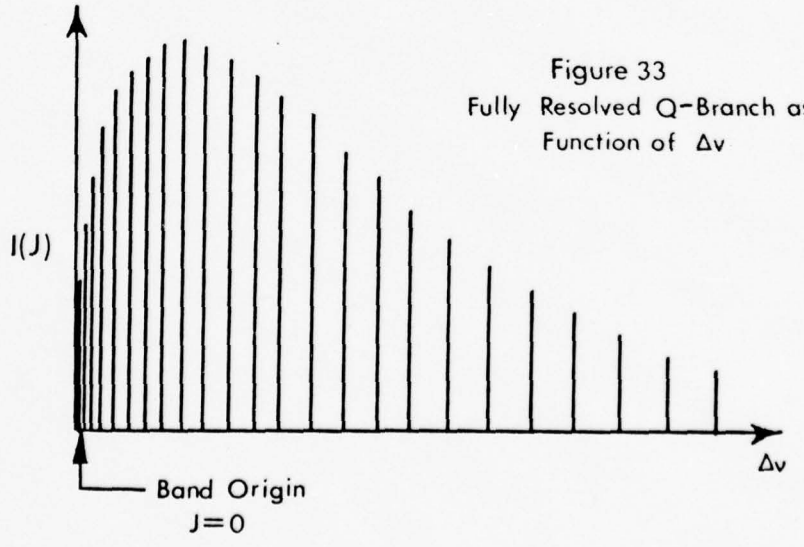


Figure 33
Fully Resolved Q-Branch as a Function of Δv

Then:

$$\frac{dJ}{d(\Delta\gamma)} = \frac{1}{2\alpha J} \qquad J = \frac{\Delta\nu}{\alpha}$$

$$I(\Delta\nu) = 2J \exp(-Bhc\Delta\nu/\alpha kT) \frac{1}{2\alpha J} \tag{5.54}$$

$$I(\Delta\nu) = \frac{1}{\alpha} \exp(-Bhc\Delta\nu/\alpha kT),$$

which is of the form $I(x) = e^{-x}$, as is shown in Fig. 34. Convolution of this shape with a real slit function produces the lineshape which is experimentally detected (Fig. 35). In the case of hot gases, the upper vibrational states may be appreciably populated, giving rise to multiple sub-bands of the shape derived above (Fig. 36).

There are two fundamental ways to obtain a measure of temperature from the Raman scattering due to the Q-branch of a diatomic molecule ($\Delta V = 1$, $\Delta J = 0$). First, we know that the population of various initial V states will be related by the Boltzmann distribution

$$N(V) = N(0) \exp(-E_{VIB}/kT). \tag{5.55}$$

This results in the full Q-branch spectrum shown in Fig. 36 (for a hot gas). If the $\Delta V = 1$ matrix elements are the same (or are known) for $V = 0, 1, 2...$, then we can estimate T_{VIB} from a simple calculation involving the areas of these bands (band-area method). Similarly, it is possible to estimate T_{ROT} from the shape of any particular vibrational-rotational band. Yet another technique involves using the dependence of peak position on T. Of course the most complete usage of the available information involves a full band fit (Lapp, 1974) using a computer to generate band contours for various temperatures until the contour is found which best fits the actual spectrum.

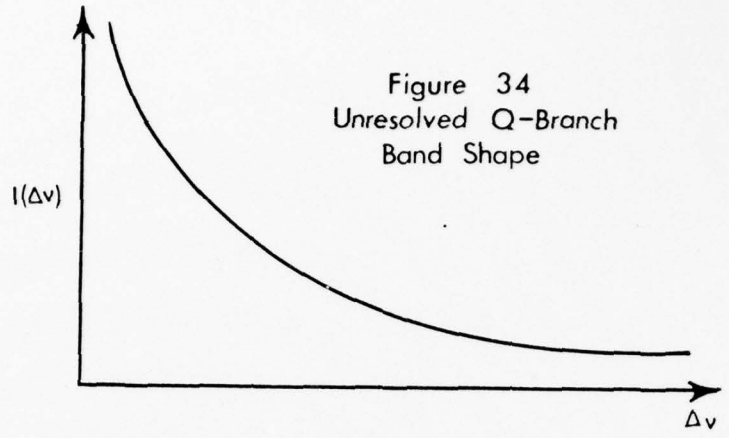


Figure 34
Unresolved Q-Branch
Band Shape

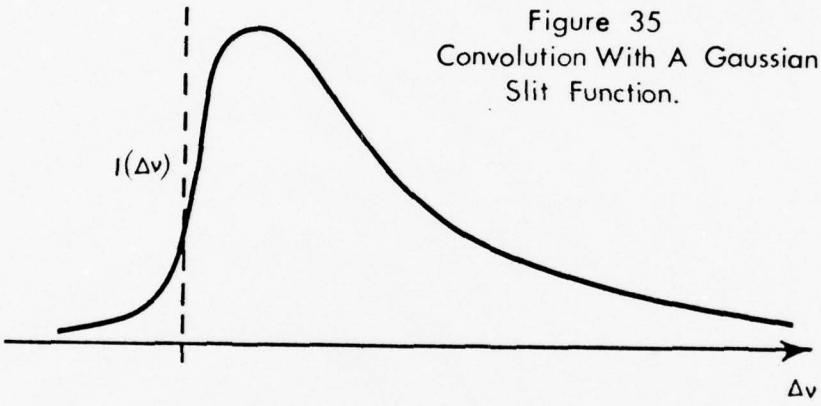


Figure 35
Convolution With A Gaussian
Slit Function.

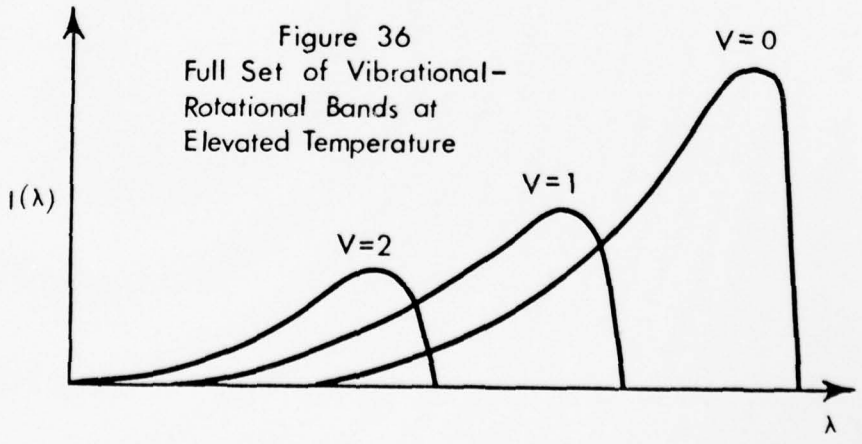


Figure 36
Full Set of Vibrational-
Rotational Bands at
Elevated Temperature

5.3 Experimental Results

The experimental apparatus for performing flame temperature measurements is shown in Fig. 37. The probe is a pulsed (normal mode ≈ 1 msec duration) ruby laser (6943 Å) which delivers approximately 15 Joules per pulse to the sample volume. The vertical laser track is folded back upon itself to obtain an effective doubling of the energy delivered to the sample volume. Collection was via a Nikon f/1.4 50 mm focal length camera lens, normal to the laser track. The combination of magnification (5:1) and spectrometer entrance slit size (10 mm x 0.5 mm) served to define a sample area of 2 mm x 0.1 mm. The torch consists of a water-cooled porous plug burner (2.5 cm dia) placed 2 cm away from a receptor (3.2 cm dia) of similar construction. The burner is supplied with a carefully metered, premixed gas and the receptor is connected to a vacuum source (water aspirator drawing 175 mm Hg). Gas metering is accomplished by means of high quality regulators and critical flow orifices. The entire torch and gas-handling apparatus was loaned to our group by Drs. M. Lapp and C. M. Penney of the General Electric Company Corporate Research and Development Center in Schenectady, New York.

Our purpose was, of course, to obtain a full Q-branch spectrum of reasonable SNR from a single ruby pulse. This would be a first step toward measuring temperatures in turbulent systems, where the optimum measurement interval would be 1 to 20 μsec. The first attempts to measure the flame temperature were unsuccessful, due to low detector sensitivity. Fortunately, later improvements in the PCD increased its SNR for low-light levels to the point where fairly detailed spectra could be obtained from a single pulse. These results are shown in

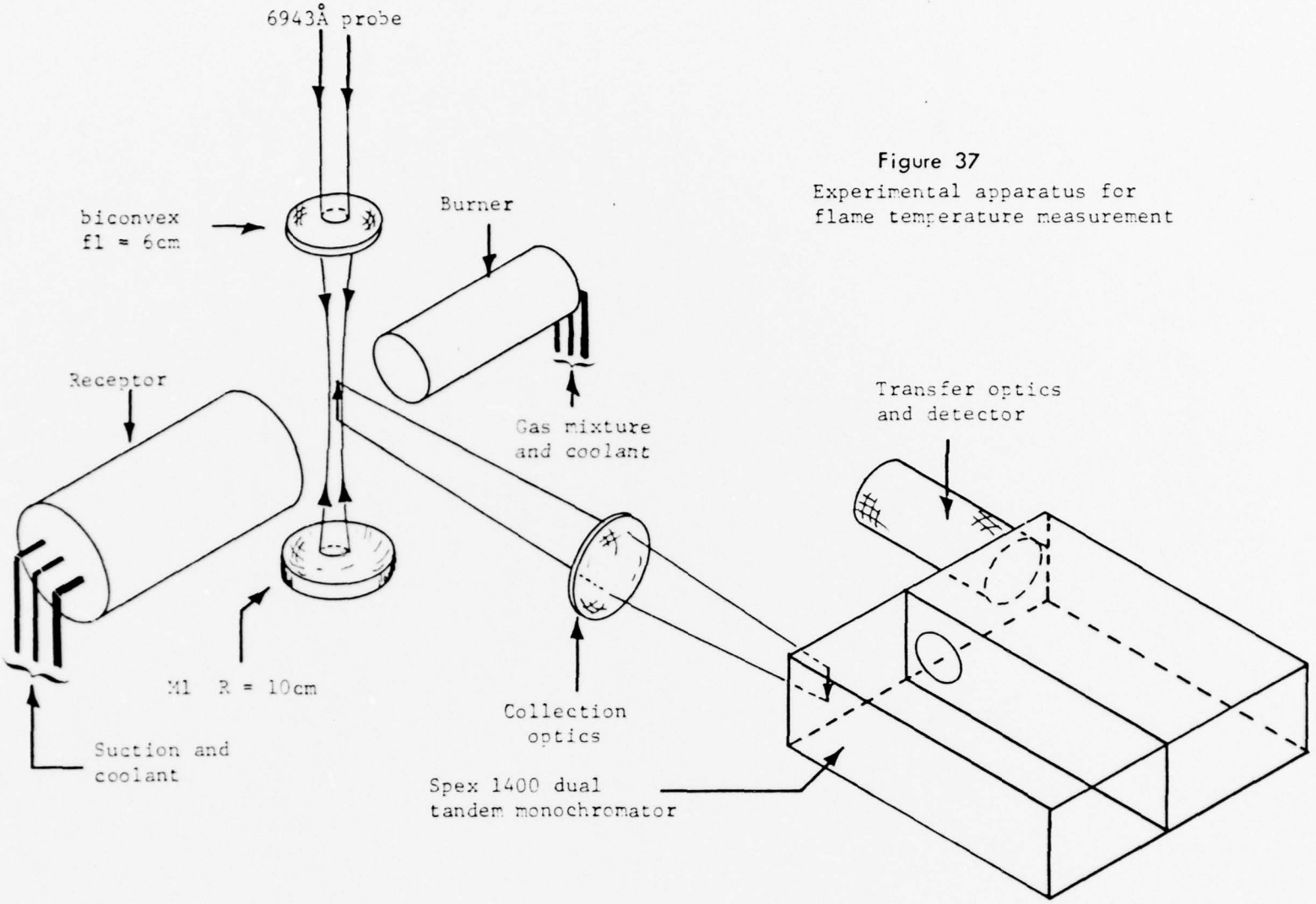


Figure 37
Experimental apparatus for
flame temperature measurement

Figs. 25 and 26 for several H_2-air flames along with data indicating the temperature and stoichiometry of each flame. Also shown is a variation of this experiment in which a rich H_2-O_2 flame was used, with the temperature measured by the O_2 Q-branch scattering. The O_2 "thermometer" (ω_e = 1555 cm^{-1}) is preferable to the N_2 "thermometer" (ω_e = 2331 cm^{-1}) in this temperature range because of the smaller spacings between vibrational states. This allows higher initial V states to be significantly populated, giving us a few more "bumps" to use in the temperature determination. At lower temperatures, a gas such as CO_2 (ω_e = 1265 cm^{-1}) would be the best choice. Note that all spectra are of the anti-Stokes variety, due to the fact that flame luminescence tended to obscure the Stokes shifted spectra.

The temperatures indicated in Fig. 25 were obtained by a simple band-area method, similar to that proposed by Lapp et al. (1973). The vibrational- and temperature-dependent factors associated with the integrated flux S(V) for a particular vibrational band (V to V + 1) are, in the harmonic oscillator, rigid rotator approximations:

$$S(V) \propto (V + 1) \exp[-E(V)/kT]. \tag{5.56}$$

The (V + 1) term arises from the V-dependence of the induced transition moment (Woodward, 1967):

$$\alpha(V, V + 1)^2 \propto (V + 1).$$

Similarly, for an anti-Stokes transition (V + 1 → V):

$$S_{AS}(V + 1, V) \propto (V) \exp[-E(V + 1)/kT], \tag{5.57}$$

where E(V + 1) is the energy of the initial state.

We can define the intensity ratio of two adjacent bands as:

$$H = \frac{S(V+2,\ V+1)}{S(V+1,\ V)} = \frac{V+1}{V} \exp(-\Delta E/kT), \tag{5.58}$$

where

$$\Delta E = E(V+2) - E(V+1) \simeq 2\omega_e x_e hc.$$

Thus:

$$\ell n\left(\frac{VH}{V+1}\right) = \frac{2\omega_e x_e hc}{kT}$$

or

$$T = \frac{2\omega_e x_e hc/k}{\ell n(VH/V+1)} = \frac{\Theta_V}{\ell n(VH/V+1)} \tag{5.59}$$

where $\Theta_V = 3354°K$ for nitrogen. The areas S(V) were estimated from the experimental spectra. Since the "tail" of each vibrational band overlaps the succeeding band, this method of obtaining a vibrational temperature is not particularly accurate. Fortunately the sensitivity of this basic approach is good for the temperatures encountered:

$$\frac{dT}{T} = \left(\frac{T}{\Theta_V}\right) \frac{dH}{H} \tag{5.60}$$

Independent measurements of the flame temperature were not performed during the experiment, since our primary interest was directed toward evaluating the usefulness of our particular experimental techniques, not toward evaluating the basic method of determining the flame temperatures. Basic confirmation of the Raman diagnostic method for flame temperature can be found in papers by Lapp et al. (1971, 1973) and by Leonard (1972). The approximate flame temperatures given in Fig. 25 are in reasonable agreement with thermocouple measurements performed by Lapp (1976) on a similar burner. In the future, it should be possible to obtain much more accurate temperatures by computerized data reduction techniques.

Chapter 6

GAS CONCENTRATION MEASUREMENTS IN A DYNAMIC SYSTEM

6.1 Experimental Configuration

The experimental arrangement described for the flame temperature measurements of Chap. 5 is typical for spectrographic investigations. The collected light from the sample region is separated into its component frequencies and detected in a manner which records intensity as a function of wavelength. An alternative mode of operation was employed for the gas concentration measurements described in this section. Fig. 38 shows the experimental configuration for measuring the concentrations of various gases at selected points downstream from a simple jet.

Fig. 38a Schematic representation.

Fig. 38b Photograph: Closeup of jet, focusing and collection lenses.

Fig. 38c Photograph of complete optical arrangement (except laser). PCD is in background.

The jet itself is a thick walled tube (0.125" O.D. x 0.060" I.D. x 6" long*) with square ends. The length of the tube, about 100 diameters, was chosen in the hope that its characteristics would be relatively insensitive to all operating parameters except pressure, which was measured with a direct reading gauge. The jet exhausts into the ambient laboratory air, not into an evacuated area. If we think of air as an essentially nitrogen environment, this is a two-gas experiment.

*Some dimensions will be given in English units, since the positioning devices used in the experiment were calibrated in inches.

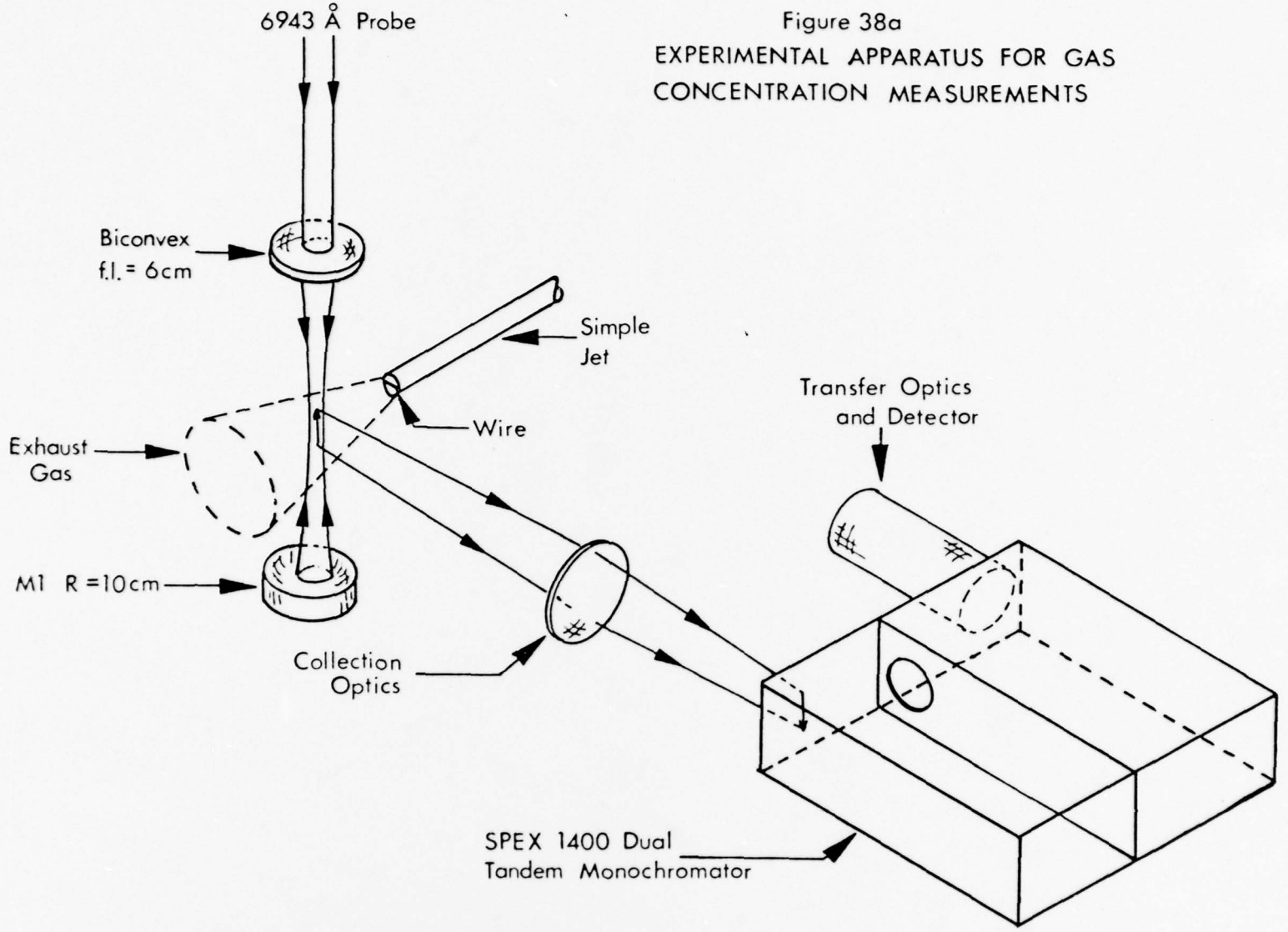


Figure 38a
EXPERIMENTAL APPARATUS FOR GAS CONCENTRATION MEASUREMENTS

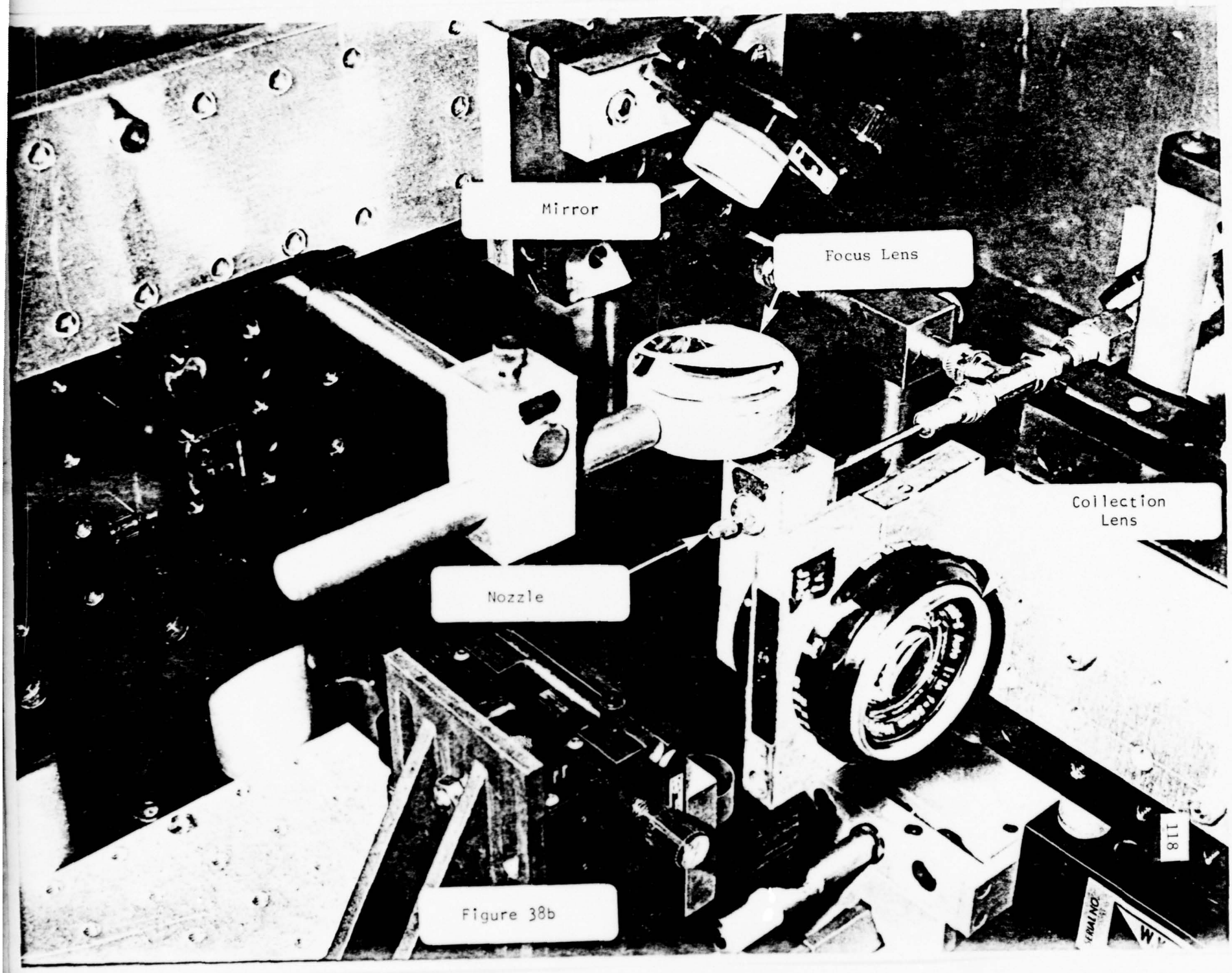


Figure 38b

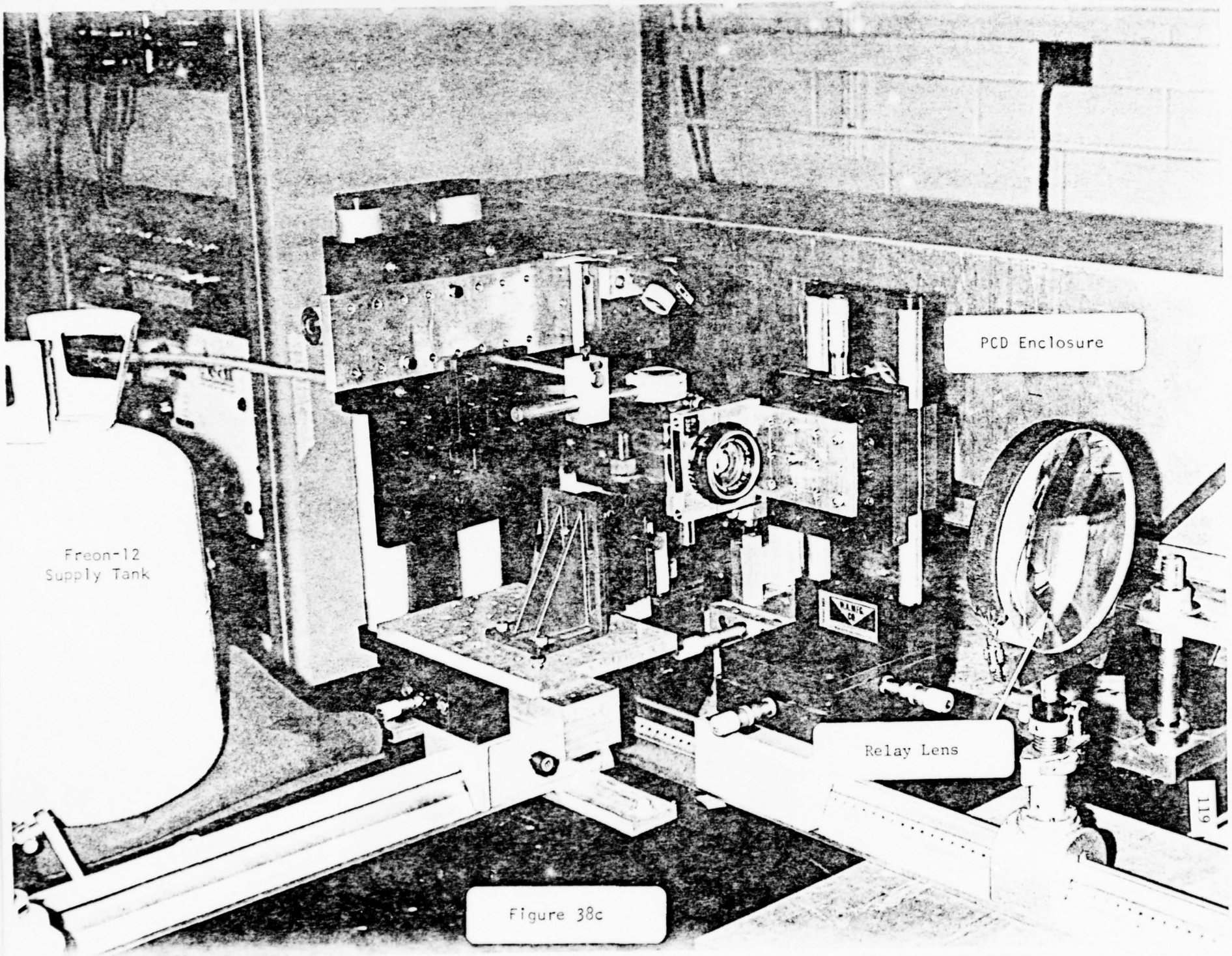


Figure 38c

Optically, the apparatus is nearly the same as in the previously described flame temperature experiment. The probe beam makes two vertical passes through the sample region, scattered light being collected perpendicular to the laser track. However, the detector is not used to record intensity vs. wavelength (spectral dispersion) but "intensity of a single wavelength" vs. "position within the probe beam" (spatial dispersion). In this mode of operation, the spectrometer is used with narrow intermediate and exit slits so that only a single spectral feature is passed.

Fig. 39 gives a more detailed view of the optical path. Light emitted from the sample volume is imaged into the plane of the spectrometer entrance slit. Since the spectrometer is a 1:1 imaging device, the input slit image is replicated at the output slit, with unwanted wavelengths removed. Normally this image would be relayed to the detector by a simple biconvex lens but, in this case, the aspect ratio of the slit image (1 mm x 10 mm) was not very favorable for the camera, so a cylindrical lens was inserted in the relay path, changing the detected aspect ratio to nearly unity. This lens was placed in a non-focusing geometry so that a sharp image was retained in only one dimension, a sufficient condition for the experiment being performed. Broadening the slit image in this fashion increased the ability of the PCD to handle large signals without saturating. The PCD scan pattern was parallel to the resolved elements in the sample volume (i.e., perpendicular to the slit height).

The experiment operates in the following manner: The gas jet is turned on and allowed to stabilize (approximately 2 sec); then the ruby laser is pulsed, providing 1 msec of illumination in the sample volume.

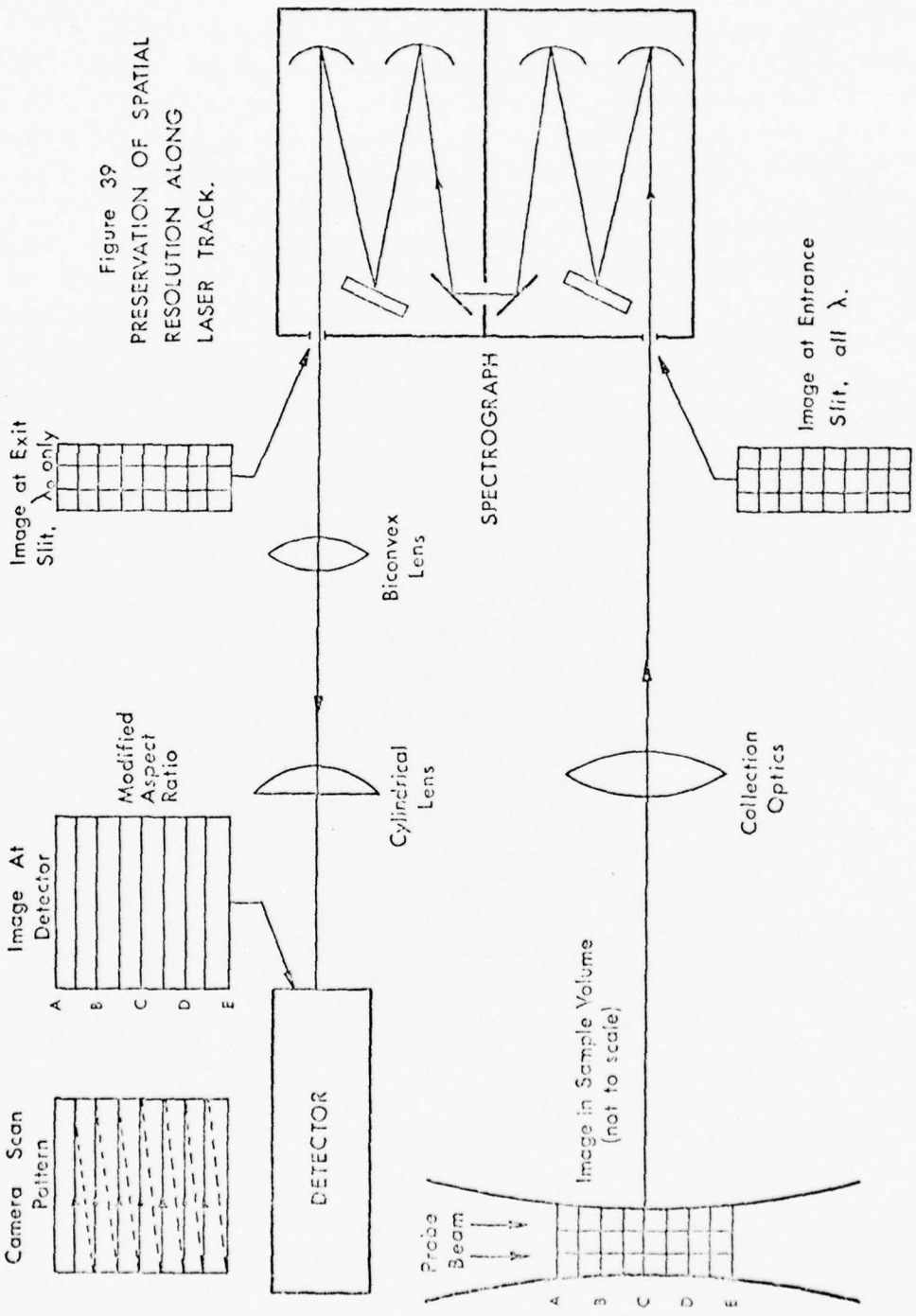


Figure 39
PRESERVATION OF SPATIAL RESOLUTION ALONG LASER TRACK.

Light of a selected wavelength is relayed from the sample volume to the detector. After a delay of 30 msec (lifetime of the intensifier output phosphor), the PCD makes a single scan, recording the intensity in each of 256 elements along the slit height. Due to the nature of the optics employed, light scattered from point A (Fig. 39) is detected and stored independently of light scattered from points B, C, D, etc. Thus the process is, in fact, an ensemble of 256 simultaneous light scattering experiments, each operating on distinct, adjacent parts of the scattering volume.

6.2 Measurement Characteristics

In practice, the jet exhausts a Raman active gas (Freon-12, $CF_2C\ell_2$) into the atmosphere and the spectrometer is tuned to an appropriate Raman line for this gas (677 cm^{-1}). The active volume is essentially a cylinder, 2 mm high by 0.1 mm in diameter, each spatially resolved element being approximately 0.01 mm high by 0.1 mm in diameter. (.0004" x .004"). The sample diameter is defined primarily by the diameter of the probe beam in the sample volume. Reducing this effective diameter by closing the entrance slit of the spectrometer naturally results in a reduction in signal strength. The amount of Raman light received by the detector from each spatial element is

$$W_R = N_G W_L L \frac{\partial\sigma}{\partial\Omega} \Omega\eta$$

where

W_R = Watts of Raman signal

W_L = Watts of input laser power

$\frac{\partial\sigma}{\partial\Omega}$ = Differential cross section per gas molecule

Ω = Solid angle of collection optics

L = Scattering length

N_G = Number of molecules per unit volume

η = Total efficiency of optics, spectrograph, etc.

If one is careful about the optics for both the probe beam and scattered light, it is found that for each spatial element in the sample volume the relative Raman energy is just $W_R \propto N_G$--i.e, we have a means of measuring changes in the concentration of a gaseous species in the sample volume. Spatial resolution is essentially .005(L), where L is the effective track length of the probe beam. Following are several

important advantages which accrue from the use of this particular system:

1. All data are taken simultaneously. Since the laser is pulsed, we essentially get a "snapshot" of the sample volume, taken in Raman scattered light, i.e., a "Ramanograph."
2. Spatial resolution. With different optics, spatial elements as small as 30 μm could be resolved. Working with a large jet is difficult because of limitations imposed by the spectrograph entrance slit and grating dimensions.
3. Time resolution. The current experiment takes place in 1 msec, requiring 5 to 15 Joules of input energy. Using an appropriate laser, this duration could be reduced to well below 10 μsec, allowing us to "freeze" even very rapid gas flows.
4. Species selectivity. Nearly all species of interest have distinct Raman signature frequencies. It is quite easy, for instance, to distinguish the component gases in a nitrogen-oxygen gas mixing experiment, which would be rather difficult by some other method (e.g., Schlieren photography).
5. Insensitivity to other parameters, especially laser energy and gas velocity.

6.3 Experimental Parameters

The gas jet inlet pressure was recorded for each experimental run, allowing us to make estimates of other parameters of interest. Most of the experiments were performed with Freon-12 as the exhaust gas, due to its favorable Raman cross section and low toxicity.

The notation used in this section is:

P = pressure

ρ = density

U = velocity

M = Mach number

a = speed of sound

γ = specific heat ratio (C_p/C_V)

T = absolute temperature

η = dynamic viscosity

ν = kinematic viscosity (η/ρ)

R_e = Reynolds number

D = tube diameter (0.159 cm)

L = tube length (15 cm)

R = gas constant [8.3×10^7 ergs $(\text{g-mole})^{-1}$ deg^{-1}]

m = mass (g/g-mole)

Variables such as ρ_o, T_o, and P_o refer to some reference state which we take to be the tank (or stagnation) conditions. Variables such as ρ_s, T_s, and P_s refer to conditions of standard temperature and pressure (STP). Constants for Freon-12 at STP are:

$\rho_s = 6.33 \times 10^{-3}$ g/cm^3

$\eta_s = 1.27 \times 10^{-4}$ g/cm/sec

$\nu_s = .02$

$\gamma = 1.137$

$a_s = 1.55 \times 10^4$ cm/sec

$m = 120.9$ g/g-mole.

For isentropic (inviscid), adiabadic flow we know that (Liepmann and Roshko, 1957):

$$\frac{P_o}{P} = \left(1 + \frac{\gamma - 1}{2} M^2\right)^{\gamma/(\gamma-1)} \tag{6.1}$$

and

$$\frac{P}{P_o} = \left(\frac{\rho}{\rho_o}\right)^{\gamma} = \left(\frac{T}{T_o}\right)^{\gamma/(\gamma-1)} \tag{6.2}$$

from which we can calculate the critical pressure (P_c) for sonic ($M = 1$) flow:

$$\frac{P_o}{P_c} = \left(\frac{\gamma + 1}{2}\right)^{\gamma/(\gamma-1)} = 1.733. \tag{6.3}$$

We can calculate the maximum variation in the speed of sound since

$$a = (\gamma RT/m)^{1/2} \tag{6.4}$$

and

$$\left(\frac{T}{T_o}\right)_{max} = \left(\frac{P}{P_o}\right)^{\gamma/(\gamma-1)}_{max} = (1.733)^{.120} = 1.07.$$

Thus:

$$\left(\frac{a}{a_o}\right)_{max} = 1.04.$$

From Eq. 6.1 we can find the velocities for subsonic flow:

$$M^2 = \frac{2}{\gamma - 1}\left[\left(\frac{P_o}{P}\right)^{\gamma/(\gamma-1)} - 1\right] \tag{6.5}$$

by assuming that the exit pressure is the same as the ambient pressure P_s. This yields valid results up to the critical pressure (P_o = 10.8 PSIG), when the flow becomes choked. For higher tank (inlet) pressures, $P_o > P_c$, the flow velocity remains sonic at the nozzle exit plane, but the exit pressure is now defined by the critical pressure ratio

$$\frac{P_o}{P_e} = 1.733. \tag{6.6}$$

Once the gas leaves the nozzle, expansion causes an increase in velocity, so that the final velocity attained is supersonic.

We can check the validity of assuming that the flow is inviscid by estimating the thickness (δ) of the viscous boundary layer at the exit of the jet. This estimate is (*Landau and Lifshitz, 1959*):

$$\delta = (\nu L/U)^{1/2} \tag{6.7}$$

where U is a characteristic velocity. We can maximize ν by letting

$$\nu = \frac{\eta}{\rho_{min}} = \frac{\eta}{\rho_s} = \nu_s.$$

We choose $U = U_e$ (exit velocity) even though U is not constant in the tube since this changes our estimate of δ by less than 2:1. Thus, for a typical exit velocity (M = 1)

$$\delta = \left[\frac{(.02)(15)}{(1.55 \times 10^4)}\right]^{1/2} = 4.4 \times 10^{-3} \text{ cm}$$

or about 6% of the tube radius, so viscous effects are quite small.

The value of P_{tank} is related to the exit velocity, pressure, and

Reynolds number (all in the plane of the end of the tube), as shown in Table III below. The Reynolds number is defined by:

$$R_e = \frac{DU\rho}{\eta} = \frac{DU\rho_o}{\eta}\left[\frac{P_e}{P_o}\right]^{1/\gamma} = \left(1.23 \times 10^5\right) M \left[\frac{P_e}{P_o}\right]^{0.88}, \tag{6.8}$$

the characteristic distance (D) being the inner diameter of the tube. Conditions for $M < 1$ were calculated from Eq. 6.5 with $P_{exit} = P_s =$ 760 Torr, and conditions for $M = 1$ were calculated from Eq. 6.6.

TABLE III

SUMMARY OF GAS JET PARAMETERS

P_{tank} PSIG	P_{tank} Torr	U_{exit} Mach number	P_{exit} Torr	R_e (exit)
2	863	0.23	760	2.8×10^4
5	1019	0.52	760	6.4×10^4
10	1277	0.94	760	1.2×10^5
20	1794	1	1035	1.6×10^5
40	2829	1	1632	2.4×10^5

6.4 Experimental Results

Three different jet configurations were used:

1. Simple open jet, no obstructions.
2. Jet with 0.25 mm (.010") wire across exit aperture. (Wire is 1/6 jet dia.)
3. Jet with 0.125 mm wire across exit aperture (.005" or 1/12 jet dia).

In each case, the laser track was centered on the jet axis, simultaneously perpendicular to the nozzle axis and any nozzle obstructions. Data were taken at several points downstream from the jet (0.25 to 15 jet diameters) and at a variety of exit velocities. Although usable data were obtained from a single laser pulse, most curves shown in Figs. 40 through 45 represent averaged results (4 to 20 pulses). Each averaged histogram is essentially identical to its component sub-experiments but shows somewhat less "scatter" than a single-shot experiment. Note: See p. 132 for these figures.

The series T3DP# is typical of the "open jet" results. Each histogram is a display of "gas concentration" vs. "position in the sample volume." T3DP6 serves to define the horizontal scale, since we know that the nozzle size is 1.5 mm. The Freon-12 is well localized at this distance (0.25 D) downstream and evenly distributed across the exit aperture. Total spatial coverage is nearly 3 mm. The vertical scale is in arbitrary units and is kept constant (insofar as possible) within each series. Samples at larger distances (X) from the nozzle tip show the Freon-12 becoming less distinct as mixing with the ambient air occurs. The open jet displayed some interesting structure at higher exit velocities, as seen in the series T3DR# in Fig. 41 (maximum

available inlet pressure at the time). The regular oscillation in peak shape (concave/convex) with distance bears further investigation.

In order to evaluate our ability to detect disturbances in the jet exhaust, the jet was deliberately perturbed by attaching a small wire to the front surface of the nozzle (Fig. 39). As shown in Fig. 42, the results were clearly visible. Several cross checks were made to insure the validity of these results. Run T5FC20 (Fig. 43) shows the overall system response vs. spatial position. No jet was used and the spectrometer was set to pass the N_2 (2331 cm^{-1}) Raman line from the ambient air. T5FF10 was taken while running air in an obstructed jet. The lack of structure substantiates the claim that the system is sensitive to gas concentration, not gas velocity.

Another interesting validity check is shown by runs T5FB5 and T5FE5. Both histograms were obtained under the same operating conditions except that the detector was sensitive to Freon-12 in the first run and to nitrogen in the second. We would expect that the "wings" of the nitrogen data would be flat since air contains a very stable concentration of nitrogen. The curvature is instrumental in this case, following the same response profile as in T5FC20. With this in mind, these two runs show that regions of low Freon-12 concentration have a high nitrogen (air) concentration, indicating that little compression or expansion of the gases takes place.

Not all of the data exhibit the simple structure shown in the instances just discussed. A series of experiments detailed in the last two sets of graphs (Figs. 44 and 45) exhibits a considerable amount of secondary structure very near the mouth of the jet (at the higher exit velocities). This secondary structure is a strong function

of the axial distance X. In the T4DA# series (Fig. 44), secondary structure was observed clearly for X = .015", .020", .025" but disappeared entirely for X > .030". Thus, the concentration profile changed radically over a distance of 1/12 jet diameter. Note also that T4D4 represents a single laser pulse from the series comprising the averaged histogram T4DA10. Fig. 44 details the variation of secondary structure with pressure, keeping X fixed. Finally, the results shown in Fig. 45 indicate a certain lack of reciprocity between runs taken while detecting nitrogen as opposed to Freon-12. None of the secondary structure was seen in any of the nitrogen runs, indicating that there were significant density changes in the Freon-12 under these conditions.

Figures 40 - 45

GAS JET DATA

All data taken refer to the same jet. The nozzle is a heavy walled tube with square ends.

Length = 15 cm (6")

O.D. = 3.2 mm (1/8")

I.D. = 1.6 mm (1/16")

The probe beam is 6943 Å, 15 Joules per pulse, 1 msec duration.

Raman shifts: Freon-12 ($CF_2C\ell_2$) = 677 cm^{-1}

O_2 = 1555 cm^{-1}

N_2 = 2331 cm^{-1}

Notation:

DET = Sp Detector is sensitive to "Sp" species. FR = Freon-12.

N = # Number of laser pulses was #

X = # Distance downstream from nozzle tip. Numbers in parentheses () are in mils (.001"). These numbers have even values since the jet translator was calibrated in English units.

P = #(Sp) Jet exhaust gas is "Sp" species at # PSIG. Pressures below 5 PSIG are very approximate.

Each histogram has a six-character identifier. Identifiers progress in a fairly orderly sequence so that runs with very similar identifiers were taken at nearly the same time. Almost all histograms are averages over several laser pulses. In all cases, the individual spectra comprising the plotted histogram are identical to the averaged histogram in all major respects (except lower SNR). Parameters which do not vary are stated only once.

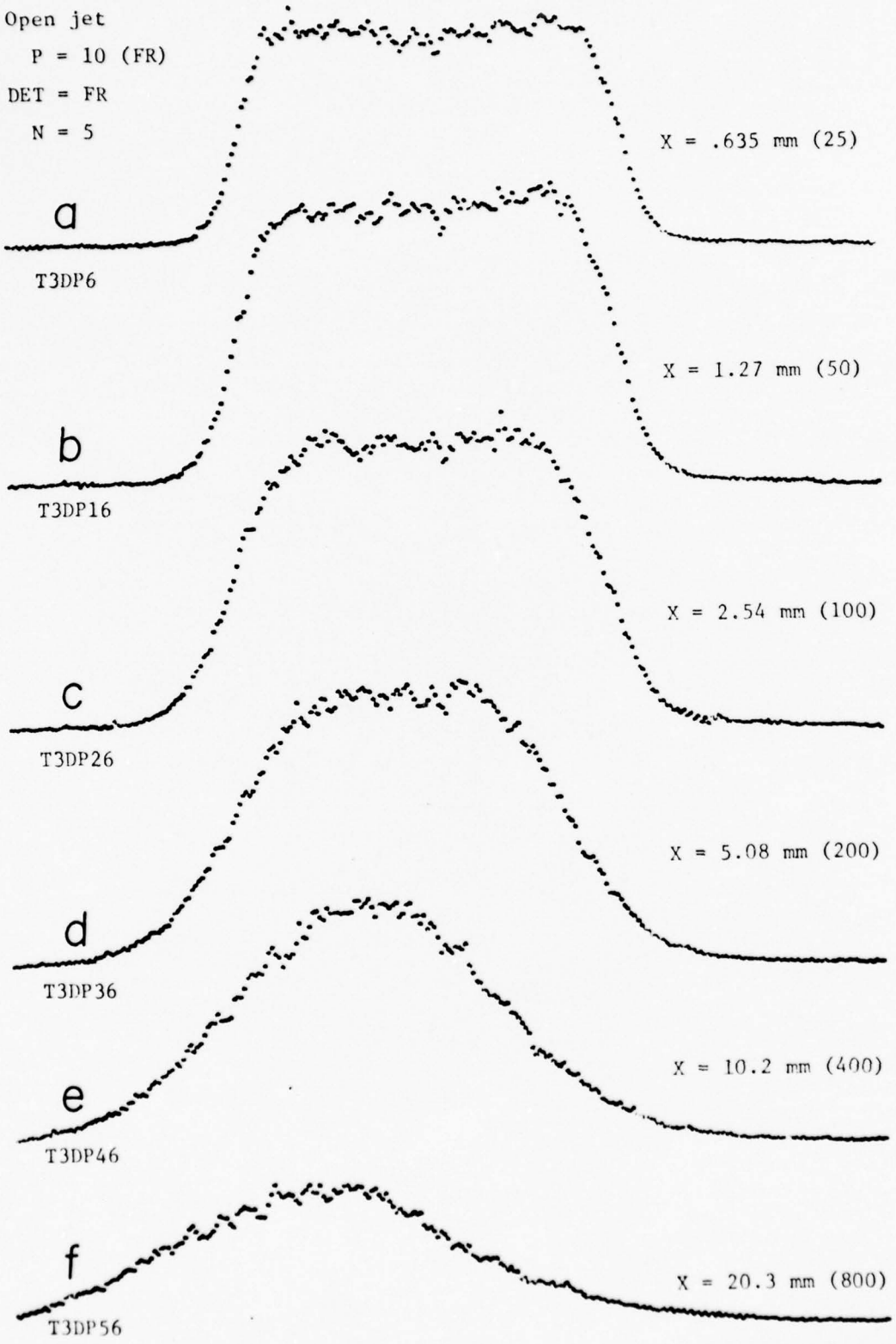

Open jet
P = 10 (FR)
DET = FR
N = 5
X = .635 mm (25)
a
T3DP6
X = 1.27 mm (50)
b
T3DP16
X = 2.54 mm (100)
c
T3DP26
X = 5.08 mm (200)
d
T3DP36
X = 10.2 mm (400)
e
T3DP46
X = 20.3 mm (800)
f
T3DP56

Figure 40

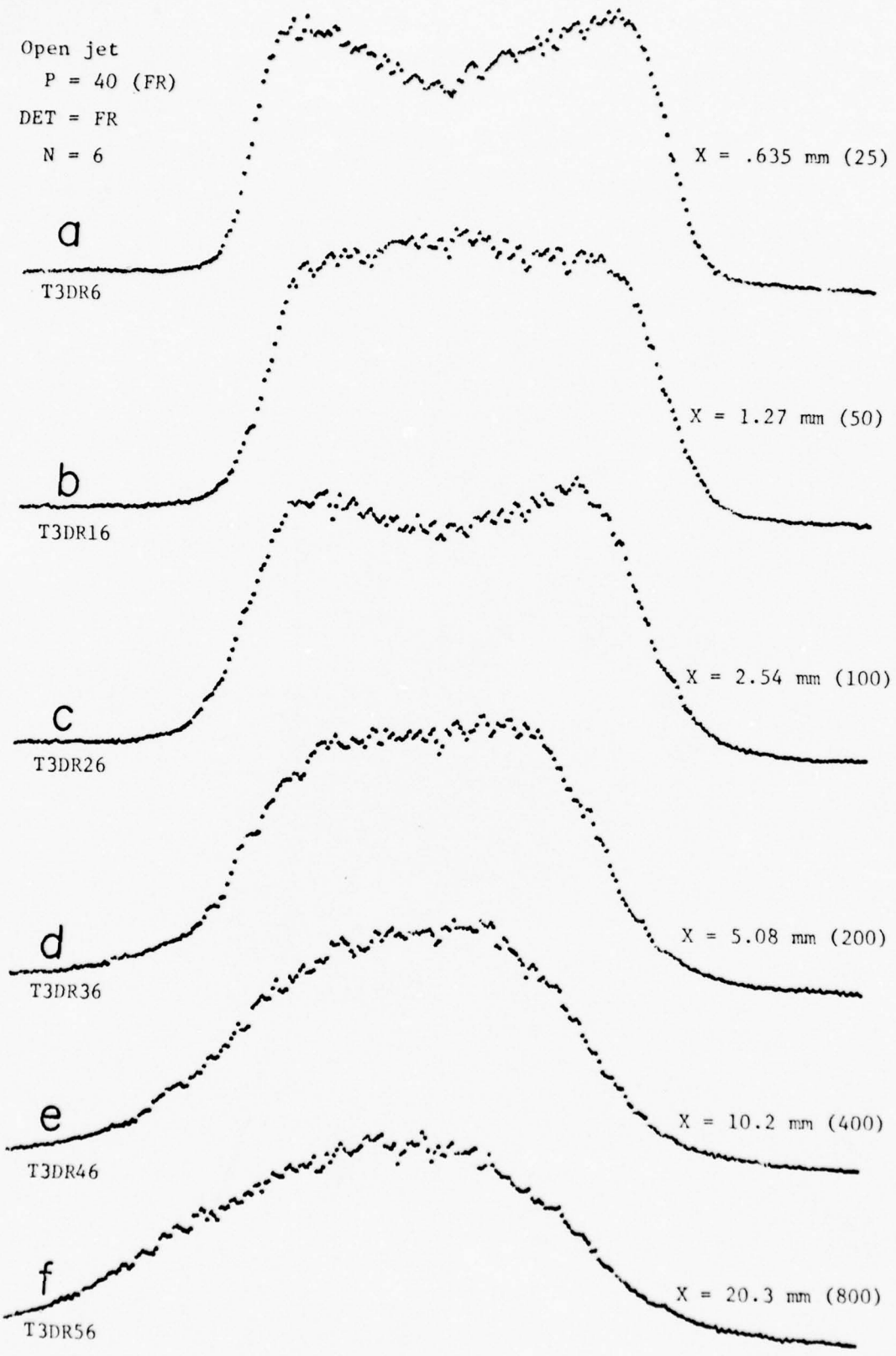

Open jet
P = 40 (FR)
DET = FR
N = 6
X = .635 mm (25)
a
T3DR6
X = 1.27 mm (50)
b
T3DR16
X = 2.54 mm (100)
c
T3DR26
X = 5.08 mm (200)
d
T3DR36
X = 10.2 mm (400)
e
T3DR46
X = 20.3 mm (800)
f
T3DR56

Figure 41

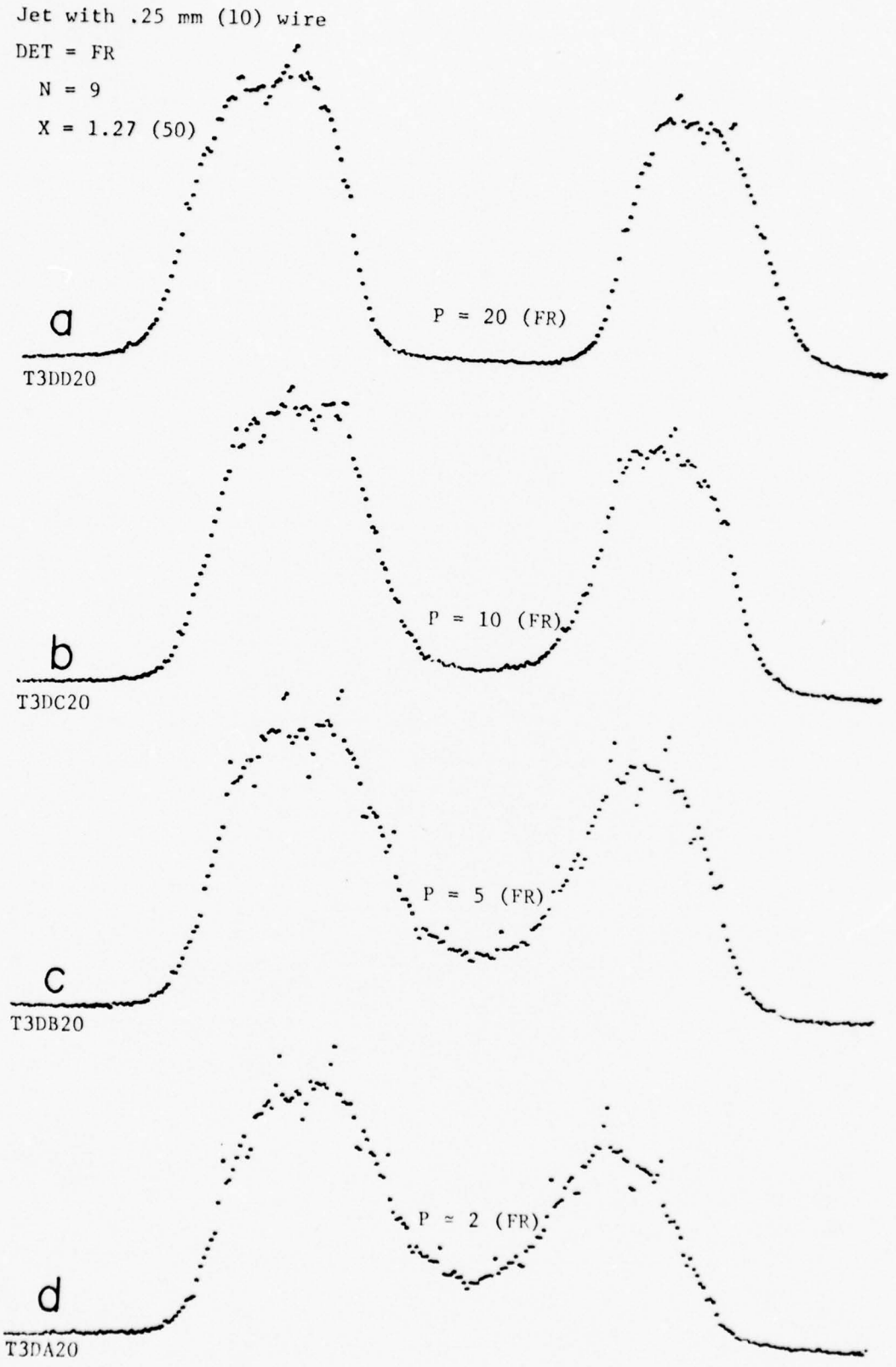

Jet with .25 mm (10) wire
DET = FR
N = 9
X = 1.27 (50)
a
P = 20 (FR)
T3DD20
b
P = 10 (FR)
T3DC20
c
P = 5 (FR)
T3DB20
d
P = 2 (FR)
T3DA20

Figure 42

Jet with .127 mm (5) wire

X = .381 mm (15)

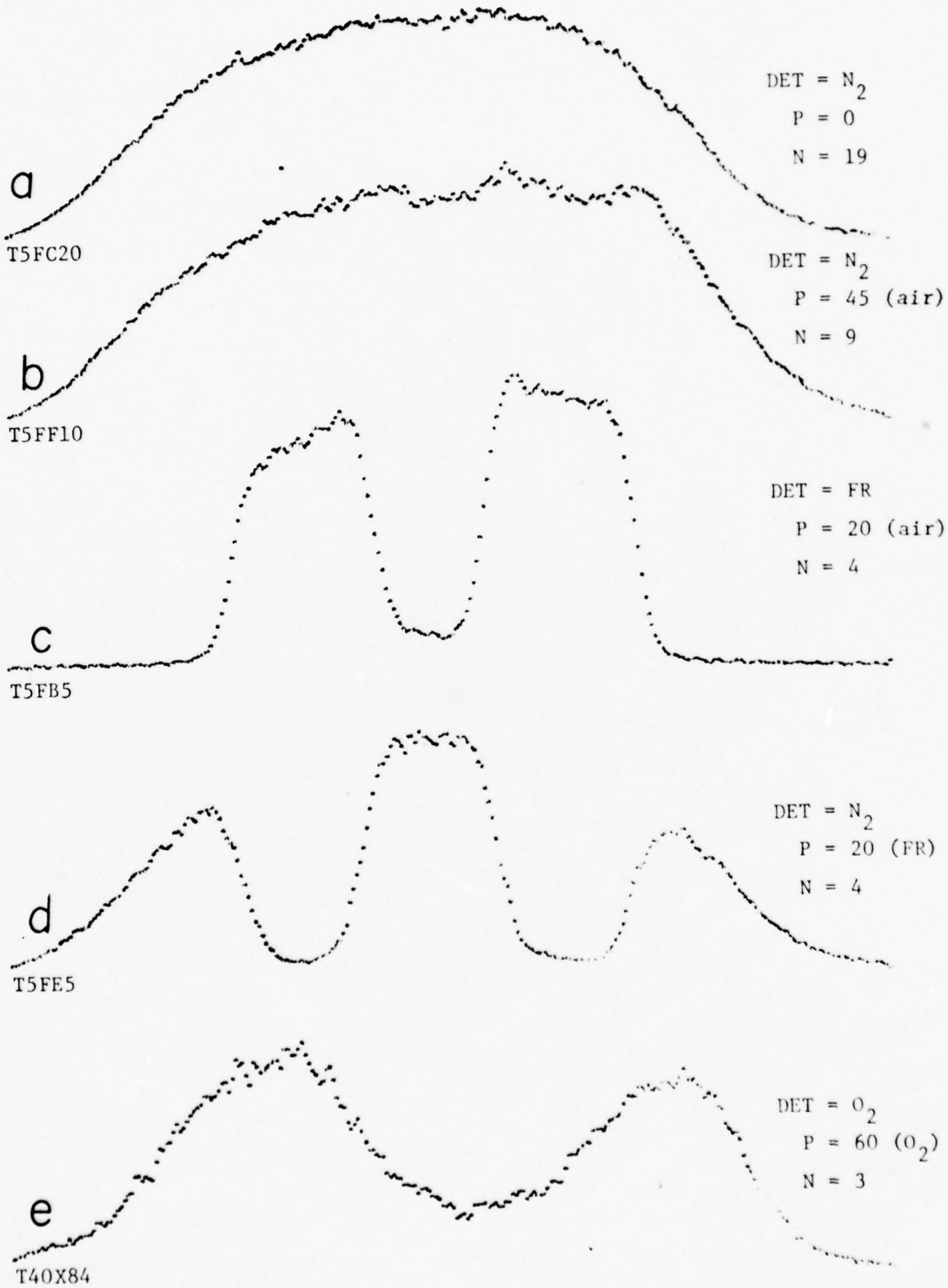


Figure 43

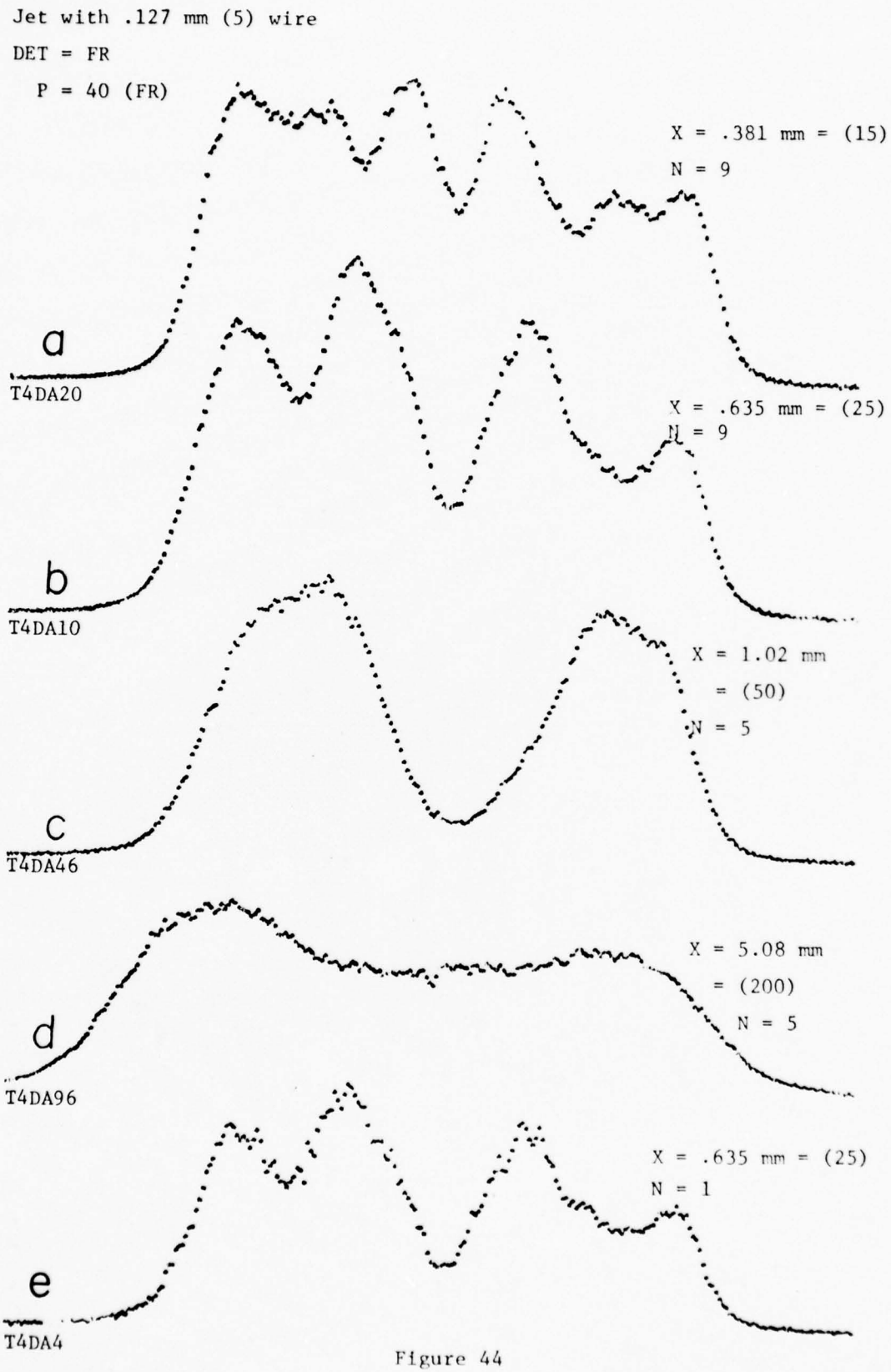

Jet with .127 mm (5) wire
DET = FR
P = 40 (FR)
X = .381 mm = (15)
N = 9
a
T4DA20
X = .635 mm = (25)
N = 9
b
T4DA10
X = 1.02 mm
= (50)
N = 5
c
T4DA46
X = 5.08 mm
= (200)
N = 5
d
T4DA96
X = .635 mm = (25)
N = 1
e
T4DA4

Figure 44

Jet with .127 mm (5) wire

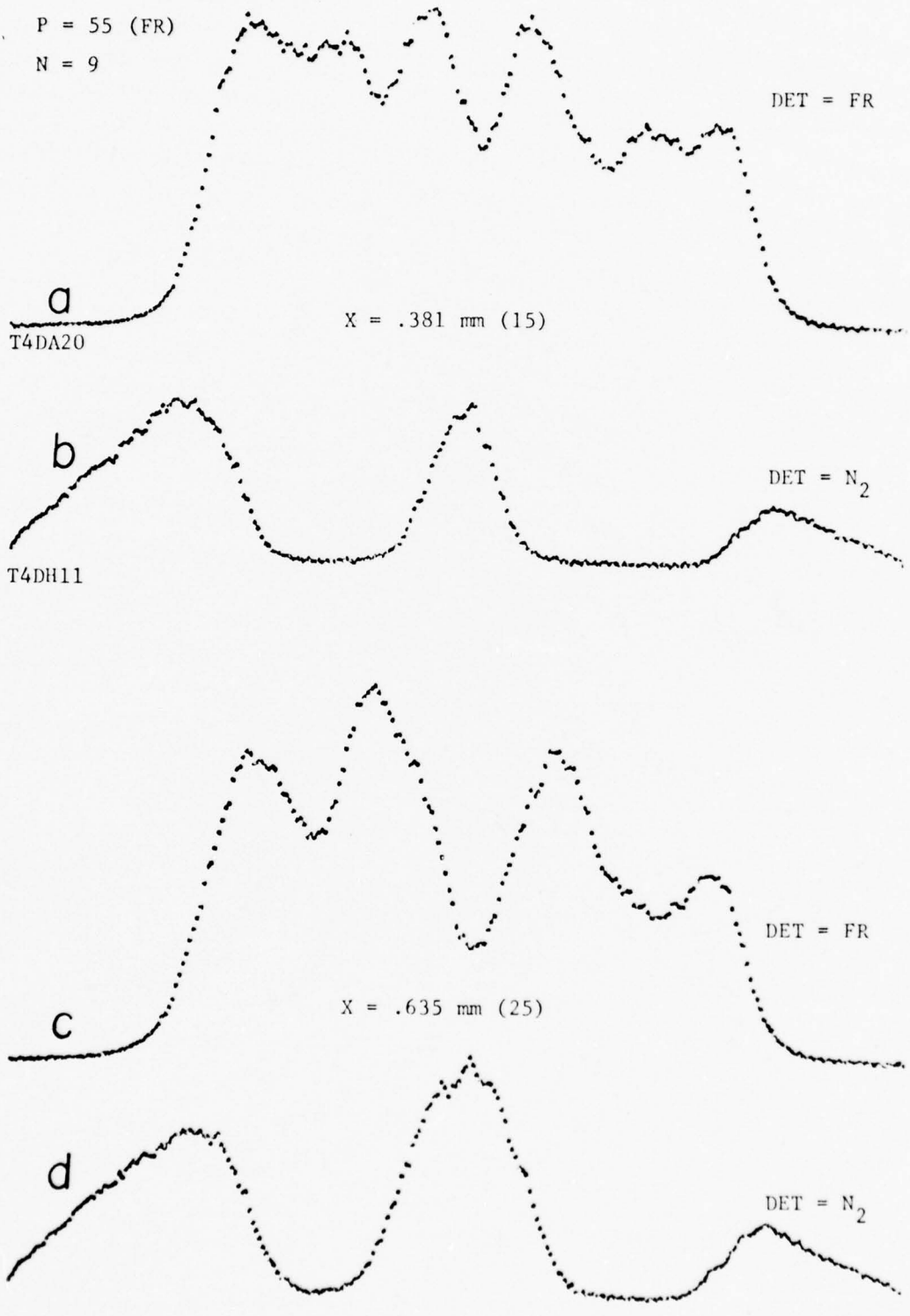


Figure 45

6.5 Conclusions

The PCD-Raman scattering system of detecting relative concentrations of gaseous molecules appears to be a powerful tool in the diagnosis of gas dynamic systems. Of course, the information collected to date is not definitive in the sense that most of our attention was directed toward the operation of the parallel-channel detector, and very little was directed toward refining the gas jet or its operating conditions. However, the basic capability has been clearly demonstrated. By working in collaboration with fluid dynamicists, it will be possible to obtain accurate, reliable data under controlled conditions, thereby making a significant contribution to the field. We have not attempted to perform a detailed analysis of the current data, partly because of its unrefined nature, and partly because of our lack of experience in the mathematical formalisms associated with the field of fluid mechanics.

Chapter 7

CONCLUDING REMARKS

7.1 Current Capabilities

A parallel-channel spectrographic detection system has been developed for use in visible and near-infrared light scattering experiments. The design goal of quantum-limited sensitivity over at least 100 simultaneously active acquisition channels has been met. This combination of high sensitivity and parallel acquisition has enabled us to perform investigations which would have been impractical (or impossible) if conventional detectors were employed.

Historically, any dramatic increase in our ability to probe the laws of nature has opened many new avenues for meaningful scientific research and technological development. Ultra-fast measurements are not a panacea for all experimental difficulties, but it does seem likely that a wide variety of potentially important applications will be centered around the use of the PCD or a similar device. Our demonstrated ability to make high-speed measurements of gas temperatures and concentrations should, if properly pursued, make a fundamental contribution to our understanding of fluid flow and combustion processes. Even though our initial goal in developing the PCD was its use in the investigation of very weak (stationary) spectra, we now feel that its greatest impact will be in the area of transient detection, particularly when the PCD is used in conjunction with a pulsed laser.

In the past, the use of an intermittent (less than 1 Hz) light

source imposed tremendous hardships on the spectroscopist. The advantages of pulsed sources (large signal return during the pulse, the ability to induce nonlinear behavior in samples, and the wide range of available dyes for tunable lasers) were often offset by problems caused by low average power, pulse-to-pulse energy variations, and the like. The PCD greatly reduces these experimental difficulties, allowing the researcher much more freedom to capitalize on the advantages of the pulsed probe.

7.2 Future Improvements

The PCD system is still an open-ended endeavor from the technological standpoint. The basic implementation is fixed by our initial choice of imaging devices, but there are still several areas for further development. For example:

1. Greater resolution might be obtained by investigating better ways to eliminate undesirable interactions between the camera and the intensifier. Performance might be significantly enhanced merely by using a longer fiber-optic bundle between the two devices, allowing optimum positioning of the camera tube in its yoke while keeping the intensifier farther removed from any fringe magnetic fields.
2. The use of a correlation type of photon detector (matched filter) is practical now that high-speed solid-state correlators are available. This technique might yield extremely reliable event detection even in the presence of high ambient electrical noise.
3. Implementation of the Selective-Scan Technique. Our principal activity was in transient-event recording, so there was little stimulus to develop the necessary hardware and software. However, this would be a valuable technique for the investigation of stationary spectra.
4. The use of a gated intensifier would significantly reduce background noise when used in conjunction with a pulsed probe. At present, the detector gate interval

is implied by the camera frame period, which is typically 50 msec. For experiments involving luminous sources (such as a flame) and short probe pulses (less than 0.5 msec), a reduction in background radiation of at least 100:1 could be realized.

5. A dual grating subtractive dispersion filter (Siemon, 1974) in tandem with a single grating spectrograph would provide a much higher scattered light rejection ratio than can be obtained from the current two-stage (additive dispersion) spectrograph. The additive dispersion spectrograph has a relatively high stray light level because of the necessity for operating with wide (1 cm or more) intermediate and exit slits in order to obtain adequate spectral coverage. In a subtractive dispersion instrument, light is dispersed by the first grating and then passes through the intermediate slit (usually wide) which is sized to pass only the desired wavelengths. The second grating reforms the selected band into a line image which can pass through the (narrow) output slit and then into the final dispersive section. The filter bandwidth is controlled by the intermediate slit width and the band center is set by rotation of the gratings. This would provide a tunable, sharp cutoff, bandpass filter which would greatly enhance our ability to study samples with large Rayleigh scattering cross sections.

The capabilities of the PCD could be further extended by making

full use of its inherently two-dimensional nature. There are three fundamentally distinct methods of processing the information obtained from the camera tube. These are:

1. Zero-dimensional: The video signal is continuously integrated (or photon counted) without regard to the read-beam position. This results in a one-channel detector similar to a PMT.
2. One-dimensional: The video signal from each scan line is recorded separately. This is the detection method currently employed, which results in a 100-channel (minimum) detector.
3. Two-dimensional: The video signal from each pixel is recorded separately, resulting in a 100 x 100 or 10,000-channel detector.

With two-dimensional detection, it is possible to perform a variety of interesting experiments. For instance, a cross-dispersed (prism-echelle) spectrograph can be constructed which folds a broad linear spectrum into a rectangular array of spectral elements. It should be possible to obtain a spectral coverage of 3000 cm^{-1} with 1 cm^{-1} resolution by this method, thereby retaining high resolution without sacrificing broad coverage. Sensitivity per channel would be reduced since the cross-dispersed spectrograph requires a very short entrance slit, but for many applications, such as species identification (see Appendix A), this would be a very favorable compromise.

A second general class of experiments which would benefit from two-dimensional recording involves spectrographic detection as a function of wavelength and "spatial position within the sample." This is

simply a combination of "spatial dispersion" and "spectral dispersion," each of which has been demonstrated individually (Chap. 5 and Chap. 6, respectively). If the flame experiment were performed in this manner, we would be able to specify temperature as a function of position along the laser track instead of detecting only the average temperature in the sample volume.

Finally, the natural extension of the gas jet experiments of Chap. 6 would be to use the spectrograph as a narrow bandpass optical filter (as before) but record the relative gas concentration as a function of two position variables. One can imagine bouncing the probe beam back and forth between two plane mirrors to form a sheet or plane of illumination, and monitoring the gas density as a function of position within the plane. This would allow us to simultaneously probe an entire cross section of the jet exhaust.

A summary of the two-dimensional imaging modes follows:

1. $I = f(\lambda_1,\lambda_2)_x$: Cross-dispersed spectral coverage of a point source.
2. $I = f(\lambda,x)$: Spectrally dispersed coverage of a spatially resolved line source.
3. $I = f(x,y)_\lambda$: Two-dimensional image of a plane source at a single wavelength.

By a suitable choice of optical apparatus, it is possible to produce $x = g(t)$, i.e., to turn spatial resolution into temporal resolution. Temporal resolutions in the picosecond range are possible in this way.

7.3 Alternative Approaches to Parallel-Channel Detector Design

There is still no definitive solution to the problem of selecting the best possible imaging devices for use in a parallel-channel detector. This is partly due to a lack of information regarding the performance characteristics of existing low-light level imaging systems. We intend to test our PCD further in order to determine the following: modulation transfer function (MTF) at various input light levels; pulse-height distribution for single-photon events; dynamic range limitations in the photon-counting and integration modes; intensifier response (in each pixel) as a function of wavelength, intensity, and temperature; imaging characteristics for point and line sources (vs. intensity); image lag and image retention time as a function of input illumination and detector temperature. Since these tests provide the only quantitative basis for evaluating a low-light level system, it is hoped that other researchers in the field will be able to publish comparable information, thereby allowing definitive comparisons to be made among the various devices and techniques.

The second major factor affecting the selection of imaging devices is one of intended use, since an optimum choice for the measurement of transient spectra might be quite different from the choice for measuring weak stationary spectra. For instance, one can argue that the best system for stationary spectra is just an un-intensified SEC camera. This approach has many advantages, such as:

1. By proper cooling, integration times of several hours are possible without image degradation. This is equally appropriate for pulsed and continuous probes.
2. By the time enough photon events have been recorded to

minimize the effects of photon statistics (say 10^3 events), the integrated intensity is large enough for accurate readout.

3. Omitting the image intensifier increases resolution while reducing cost and complexity.
4. Slow scan readout reduces the performance requirements for the video-processing circuits.

Thus we see that this method offers numerous benefits even though it is radically different from our system (which is more nearly optimized for transient-event detection). Other possibilities include the use of ISIT cameras, GEN-II intensifiers, and charge-doupled device readout arrays.

In short, many new opportunities exist in this area for both the scientist and the engineer. Although it is not possible to predict where these endeavors will lead, it is almost certain that the results will be interesting.

Appendix A

POLLUTANT DETECTION

Table I in this appendix lists an assortment of hydrocarbon pollutants, showing relative intensities for Raman scattering and energy shifts in cm^{-1} (Fouche and Chang, 1973). Other pollutants, such as CO, CO_2, HCℓ, and H_2SO_4, can be similarly identified. We can estimate the intensity of Raman scattered light from a trace contaminant of one part per million (1 ppm) concentration at standard temperature and pressure (STP). The defining equation is:

$$W_R = N_G W_L L \frac{\partial\sigma}{\partial\Omega} \Omega \eta, \qquad (A.1)$$

where

W_R = Watts of Raman signal

W_L = Watts of input laser power

$\frac{\partial\sigma}{\partial\Omega}$ = Differential cross section of gas molecule

Ω = Solid angle of collection optics

L = Scattering length

N_G = Number of molecules per unit volume

η = Total efficiency of collection optics and spectrograph.

Representative values:

W_L = 5 Watts, argon ion laser (5145 Å)

$\frac{\partial\sigma}{\partial\Omega}$ = 4.5×10^{-31} cm^2/sr per molecule N_2 at 5145 Å. Similar to most pollutant cross sections (off resonance).

Ω = 0.79 sr for f/1 optics

L = 0.125 cm. The spectrograph is f/8 with a 1 cm high entrance slit. The ratio of f-numbers requires a

TABLE I

a = acetylene
b = butane
1b = 1-butene
2b = cis-2 butene
3b = 1-3-butadiene
ib = isobutene
ea = ethane
ey = ethylene
m = methane
ma = methyl acetylene
p = propylene
t = toluene

Relative intensities are $100 \times (c_x / c_{N_2})$.

Molecule	Δν (cm^{-1})	Relative Intensity	Separation from previous line	Molecule	Δν (cm^{-1})	Relative Intensity	Separation from previous line	Molecule	Δν (cm^{-1})	Relative Intensity	Separation from previous line
t	201	173		ey	1342	300	36	1b	2886	344	3
ma	327	115	126	ma	1379	38	37	b	2888	201	2
2b	331	42	54	t	1381	71	2	p	2895	75	7
ib	383	19	2	2b	1381	477	0	ea	2897	655	2
b	428	78	45	ib	1416	155	35	1b	2909	291	12
ib	431	19	3	1b	1422	53	6	ib	2911	501	2
p	476	62	5	p	1430	80	8	m	2914	79	3
1b	487	80	1	3b	1442	279	12	3b	2914	31	0
t	511	220	74	b	1459	81	17	b	2921	80	7
3b	513	348	2	ma	1463	15	4	p	2928	320	7
t	624	78	111	2b	1465	53	2	t	2932	358	4
ma	635	35	11	ea	1478	26	13	2b	2933	345	1
t	786	46	151	t	1602	213	24	ma	2939	504	6
2b	803	210	17	ey	1623	172	21	ea	2944	780	5
b	833	150	30	ib	1640	388	17	1b	2945	341	1
1b	852	249	21	3b	1643	200	3	b	2946	144	1
2b	868	145	16	2b	1648	166	5	b	2969	34	23
ib	883	21	15	ib	1655	181	7	p	2986	65	17
2b	900	63	17	ey	1656	13	1	ib	2989	281	3
ma	919	74	19	p	1656	216	0	ma	3000	43	11
p	925	146	7	3b	1772	26	116	1b	3004	519	4
b	967	26	41	3b	1865	135	93	3b	3014	691	10
ea	990	173	23	ma	1967	51	102	p	3016	177	2
2b	1003	47	13	ma	2133	427	66	1b	3017	385	1
t	1011	81	8	ib	2731	50	598	ey	3019	592	2
ib	1058	36	47	b	2742	57	11	m	3020	800	1
b	1062	53	4	p	2746	25	4	2b	3031	246	11
b	1150	27	88	ma	2749	16	3	t	3062	847	31
t	1204	234	54	ea	2758	46	9	ib	3079	60	17
3b	1205	280	1	ea	2793	28	35	1b	3087	154	8
2b	1253	59	48	ib	2860	26	67	p	3089	41	2
3b	1279	172	26	p	2866	38	6	3b	3100	135	11
1b	1292	146	13	b	2870	94	4	ma	3328	39	228
b	1293	208	1	2b	2875	126	5	ma	3369	13	41
3b	1303	173	10	ey	2880	8	5	a	3374	111	5
p	1306	145	3	ma	2883	87	3				

magnification of 8:1 so L = 0.125 cm.

N_G = 2.64×10^{13} cm^{-3} for 1 ppm at STP

η = 7%. Collection optics 70% throughput, spectrograph and post-optics, 10%.

Substitution of these values yields $W_R = 4 \times 10^{-19}$ W/ppm, or in terms of photons:

$$n = \frac{(4 \times 10^{-19}) \text{ W/ppm})}{(3.8 \times 10^{-19} \text{ W-sec/photon})} \simeq 1 \text{ photon/sec/ppm} \quad (A.2)$$

For a detector quantum efficiency of 20%, we get 0.2 counts/sec/ppm detected. It is possible to construct a multiple pass sample cell which yields a 50:1 improvement in Raman signal intensities for gaseous samples (Stafford et al., 1976). Using this technique, a detected signal of 10 counts/sec/ppm can be expected. Thus 100 counts/ppm would be obtained over a 10 sec integration period, resulting in a statistical uncertainty of 0.1 ppm.

The detection of automotive exhaust pollutants by means of the PCD-based Raman scattering method is characterized by good sensitivity (1 ppm or less), moderate response speed (10 sec), and a unique ability to simultaneously identify many different pollutant species. A recent publication, Instrumentation for Monitoring Air Quality (ASTM, 1974), provides a review of instruments commonly used for the detection of hydrocarbons, nitrous oxides, sulphur dioxide, ozone, etc.

Nearly all of these detectors provide sensitivity for only a single species or for a limited class of contaminants, and many are degraded by the presence of other possible atmospheric constituents. Some examples are:

1. Flame ionization detection (FID): Detects total carbon

content. Interference is caused by hydrocarbons containing nitrogen, oxygen, or halogens.

2. Gas chromatography (GC): Detects individual hydrocarbons (not "real-time").
3. Non-dispersive infrared absorption (NDIA): Detects total hydrocarbon content. Interfering species include CO, CO_2, and H_2O.
4. Chemiluminescence: Detects total NO_x content. Quenched by CO_2, H_2O, NH_3.
5. Colorimetry (wet chemical): Detects NO_2 or SO_2.
6. Flame photometry: Detects total sulphur content.

Only the various light-scattering techniques such as second derivative ultra-violet absorption, dispersive infrared absorption, and the Raman effect appear attractive for the purpose of providing simultaneous real-time analysis of many different pollutants. Of these, the PCD-based Raman-scattering method is particularly attractive since it requires only one light source and one detector.

It is noteworthy that the I^3Isocon PCD described in this work can provide far more than 100 resolvable spectral elements if used in conjunction with a cross-dispersive spectrograph (Wood et al., 1975). A cross-dispersed instrument can fold a broad spectrum into a rectangular matrix of wavelength elements, allowing full utilization of the two-dimensional nature of the detector. Thus, the maximum number of resolvable "channels" could be extended to well over 3,000. This would provide resolution of better than 1 cm^{-1} for all Raman shifted signals in the 200 cm^{-1} to 3400 cm^{-1} region, thereby including all of the tabulated Raman-active pollutants.

Appendix B

CALCULATION OF COLLECTION EFFICIENCY

Given a point source which radiates uniformly throughout a solid angle of 2π steradians (i.e., a hemispherical source distribution), we calculate the percentage of available light collected by a given lens. Spherical coordinates are defined in the customary manner (Fig. B1):

$$\begin{aligned} x &= r\sin\theta\cos\phi \\ y &= r\sin\theta\sin\phi \\ z &= r\cos\phi. \end{aligned} \tag{B.1}$$

The differential element of surface area is thus $dA = r^2\sin\theta d\theta d\phi$. Consider a point source lying at the origin and radiating into the $z > 0$ hemisphere. A hemispherical collector (100% collection) of radius R has the area

$$\begin{aligned} A_H &= R^2\int_0^{\pi/2}\sin\theta d\theta\int_0^{2\pi} d\phi \\ &= 2\pi R^2[-\cos\theta]_0^{\pi/2} = 2\pi R^2. \end{aligned} \tag{B.2}$$

A lens of diameter D is placed with the optical axis along z. If the distance from the origin to the lens is L, then the geometry is as shown in Fig. B2. The lens occludes part of the hemispherical surface. The area of this occluded surface is:

$$\begin{aligned} A_L &= R^2\int_0^{\theta_M}\sin\theta d\theta\int_0^{2\pi} d\phi \\ &= 2\pi R^2[\cos\theta]_{\theta_M}^{0} = 2\pi R^2[1 - \cos\theta_M]. \end{aligned} \tag{B.3}$$

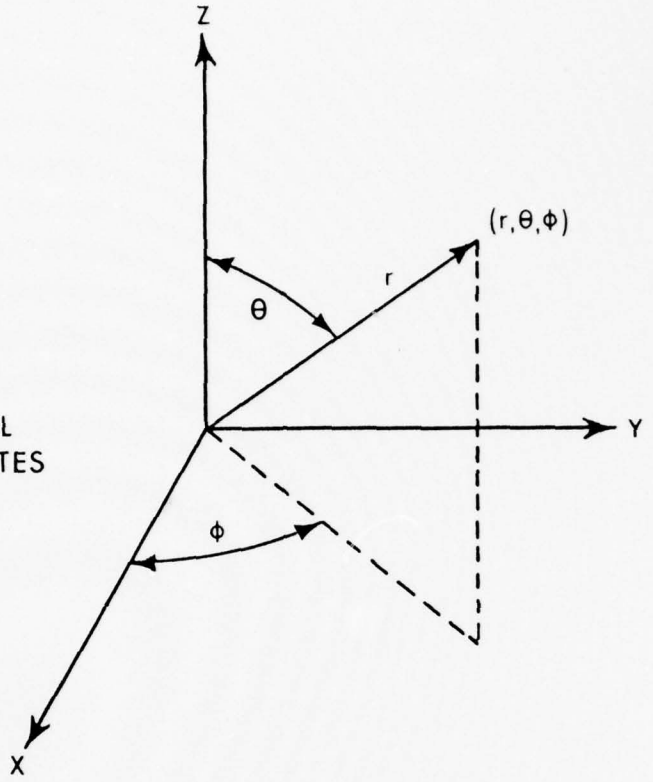


Figure B1

SPHERICAL COORDINATES

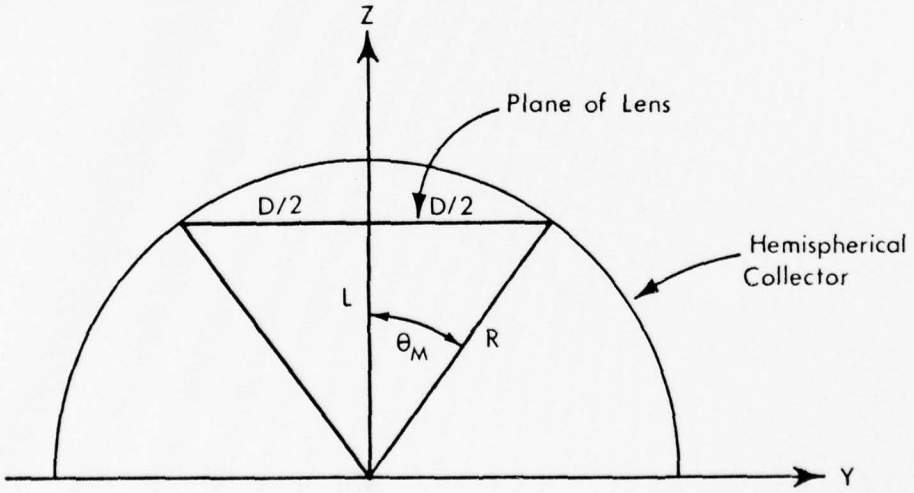


Figure B2

GEOMETRIC RELATIONSHIPS

The fraction of light intercepted by the lens is:

$$Q = A_L/A_H = \frac{2\pi R^2[1 - \cos\theta_M]}{2\pi R^2} = 1 - \cos\theta_M. \qquad (B.4)$$

From Fig. B2, we see that

$$\cos\theta_M = L/R = \frac{L}{(L^2 + D^2/4)^{1/2}} = [1 + \frac{D^2}{4L^2}]^{-1/2}. \qquad (B.5)$$

The effective f-number of the lens is f = L/D. Making this substitution, we find:

$$Q = 1 - [1 + 1/(2f)^2]^{-1/2}. \qquad (B.6)$$

Collection efficiencies based on this formula are plotted in Fig. B3.

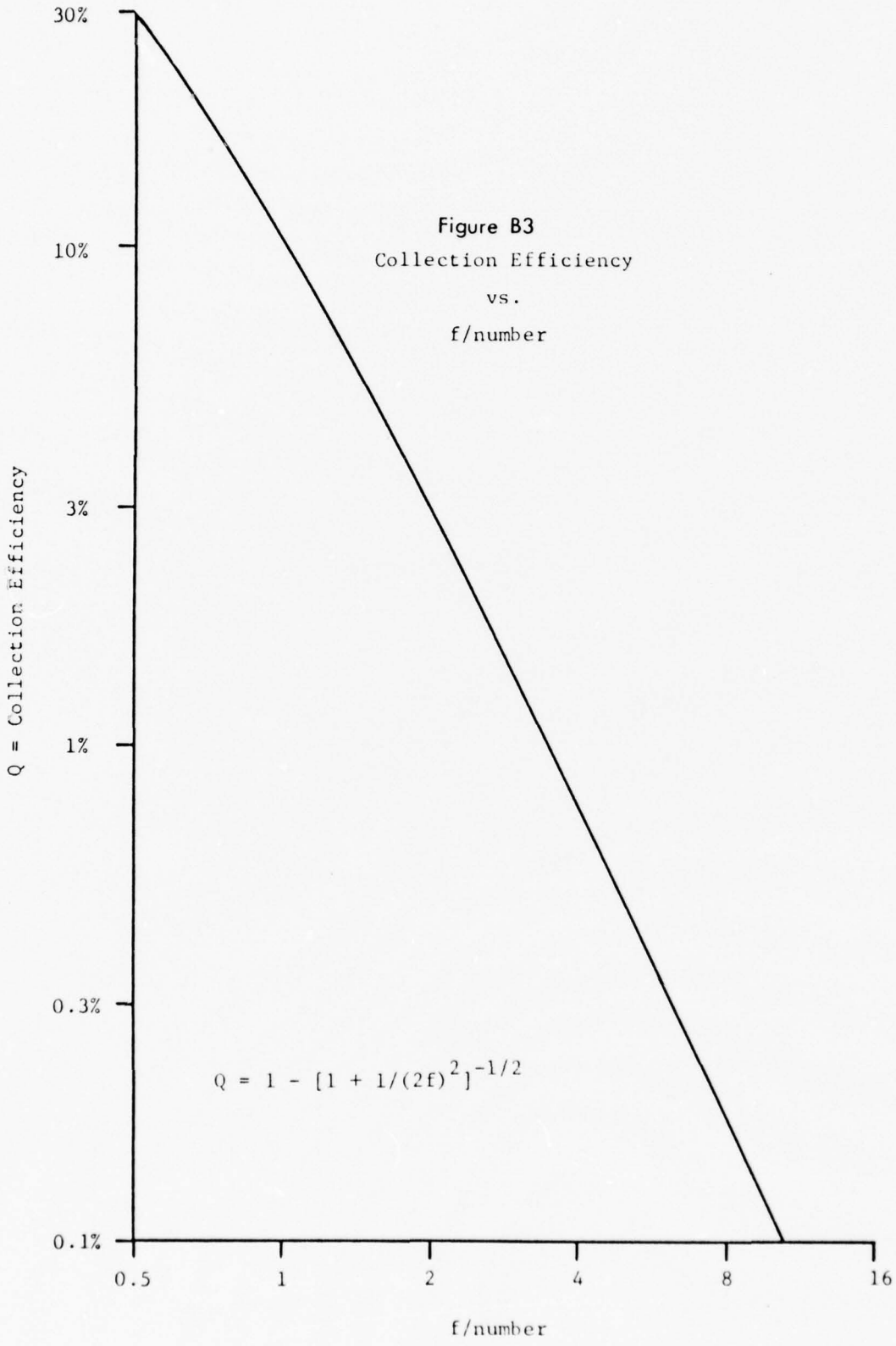


Figure B3
Collection Efficiency
vs.
f/number

Appendix C

THE SELECTIVE-SCAN TECHNIQUE

A computer or special purpose analyzer which explicitly controls the television camera scan pattern can increase the PCD's intrinsic dynamic range by a factor of almost 1000:1. This "Selective-Scan" method is based on the readout characteristics of the TV camera tube. The camera temporarily stores an image on its target as a charge distribution. Noise (target readout or video preamplifier) limits the smallest charge density which may be detected. The largest charge density which may be linearly detected is limited by various saturation effects. Let us call these minimum and maximum charge densities Q_{min} and Q_{max}, respectively. Such charge "bumps" are created by integrating the incoming photoelectrons for a period T, equal to one frame period. Thus we define the maximum and minimum acceptable levels by:

$$\begin{aligned} I_{max} &= Q_{max}/T \\ I_{min} &= Q_{min}/T. \end{aligned} \tag{C.1}$$

However, suppose that we could selectively vary T, the time between successive readouts. Then if $T_{min} < T < T_{max}$, we would choose T_{min} for strong signal areas and T_{max} for weak signal areas. In this way, the acceptable illumination levels become:

$$\begin{aligned} I'_{max} &= Q_{max}/T_{min} \\ I'_{min} &= Q_{min}/T_{max}. \end{aligned} \tag{C.2}$$

The original camera had a dynamic range (D) of

$$D = I_{max}/I_{min} = Q_{max}/Q_{min}, \tag{C.3}$$

whereas the "selective" camera has a dynamic range of

$$D' = I'_{max}/I'_{min} = (Q_{max}/Q_{min})(T_{max}/T_{min})$$

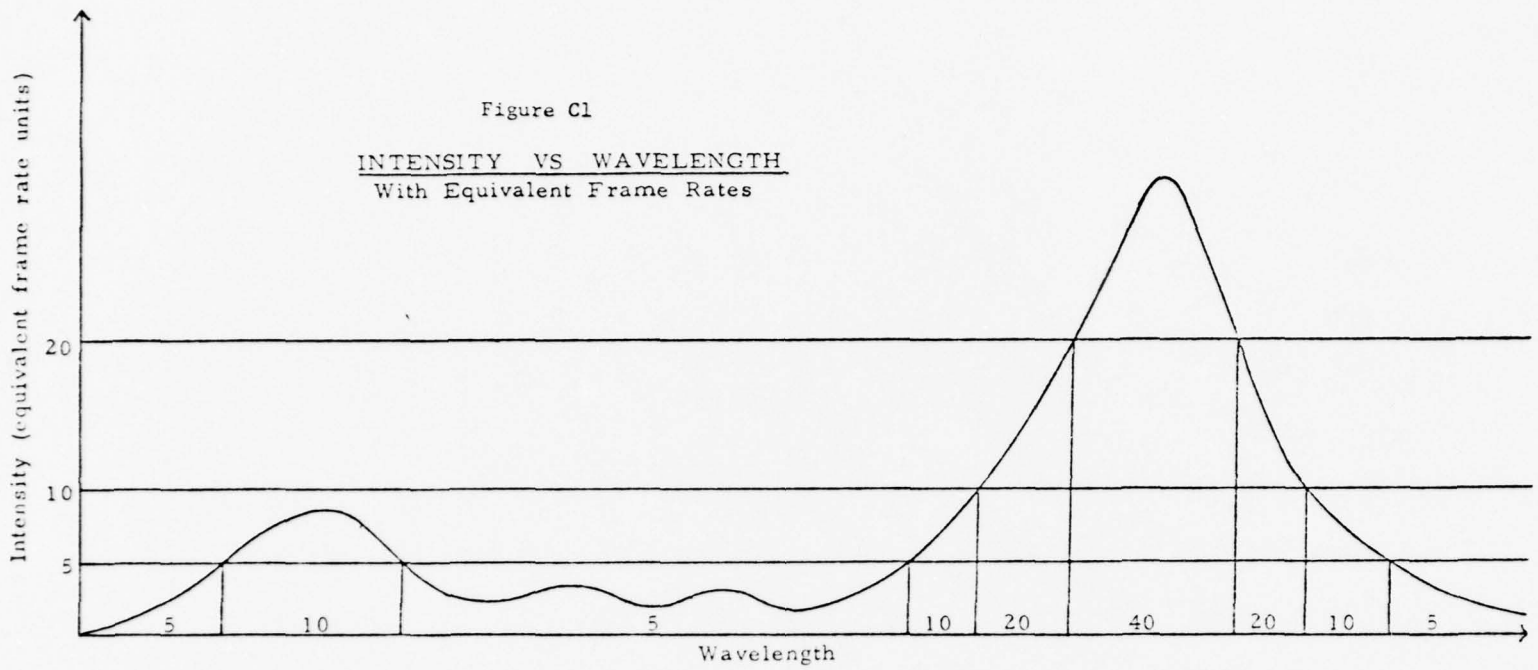
$$D' = D(T_{max}/T_{min}). \tag{C.4}$$

Whenever the spectra of interest are stationary, the above argument can be realized in hardware. First, a preliminary scan is taken for the purpose of making a rough determination of the spectral line intensities. A computational algorithm then compiles a table of TV camera yoke commands which cause the bright areas of the target to be scanned more frequently than the dark areas. For the Isocon, T_{min} is limited by practical beam speed to a few milliseconds and T_{max} is a few seconds. Thus, useful dynamic range may be extended by a factor of 10^3 under certain circumstances. (Note that the average intensity over the entire target must be less than Q_{max} or the read-beam will simply be unable to keep up with the total demand.)

Figs. C1 and C2 depict two idealized spectra and how they might be handled by the Selective-Scan Technique. It is interesting to see that this technique not only "knocks down" the high intensity peaks (preventing target saturation by frequent local erasure) but also "brings up" the low intensity areas by the use of long equivalent frame rates. This action prevents overscanning of "dark" areas of the target, a practice which normally acts to desensitize the target unless backlighting is employed.

Figure C1

INTENSITY VS WAVELENGTH
With Equivalent Frame Rates



The horizontal lines indicate an exponential series of intensity values, each with an associated equivalent frame rate (the number of times an area is to be scanned each second). The vertical lines show the division of the camera target into vertical strips of nearly constant intensity, with the equivalent frame rate for each strip given beneath the curve. In this case frame rates from 5 to 40 frames/second are required, with an average rate of 20/second.

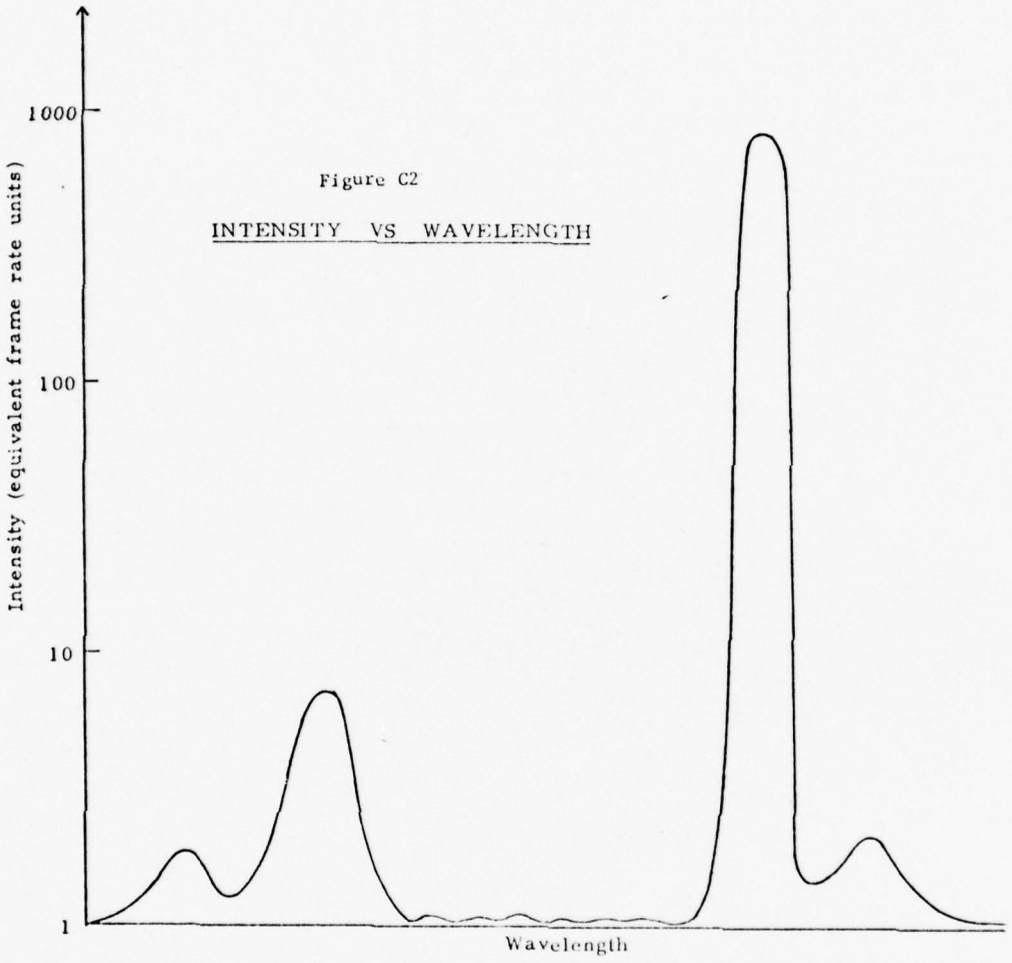


Figure C2

INTENSITY VS WAVELENGTH

The arbitrary intensity units are chosen to correspond to the equivalent frame rates necessary to keep the isocon target in the linear operating region. The previous figure demonstrated a dynamic range of approximately 10:1 with a maximum frame rate of 40/second; i.e. a reasonable task for a standard camera. The current figure exhibits a much greater dynamic range and requires a maximum frame rate of nearly 1000/second. However, if the target is divided into strips in the same manner as Fig. C1, the average frame rate is 30/second, well within the limits of a standard camera and deflection yoke.

Appendix D

DIGITAL I/O INTERFACE

Fig. D1 shows the basic structure of the interface, all circuitry being standard TTL. Data interchange with the computer is carried out via the 16 bit bi-directional bus <CB00:CB15>. In addition, there are two uni-directional control lines from the computer: CBW (write) and CBR (read). Computer Bus line receivers and line drivers act as a repeater between the Computer Bus and the internal Data Bus <DB00:DB15>. A second bus repeater is located near the META-4 computer so that the 250' long Computer Bus is properly terminated at both ends. Tri-state buffers (and associated control logic) are used throughout to prevent competition for control of the data lines. Internally, all data to/from the computer are carried by the 16 bit Data Bus <DB00:DB15>, which is interfaced to each card in the device. Data entry switches and display lights mounted on the front panel of the interface serve two functions. The display lights indicate the current status of the Data Bus, regardless of the mode of operation. The data entry switches are active only in "LOCAL" mode (switch selectable). In "REMOTE" operation the computer is treated as either the source or destination of all Data Bus information, whereas LOCAL operation ignores all Computer Bus information and treats the Data Panel as source/destination. Since the Data Panel has pushbutton switches corresponding to CBW and CBR, any function which the computer executes can also be executed (slowly) via the Data Panel. This feature has two important consequences:

1. An independent manual check can be made of almost all

circuits in the interface.

2. When the computer is not available, the interface can be "set up" via manual data entry and has the ability to operate the detector head in a stand-alone configuration. A multichannel analyzer can be used during stand-alone operation to collect the data. Although this type of operation is not as flexible as fully computerized data collection, it provides a highly desirable backup system which may be used for alignment, initial data runs, device testing, etc.

The typical wire wrap board shown in Fig. D1 receives computer data via the Data Bus. In order to limit loading of the Data Bus, each card has a bus buffer which presents a single load to the bus while providing a fanout of 10 on the internal data lines <D00:D15>. The data are almost invariably stored in a latch (memory element) for further use by internal or external hardware. All such latches are continuously connected to the data lines, but control lines uniquely designate which latch is the correct destination for a particular datum.

Data transmitted from the computer has the format shown in Fig. D1. Since there are many possible destinations for transmitted data, a portion of each word must be used as a destination address (or function code). The first four bits of each word are used to determine the primary function code (16 choices). Typically four more bits are needed to fully specify the desired function, leaving eight bits (one byte) of actual data. It often occurs that the function code itself contains all of the necessary information for a given command, leaving the data bits unused. For instance, a function might create a pulse

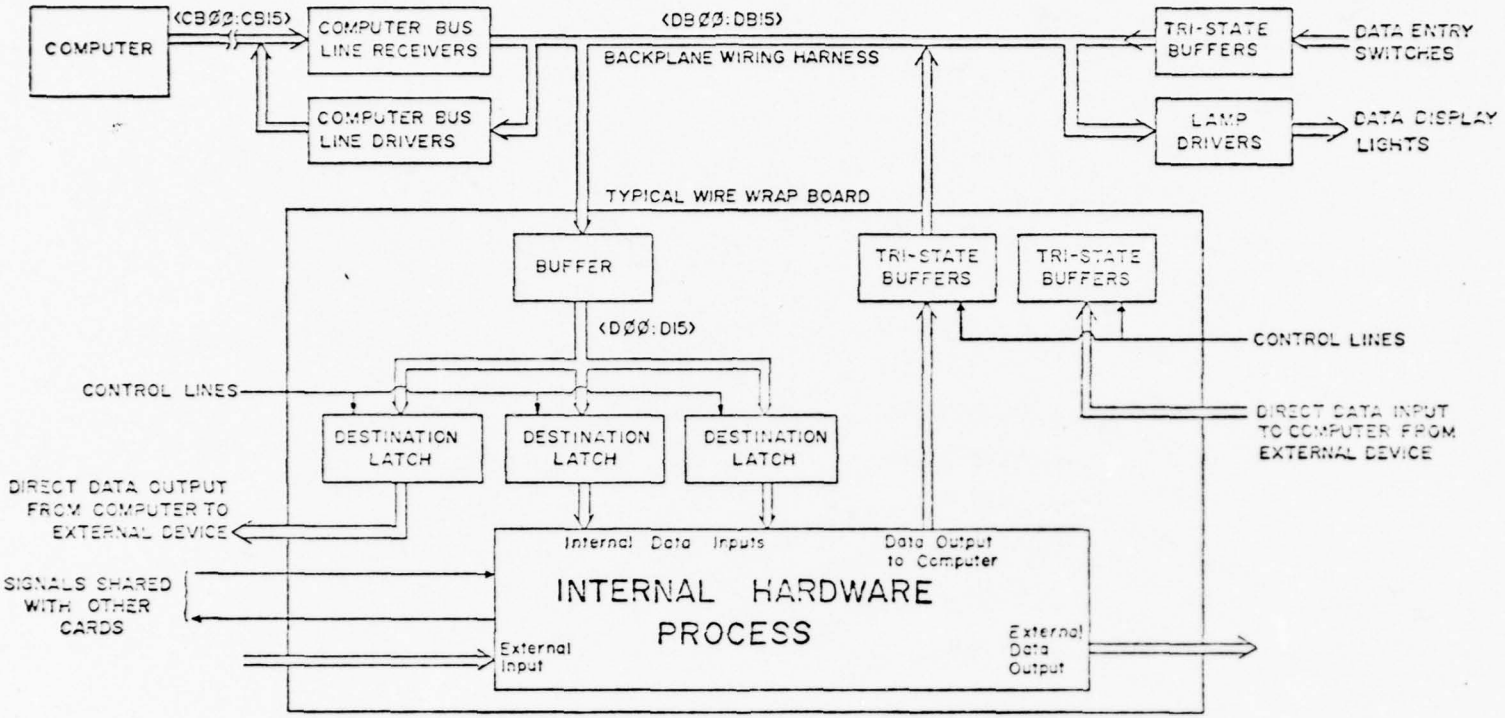
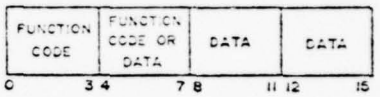


FIGURE D1: DIGITAL I/O INTERFACE



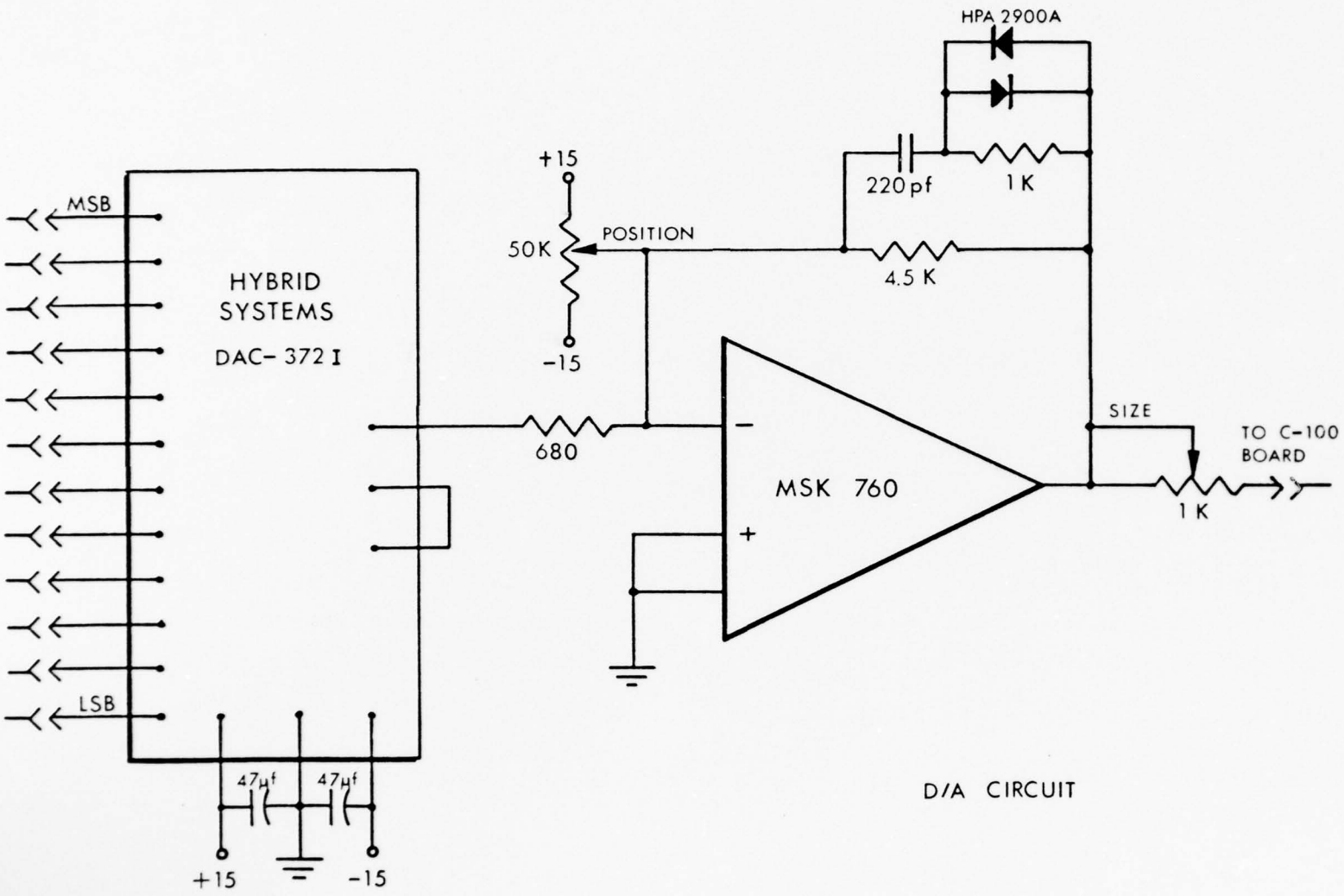
BEST AVAILABLE COPY

on a particular digital output line or reset some indicator in the interface. Another function is to request that a certain piece of information be made available to the computer (read request). The data returned by the interface can utilize all 16 bits since no destination code is needed--i.e., the computer is the only possible destination for such a transaction.

Appendix E

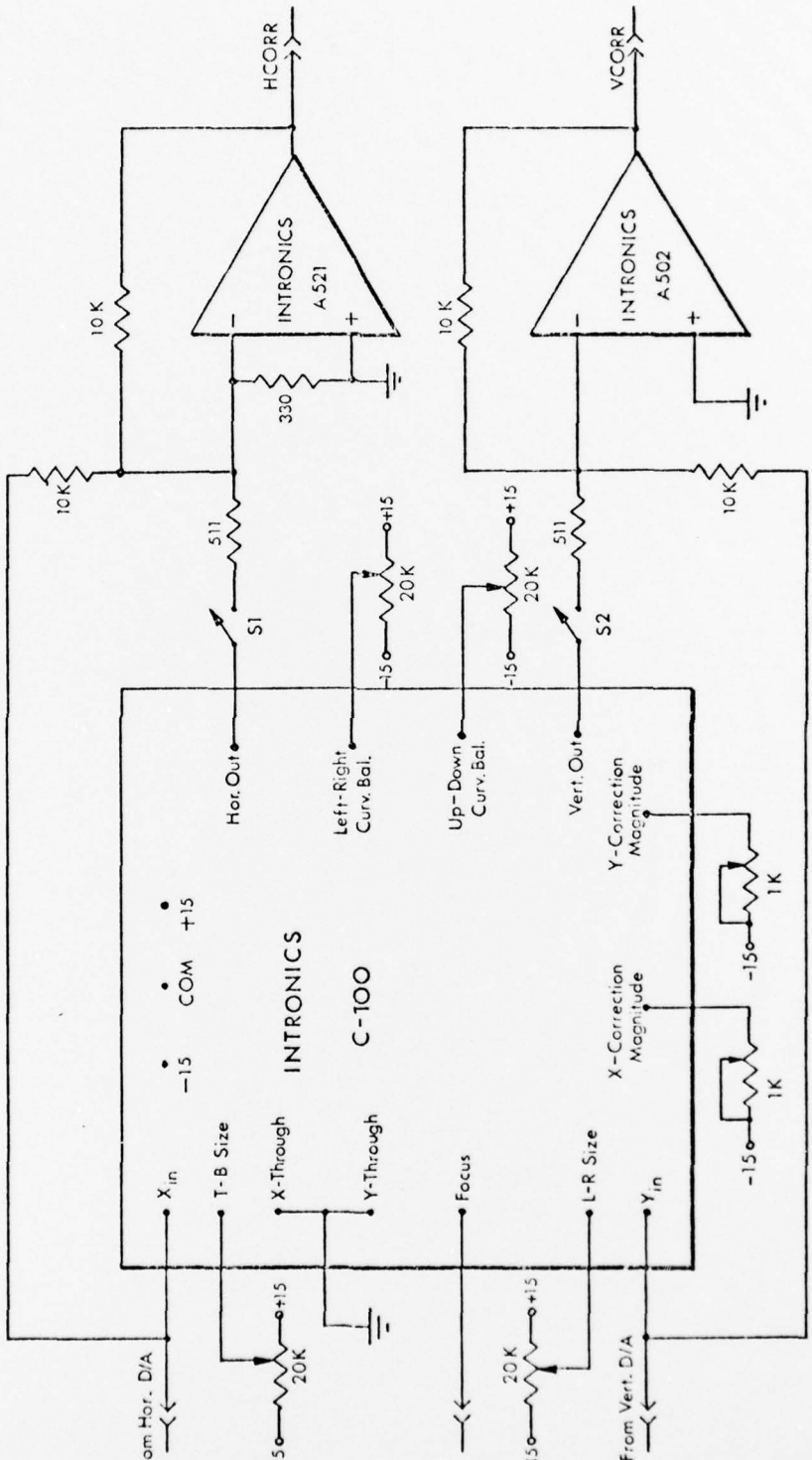
SUPPLEMENTARY INFORMATION

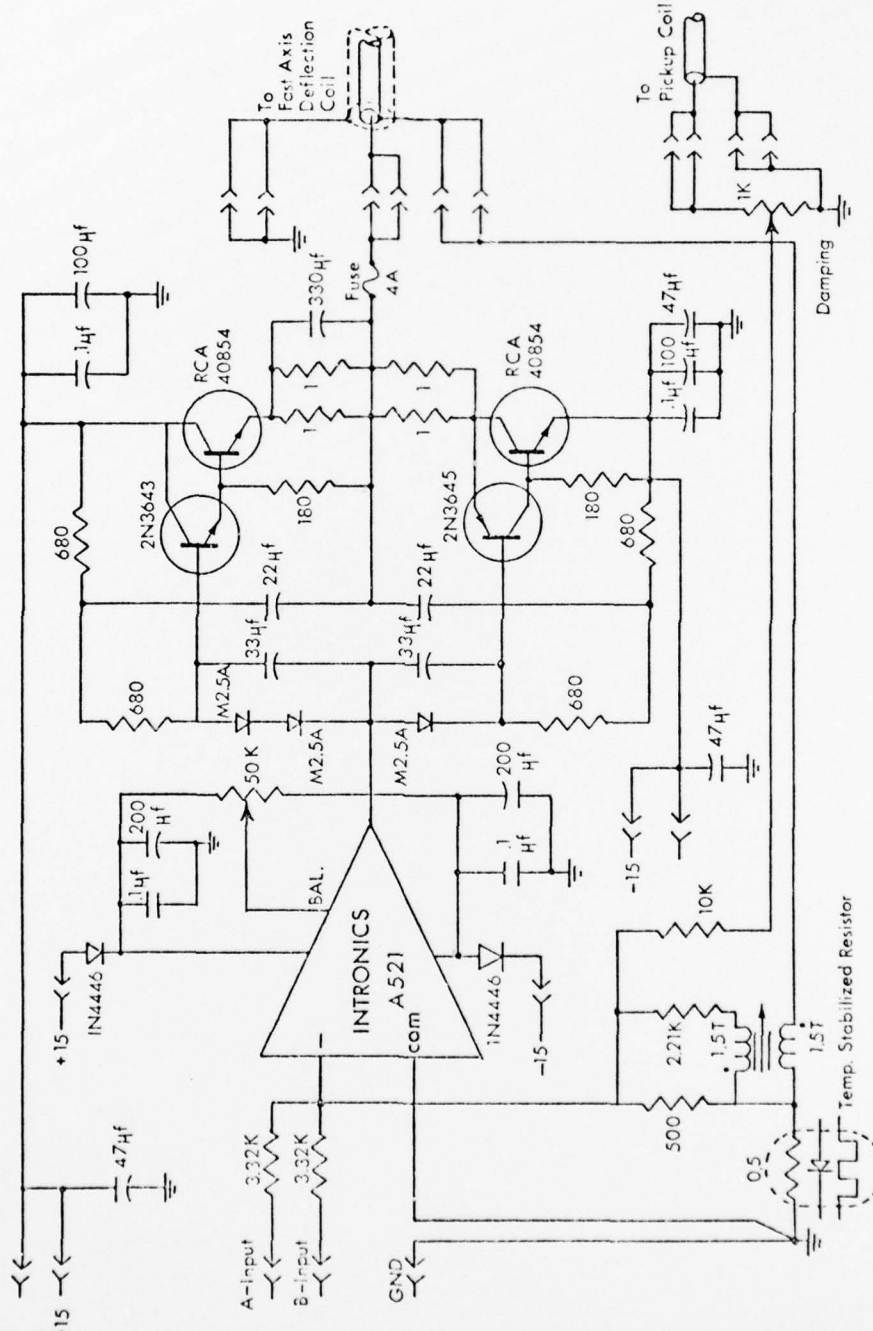
Title	Page
D/A Circuit	165
Geometry Correction Circuit	166
160 μH Yoke Driver	167
RCA 4807A Image Isocon Characteristics	168-169
Varo 8606 Image Intensifier Characteristics	170-172


HPA 2900A
+15
220 pf
1 K
50K
POSITION
4.5 K
-15
MSB
HYBRID
SYSTEMS
DAC- 372 I
680
SIZE
TO C-100
BOARD
MSK 760
1 K
LSB
47μf
47μf
+15
-15

D/A CIRCUIT

GEOMETRY CORRECTION CIRCUIT





160μH YOKE DRIVER

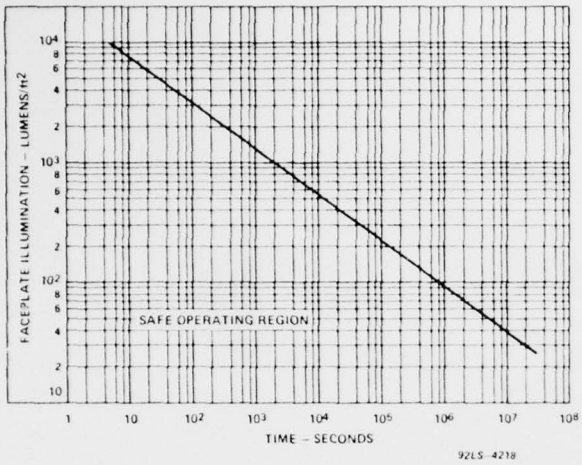


Figure 4 – Faceplate Exposure Limit

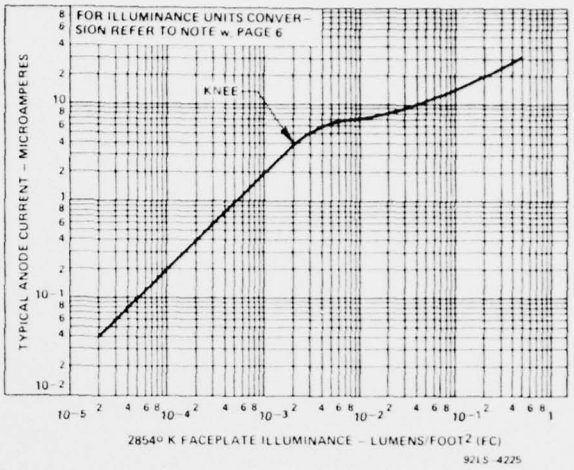


Figure 6 – Typical Transfer Characteristic

BEST AVAILABLE COPY

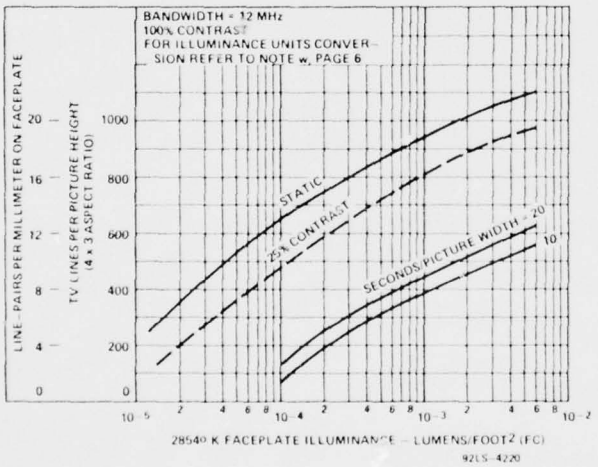


Figure 5 – Typical Dynamic Limiting Resolution

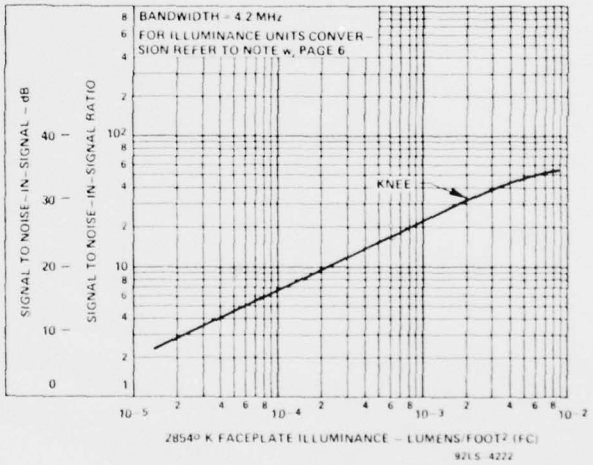


Figure 7 – Typical Signal to Noise-In-Signal Ratio As A Function of Faceplate Illuminance or Irradiance From Flux Levels Within A Given Scene. (Beam Adjustment Fixed At 2 x Knee Setting)

BEST AVAILABLE COPY

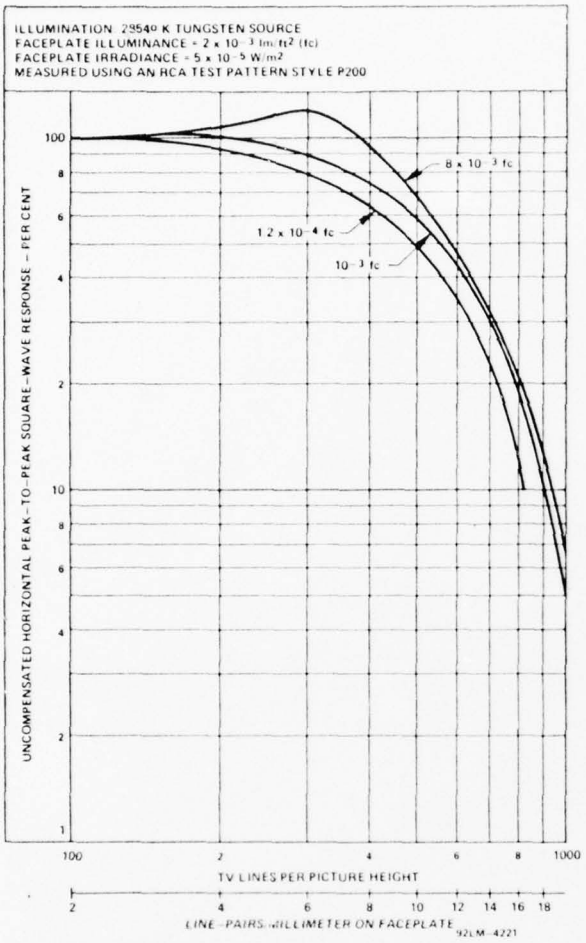


Figure 8 – Typical Amplitude Response (CTF) Characteristic

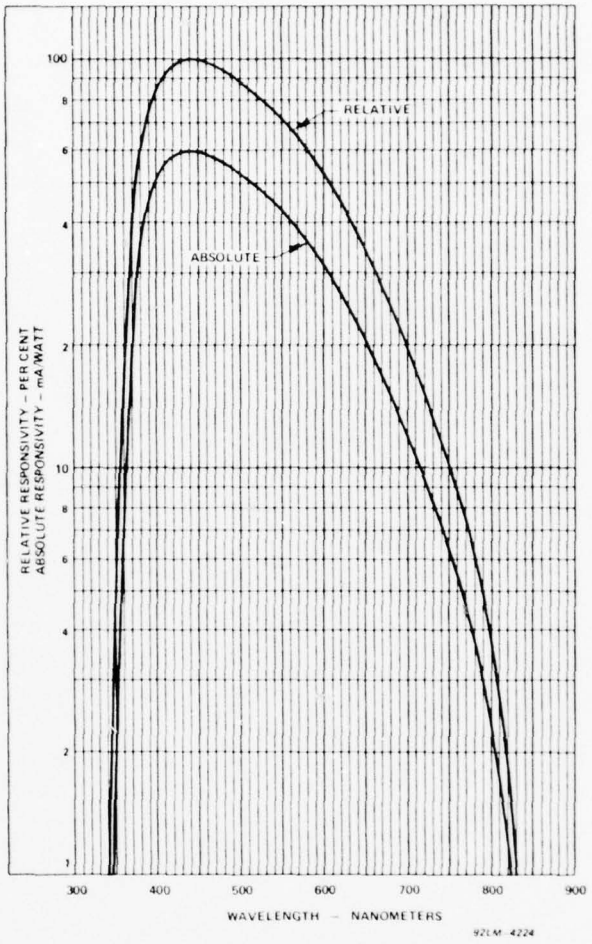


Figure 10 – Typical S-20 Spectral Response

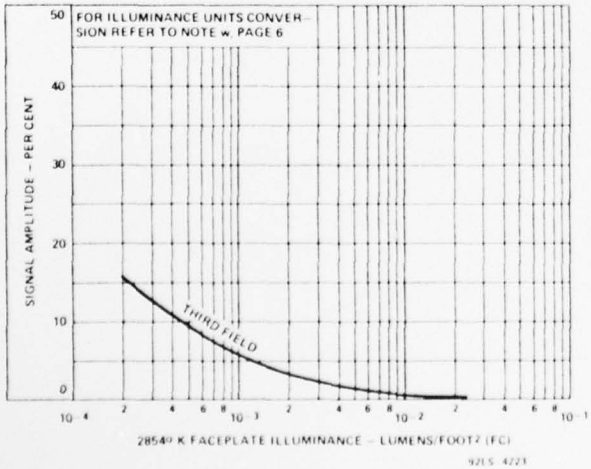


Figure 9 – Residual Signal (Lag) Characteristic

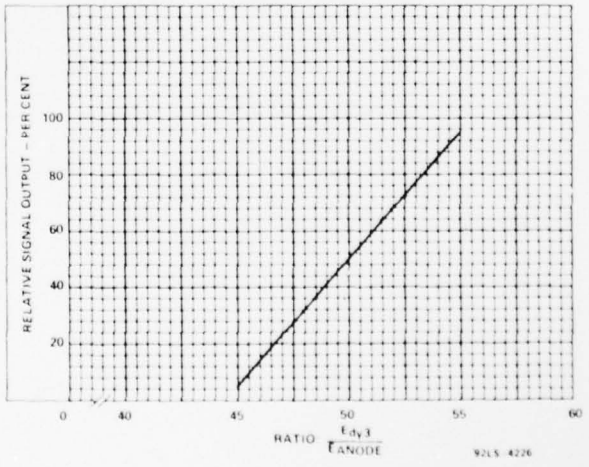
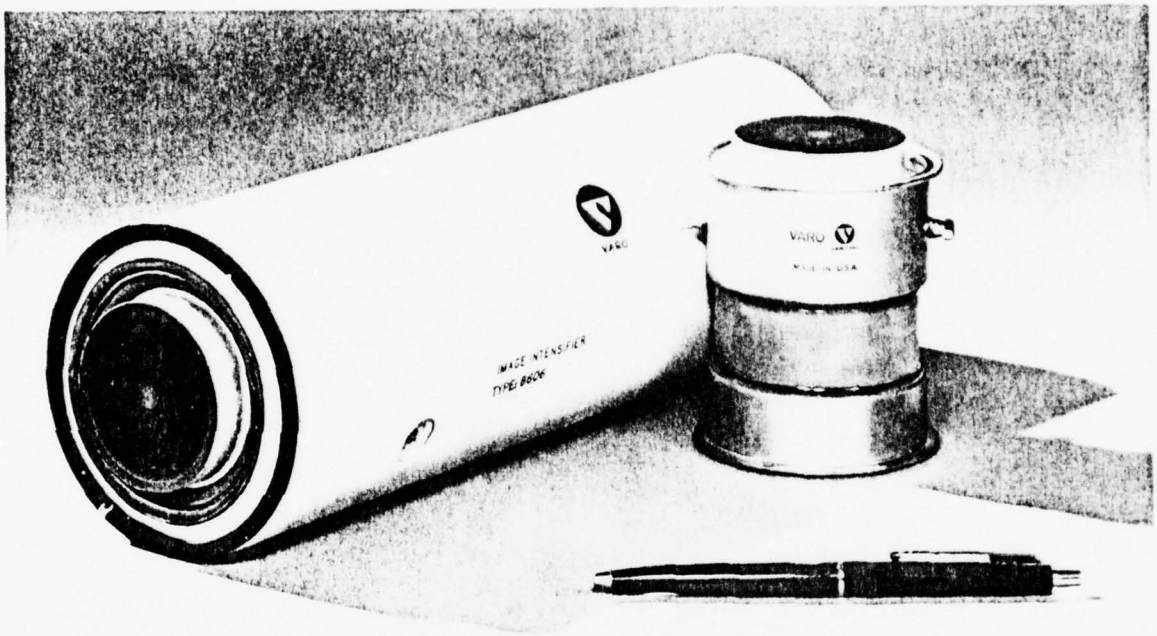


Figure 11 – Typical Dynode Gain Control

IMAGE INTENSIFIER ASSEMBLIES
VARO MODELS 8605 and 8606



40 MM IMAGE INTENSIFIER ASSEMBLY

Application:

Varo's Image Intensifier Assemblies are used for direct viewing at low light levels in the visible and near infrared regions of the spectrum. The intensified image can also be coupled to other remote viewing devices.

Since these intensifiers are passive in nature, they require no artificial light source. For example, the light available from the stars and the faint upper air glow on a cloudy, moonless night is sufficient to present a usable image.

Description:

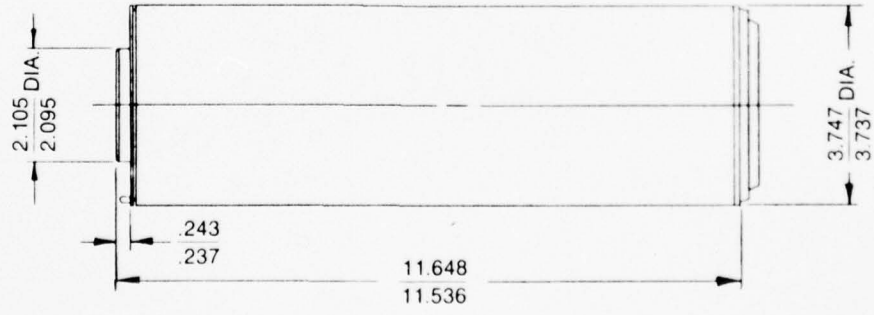
The 40 millimeter Image Intensifier Assemblies utilize an electrostatically-focused diode and require only one potential across each module. The three-stage assemblies are furnished with the voltage multiplier, and require only a 6.75 volts DC power source and oscillator which can also be furnished for operation.

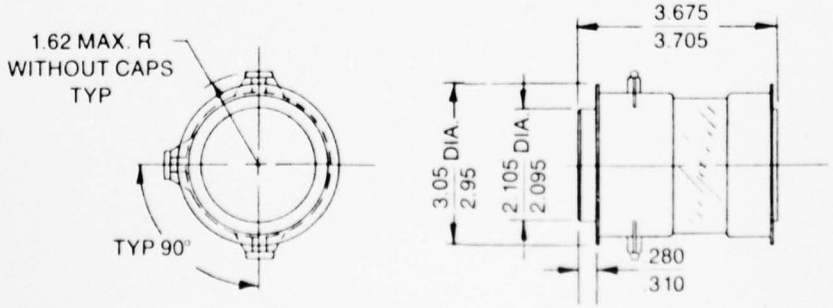
These tubes have a minimum of 63 lp/mm resolution in a single stage and 28 lp/mm in the three stage assemblies. The modules are optically and mechanically coupled together with fiber optic faceplates which act both as field flatteners and image transporters.

When rays of light are focused by the objective optics onto the photocathode of the tube, an image of emitted electrons is formed. These electrons are then electrostatically accelerated before being focused on the phosphor screen of the tube. The gain of the energy of the electrons is then evidenced as a light amplified image which may then be observed through conventional optics.

SPECIFICATIONS	3-STAGE ASSY. (8606)	SINGLE STAGE (8605)
Nominal Operating Voltage	45,000 Volts	15,000 Volts
Min. Resolution (center)	28 lp/mm	63 lp/mm
Min. Resolution (off center)	25 lp/mm	50 lp/mm
Magnification	.82 to 1.0	.94
Gain	35,000 minimum	60 minimum
Focusing Method	Electrostatic	Electrostatic
Photocathode	S-20 with extended Red Response	S-20 with extended Red Response
Cathode Sensitivity	175 μa/lumen minimum	175 μa/lumen minimum
Red Response		
@ 8000 A	12 to 40 ma/watt	12 to 40 ma/watt
@ 8500 A	5 to 25 ma/watt	5 to 25 ma/watt
@ 9000 A	On Request	On Request
Phosphor	Aluminized P-20	Aluminized P-20
Equiv. Background Input	Less than 2×10^{-11} lumens/sq cm	Less than 2×10^{-11} lumens/sq cm
Distortion	21% Maximum	7% Maximum
Modulation Transfer Function		
@ 2.5 lp/mm	90% Minimum	96% Minimum
@ 7.5 lp/mm	60% Minimum	87% Minimum
@ 16 lp/mm	20% Minimum	68% Minimum
@ 25 lp/mm		50% Minimum
@ 35 lp/mm		30% Minimum

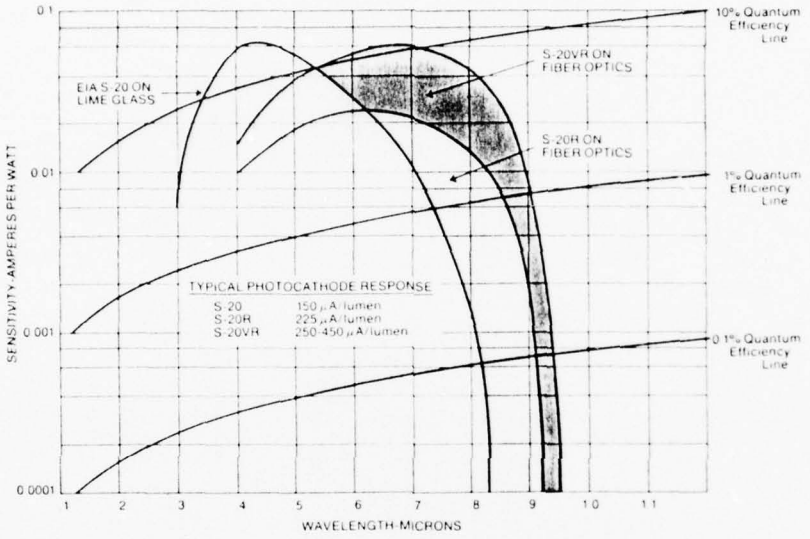
The above specifications represent present production quality. Units may be selected for special applications to a more rigid specification in any of the above categories.





BEST AVAILABLE COPY

VARO S-20 PHOTOCATHODE RESPONSE



Select the photocathode response for your particular requirement. The S-20 VR is available in all Varo Image Intensifiers.

The development of this photocathode greatly improves the spectral quality of the standard S-20 and enables viewing of, among other things, light from Gallium Arsenide Lasers. It is now possible to select an S-20 VR that covers neodymium laser light at 1.06 microns without the instability of high thermal background of the S-1 photocathode.

PHOSPHOR SCREENS

The standard phosphor in Varo's Intensifiers is the P-20. If you require any other, they are available on special order.

REFERENCES

Arden, W.M., Hirschfeld, T.B., Klainer, S.M., and Mueller, W.A., "Studies of Gaseous Flame Combustion Products by Raman Spectroscopy," Appl. Spectry. 28, 554 (1974).

American Society for Testing and Materials, Instrumentation for Monitoring Air Quality, ASTM Special Publication No. 555 (1974).

Bandy, A.R., Hillard, M.E., and Emory, L.E., "Evaluation of Raman Scattering as a Sensor of Temperature and Molecular Density," Appl. Spectry. 27, 421 (1973).

Black, P.C. and Kindlmann, P.J., "Parallel-Channel Detection System for Low-Light Level Spectroscopy," Proceedings of the Technical Program, Electro-Optical Systems Design Conference-1973, New York, p. 206.

Bridge, N.J. and Buckingham, A.D., "The Polarization of Laser Light Scattered by Gases," Proc. Roy. Soc. (London) A295, 334 (1966).

Bridoux, M. and Delhaye, M., "Spectrométrie Raman-Laser Ultra Rapide," Nouv. d'Opt. Appl. 1, 23 (1970).

Busch, K.W., Howell, N.G., and Morrison, G.H., "The Vidicon Tube as a Detector for Multielement Flame Spectrometric Analysis," Anal. Chem. 46, 575 (1974).

Colgate, S.A., Moore, E.P., and Coburn, J., "SIT Vidicon with Magnetic Intensifier for Astronomical Use," Appl. Opt. 14, 1429 (1975).

Delhaye, M., "Rapid Scanning Raman Spectroscopy, Appl. Opt. 7, 2195 (1968).

Delhaye, M., "Pulsed Lasers and Imaging Techniques in Raman Spectroscopy," in Proceedings of the Fifth International Conference on Raman Spectroscopy, E.D. Schmid, J. Brandmüller, W. Kiefer, B. Schrader, and H.W. Schrötter, eds. (Hans Ferdinand Schulz Verlag, Freiburg, 1976), p. 747.

Dicke, R.H. and Wittke, J.P., Introduction to Quantum Mechanics (Addison-Wesley Publishing Co., Reading, Mass., 1960), p. 143.

Fouche, D. G. and Chang, R.K., "Relative Raman Cross Section for N_2, O_2, CO, CO_2, SO_2, and H_2S," Appl. Phys. Lett. 18, 579 (1971).

Fouche, D.G. and Chang, R.K., "Relative Raman Cross Section for O_3, CH_4, C_3H_8, NO, N_2O, and H_2," Appl. Phys. Lett. 20, 256 (1972).

Fouche, D.G. and Chang, R.K., personal communication (1973).

French, M.J. and Long, D.A., "A Versatile Computer-Controlled Spectrometer for Hyper Rayleigh and Hyper Raman Spectroscopy," J. Raman Spectry. 3, 391 (1975).

Gaufres, R., "Analysis of Raman Contours in Vibration-Rotation Spectra," in Laser Raman Gas Diagnostics, M. Lapp and C.M. Penney, eds. (Plenum Press, New York, 1974), p. 15.

Goerlich, P., "Photoelectric Cells for the Visible Spectral Range," J. Opt. Soc. Am. 31, 504 (1941).

Gordon, S., Schmidt, K.H., and Martin, J.E., "A TV-Scanning Method for Recording Time-Resolved Spectra of Transients Produced by a Single Pulse of Electrons," Rev. Sci. Instr. 45, 552 (1974).

Hartley, D., Lapp, M., and Hardesty, D., "Physics in Combustion Research," Phys. Today 28, 36 (1975).

Herzberg, G., Molecular Spectra and Molecular Structure I. Spectra of Diatomic Molecules, 2nd ed. (Van Nostrand-Reinhold Co., New York, 1950), p. 67.

Johnson, S.A., Fairbank, W.M., Jr., Schawlow, A.L., "Image Orthicon Spectrograph with Computer Control," Appl. Opt. 10, 2259 (1971).

Kuroda, H., Shionoya, S., Saito, H., Masuko, H., "Spectroscopy of Picosecond Light Pulses with a Television Camera System," Opt. Commun. 12, 107 (1974).

Landau, L.D. and Lifshitz, E.M., Fluid Mechanics (Pergamon Press, London, 1959), p. 148.

Lapp, M., "Flame Temperatures from Vibrational Raman Scattering," in Laser Raman Gas Diagnostics, M. Lapp and C.M. Penney, eds. (Plenum Press, New York, 1974), p. 107.

Lapp, M., personal communication (1976).

Lapp, M., Goldman, L.M., and Penney, C.M., "Raman Scattering from Flames," Science 175, 1112 (1972).

Lapp, M., Penney, C.M., and Goldman, L.M., "Vibrational Raman Scattering Temperature Measurements," Opt. Commun. 9, 195 (1973).

Lederman, S., Bloom, M.H., Bornstein, J., and Khosla, P.K., "Temperature and Specie Concentration Measurements in a Flow Field," Int. J. Heat Mass Transfer 17, 1479 (1974).

Leonard, D.A., AVCO Everett Research Laboratory, Research Note No. 914 (1972).

Liepmann, H.W. and Roshko, A., Elements of Gasdynamics (John Wiley and Sons, New York, 1957), p. 53.

Mende, S.B., "Single Photoelectron Recording by an Image Intensifier TV Camera System," Appl. Opt. 10, 829 (1971).

Moya, F., Druet, S.A.J., and Taran, J.P.E., "Gas Spectroscopy and Temperature Measurement by Coherent Raman Anti-Stokes Scattering," Opt. Commun. 13, 169 (1975).

Placzek, G. and Teller, E., "Die Rotationsstruktur der Ramanbanden mehratomiger Moleküle," Z. Physik 81, 209 (1933).

Sanford, M.T., Gow, C.E., and Jekowski, J.P., "Quantum-Limited Near-Infrared Vidicon Camera System," Rev. Sci. Instr. 47, 486 (1976).

Savage, C.M. and Maker, P.D., "Multichannel Photon Counting Spectrographic Detector System," Appl. Opt. 10, 965 (1971).

Siemon, R.E., "Polychromator with Extreme Rejection of Stray Light," Appl. Opt. 13, 697 (1974).

Stafford, J.J. and Gilblom, D., "Designing a LLL TV Camera," Electro-Optical Systems Design, August 1976, p. 52.

Stafford, R.G., Chang, R.K., and Kindlmann, P.J., "Laser-Raman Monitoring of Ambient Sulfate Aerosols," Proceedings of the National Bureau of Standards Eighth Materials Research Symposium on Methods and Standards for Environmental Measurement, 1976 (to be published).

Trolinger, J.D., Laser Applications in Flow Diagnostics, Ardograph No. 186 (1974).

Vear, C.J., Hendra, P.J., and Macfarlane, J.J., "Laser Raman and Resonant Fluorescence Spectra of Flames," J. Chem. Soc. Commun. 381 (1972).

Weber, A., "High Resolution Raman Studies of Gases," in The Raman Effect, vol. 2, A. Anderson, ed. (Marcel Dekker, Inc., New York, 1973), p. 719.

Weber, A., Porto, S.P.S., Barrett, J.J., and Cheesman, L.E., "High Resolution Spectroscopy of Gases with cw-Laser Excitation," J. Opt. Soc. Am. 57, 19 (1967).

Willetts, D.V., Freedman, P.A., and Jones, W.J., "A Czerny-Turner Spectrograph Incorporating a 2-Stage Image Intensifier for the Study of Very Weak Raman Spectra," J. Raman Spectry. 2, 249 (1974).

Wood, D.L., Dargis, A.B., and Nash, D.L., "A Computerized Television Spectrometer for Emission Analysis," Appl. Spectry. 29, 310 (1975).

Woodward, L.A., "General Introduction," in Raman Spectroscopy, Theory and Practice, H.A. Szymanski, ed. (Plenum Press, New York, 1967), p. 35.

Unclassified

SECURITY CLASSIFICATION OF THIS PAGE (When Data Entered)

REPORT DOCUMENTATION PAGE		READ INSTRUCTIONS BEFORE COMPLETING FORM
1. REPORT NUMBER	2. GOVT ACCESSION NO.	3. RECIPIENT'S CATALOG NUMBER
4. TITLE (and Subtitle) THE DEVELOPMENT OF A PARALLEL-CHANNEL SPECTROGRAPHIC DETECTOR: APPLICATIONS TO RAMAN SCATTERING.		5. TYPE OF REPORT & PERIOD COVERED Interim
		6. PERFORMING ORG. REPORT NUMBER Technical Report No. 1
7. AUTHOR(s) Philip C. Black		8. CONTRACT OR GRANT NUMBER(s) ONR N00014-76-C-0643
9. PERFORMING ORGANIZATION NAME AND ADDRESS Yale University Department of Engineering and Applied Science New Haven, Connecticut 06520		10. PROGRAM ELEMENT, PROJECT, TASK AREA & WORK UNIT NUMBERS NR 372-107
11. CONTROLLING OFFICE NAME AND ADDRESS Office of Naval Research Physical Sciences Division Arlington, Virginia 22217		12. REPORT DATE March 1977 13. NUMBER OF PAGES 177
14. MONITORING AGENCY NAME & ADDRESS (if different from Controlling Office) Office of Naval Research New York Area Office 715 Broadway New York, New York 10003		15. SECURITY CLASS. (of this report) Unclassified 15a. DECLASSIFICATION/DOWNGRADING SCHEDULE

16. DISTRIBUTION STATEMENT (of this Report)

Distribution of this report is unlimited.

17. DISTRIBUTION STATEMENT (of the abstract entered in Block 20, if different from Report)

18. SUPPLEMENTARY NOTES

Yale University Ph.D. Thesis.

19. KEY WORDS (Continue on reverse side if necessary and identify by block number)

Raman scattering
Image intensifier
Image Isocon camera
Second-order Raman effect
Flame temperature
Gas turbulence
Optical multichannel analyzer

20. ABSTRACT (Continue on reverse side if necessary and identify by block number)

A parallel-channel detector was developed for use in visible and near-infrared light scattering experiments. The design goal of obtaining quantum-limited response simultaneously over 100 resolvable spectral elements has been achieved. This level of performance allows a significant (100:1) decrease in the time required to obtain a low-light level spectrum, when compared to the acquisition times of conventional detectors, such as the photomultiplier tube or photographic emulsion. Details of the design, construction, and operating

(Cont'd)

DD FORM 1 JAN 73 1473 EDITION OF 1 NOV 65 IS OBSOLETE

Unclassified

SECURITY CLASSIFICATION OF THIS PAGE (When Data Entered)

20. characteristics of the parallel-channel detector are given, along with the results of Raman scattering measurements to determine: 1) the vibrational-rotational temperature of a flame; 2) the gas concentration profile of a gas-dynamic system. Implications of these measurement techniques are discussed.